HYBRID FIBER SORBENTS FOR ODORANT REMOVAL FROM PIPELINE NATURAL GAS

A Dissertation
Presented to
The Academic Faculty

By

Grace Chen

In Partial Fulfillment
Of the Requirements for the Degree
Doctor of Philosophy in the
School of Chemical & Biomolecular Engineering

Georgia Institute of Technology

August 2017

HYBRID FIBER SORBENTS FOR ODORANT REMOVAL FROM PIPELINE NATURAL GAS

Approved By:

Dr. Christopher W. Jones
School of Chemical & Biomolecular Engineering
Georgia Institute of Technology

Dr. William J. Koros
School of Chemical & Biomolecular Engineering
Georgia Institute of Technology

Dr. Yoshiaki Kawajiri
School of Chemical & Biomolecular Engineering
Georgia Institute of Technology

Dr. Ryan P. Lively
School of Chemical & Biomolecular Engineering
Georgia Institute of Technology

Dr. Angus Wilkinson
School of Chemistry & Biochemistry
Georgia Institute of Technology

Date Approved: June 21, 2017

ACKNOWLEDGEMENTS

I would like to acknowledge my advisers Dr. Christopher Jones and Dr. William Koros, my committee members Dr. Yoshiaki Kawajiri, Dr. Ryan Lively, and Dr. Angus Wilkinson, and my friends and family for their guidance and support in completing this project. This work was financially supported by General Electric (GE), the U.S. Department of Energy (DOE), and the Georgia Research Alliance. The National Energy Technology Laboratory (NETL) of the DOE provided partial support under Contract DE-FE0007804. I would also like to thank Dr. Bogna Grabicka and Dr. Krista Walton for providing the large-batch UiO-66(Zr) material used in this study.

TABLE OF CONTENTS

LIST OF TABLES

LIST OF FIGURES

SUMMARY

Pipeline natural gas is typically odorized with about 10 ppm or less of mercaptans for safety purposes in case of a leak. When these sulfur compounds are burned in air inside of gas turbines for electricity generation, they react with alkali material present in air to form a corrosive combustion product which corrodes the inside of the turbine and reduces its efficiency and lifetime. It is therefore of interest to remove these mercaptan odorants from pipeline natural gas before introduction into combustion turbines for the purposes of preventing or delaying corrosion associated with SOx production, and extending turbine lifetime. Sulfur-free natural gas can also prevent deactivation in catalysts used for both exhaust gas cleanup and for hydrogen production for fuel cells via steam reforming. Selective adsorption of odorants onto solid materials is an attractive approach to address this problem because of its ability to remove these trace levels of sulfur and to be operated at low temperatures, meaning that it is less energy-intensive than other traditional sulfur removal methods. The overall goal of this research is to fabricate and optimize a hybrid fiber sorbent system for odorant removal from pipeline natural gas.

Three objectives were established to meet this goal and are discussed in detail in the following chapters: (1) Investigate the ability of several synthesized MOFs and commercial zeolites to selectively adsorb a common odorant, *tert*-butyl mercaptan (TBM), from both a mercaptan / inert gas feed and a model natural gas feed; (2) Fabricate and evaluate hybrid fiber sorbents with high sorbent loadings and desired separation properties; (3) Assess the performance and stability of the fiber sorbents in a cyclic

temperature swing adsorption (TSA) system in a module configuration. Previous system design calculations indicated that fiber sorbent modules can offer several advantageous over traditional fixed bed technologies in terms of lower pressure drop and faster heat and mass transfer rates, leading to greater energy and spatial savings.

Adsorbent material selection is important for this application, and a material with high mercaptan uptake capacity, selectivity, and regenerability is desired for the practical implementation of such an adsorption system. These aspects are important to the economic viability of a TBM removal system in an industrial setting. Cu-BTC and MIL-53(Al) displayed higher capacities and selectivities than the benchmark zeolites studied. All materials except Cu-BTC were found to be fully or partially regenerable upon heating in flowing inert gas and were stable over many cycles. The highest performing and most promising materials, MIL-53(Al), UiO-66(Zr), and NaY, were chosen for further studies in the next project objective.

Adsorbent sieves alone cannot be used in a practical system, and an inert support such as a porous polymer fiber is necessary to fully utilize the materials from objective 1. High capacity sorbent materials are combined with the advantages of polymer fibers to create a new platform technology for odorant removal from natural gas. MIL-53(Al) was eliminated from further investigation due to its inability to be incorporated into a fiber using the typical spinning conditions used to create these fibers. Both NaY/CA and UiO-66(Zr)/CA hybrid fibers were fabricated with high sorbent loadings (about 75 wt %) and exhibited high capacities and selectivities for the TBM in a model natural gas flow, while being stable to multiple temperature swing regeneration cycles. NaY/CA fibers demonstrated higher overall adsorption capacities than UiO-66(Zr)/CA fibers, while UiO-

66(Zr)/CA fibers demonstrated higher stability and selectivity. For low humidity or tightly controlled environments, NaY/CA fibers may be better suited for odorant removal, while UiO-66(Zr)/CA fibers may be more advantageous in high humidity or variable environments. The cyclic sulfur adsorption capacities of sorbents in their powder forms were also measured with a lower desorption temperature of 120°C, which decreased their uptake by 24-40% compared to desorption at a higher temperature of 200°C.

The breakthrough and equilibrium adsorption capacities of both zeolite and MOF hybrid fibers decreased with increasing model natural gas flow rate between 10-80 sccm, and also decreased with increasing adsorption temperature between 35-55°C. The mass transfer resistance was mainly controlled by the external mass transfer coefficient, which was lower than the internal mass transfer coefficient at almost every operating condition studied. The fibers were found to be stable in retaining high TBM uptake capacities over several cycles of adsorption and desorption. Further, fibers which had been stored under normal laboratory conditions for over one year were found to retain the same TBM capacity in the adsorption TGA even after this long-term ambient storage. Both immediate cyclic regenerability and long-term stability are important for a real application of this technology. The overall results from the three objectives demonstrate a proof of concept that fiber sorbent creation and implementation are feasible and worth further investigation for odorant removal from pipeline natural gas in an industrial setting.

CHAPTER 1

INTRODUCTION TO ADSORPTIVE DESULFURIZATION

Coal, petroleum, and natural gas are currently the three largest sources of energy in the United States[1] and worldwide.[2] The constant, rapid increase in energy demands coupled with energy independence and climate change concerns in the United States has encouraged the planned gradual conversion from coal-fired power plants to the cleaner alternative of natural gas fueled power plants for electricity generation. Natural gas plants often employ combustion turbines in a combined cycle with steam turbines to transform mechanical energy into electricity. While there is an ample supply of pipeline natural gas in the U.S. for this application, the combustion of trace amounts of sulfur odorants such as *tert*-butyl mercaptan (TBM) present in the fuel (typically 10 ppm or less) with alkali material from the environment results in a corrosive residue that reduces the lifetime and overall efficiency of the gas turbine.[3-4] Efficient removal of these sulfur compounds can relieve this problem and support the conversion from oil and coal to natural gas for electricity generation.

1.1 Current Energy Scenario

Electricity generation consumed 37.5% of the total energy produced in the U.S. in the year 2016, relying primarily on coal, nuclear, and natural gas as a supply. As seen in Figure 1, coal was the largest contributor that year at 13.0% of the total energy supplied

for electricity generation, followed by natural gas at 10.3% and nuclear at 8.42%.[1] Recently, a globally growing interest in clean energy and environmental sustainability has fueled a conscious effort to shift from coal to natural gas as an energy source when possible. Compared with coal usage at the power plant, natural gas produces half as much carbon dioxide (CO_2), less than one third as much nitrogen oxides (NO_x), and a negligible amount of other air pollutants such as carbon monoxide, sulfur dioxide (SO_2), soot or ash, mercury, and other heavy metals. Additionally, natural gas is easier to transport than either coal or oil, and has an increasing domestic supply in the U.S.[5]

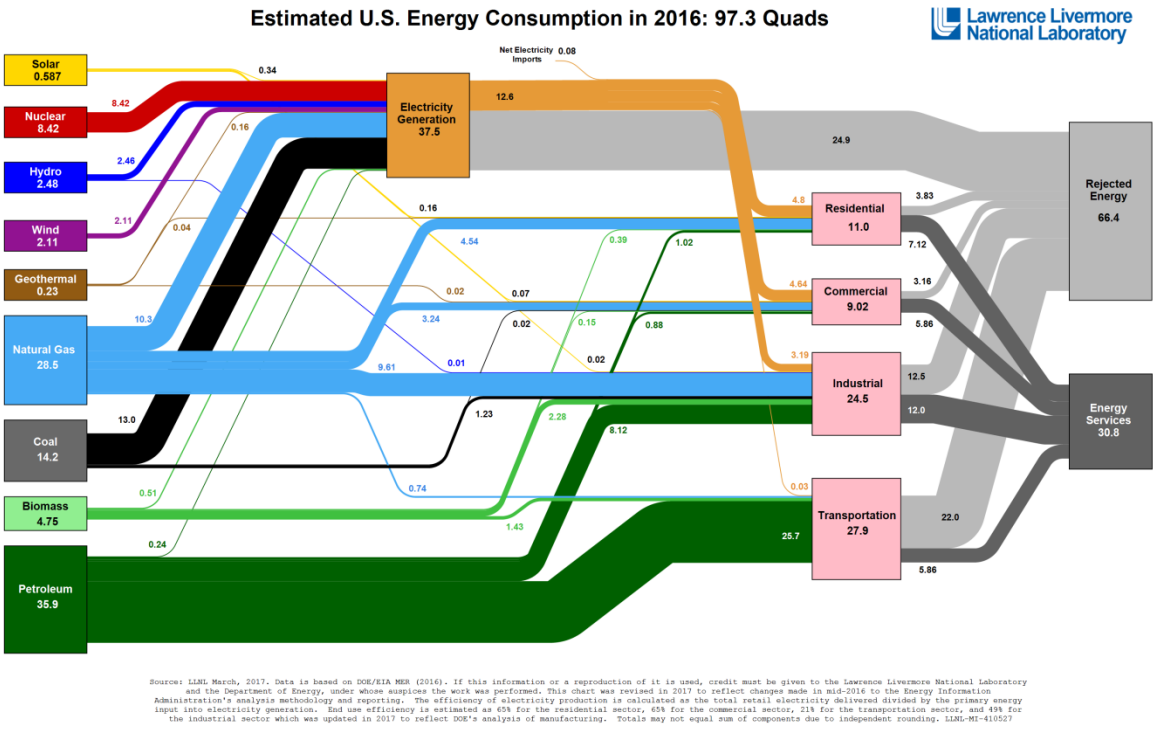

Figure 1: Energy flow diagram of the total energy supply and consumption in the United States in 2016. The left side indicates sources of energy while the right side indicates how much of each source is used in a particular sector. Almost 40% of the total energy consumed went towards electricity generation, and was supplied mainly by coal, natural gas, and nuclear sources. Source: Lawrence Livermore National Laboratory, 2016.

1.1.1 Growth of Natural Gas-Fueled Power Plants

Natural gas production in the U.S. is projected to grow significantly and continuously in the next few decades as the use of coal declines.[6] This effect, coupled with new power plant emissions regulations, will be largely seen in the electric power sector, as shown by the historical and projected growth in natural gas consumption for electricity generation in Figure 2.

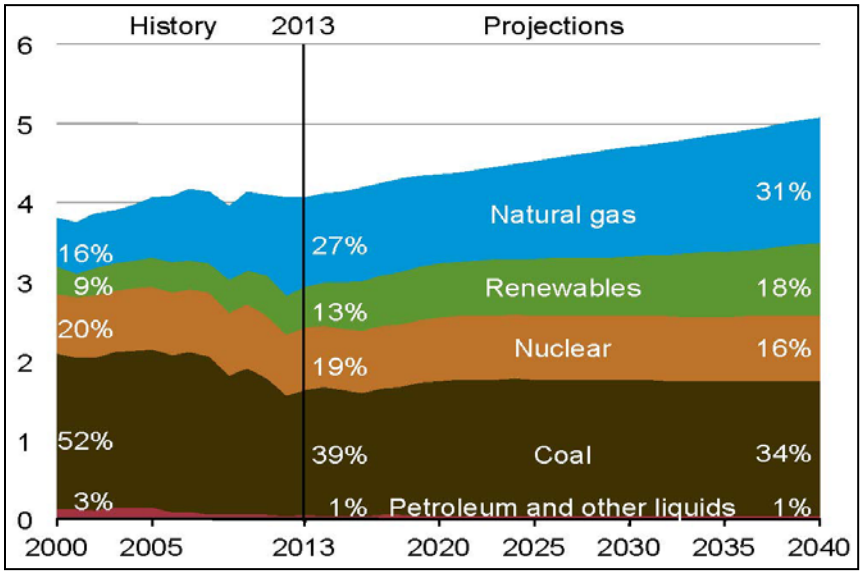

Figure 2: United States electricity generation by fuel type in trillion kilowatt-hours per year from 2000 to 2013, and projected onwards to 2040. Source: U.S. Energy Information Administration, Annual Energy Outlook, 2015.

Over 300,000 miles of natural gas transmission pipelines and supporting infrastructures have been built in the United States.[7] These pipelines, as shown in Figure 3, form a highly integrated cross-country network that can supply natural gas to almost any location for any purpose. An increasing number of new power plants built are fitted

for natural gas fuel,[8] in addition to current coal-fired power stations being replaced with natural gas units.[9]

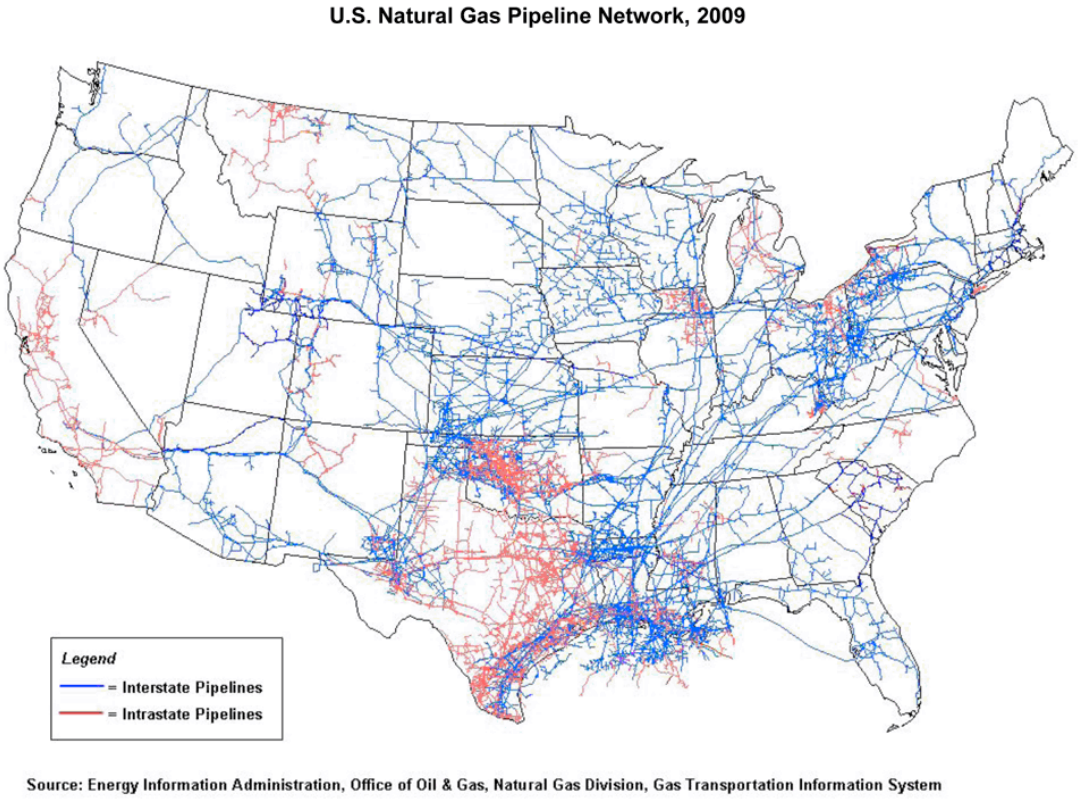

Figure 3: U.S. natural gas pipeline network, 2009. Source: Energy Information Administration, Office of Oil & Gas, Natural Gas Division, Gas Transportation Information System, 2009.

The most common method used commercially to generate electricity from natural gas is through a combined cycle power plant employing both a gas turbine and a steam turbine with a heat recovery steam generator, as shown in Figure 4. Combined cycle plants can be as high as 50-60% thermally efficient.[8] The gas turbine, or combustion turbine, uses hot, high pressure gases generated from the burning of pipeline natural gas in an excess of compressed air to spin the turbine blades and generate electricity through electromagnetic induction.

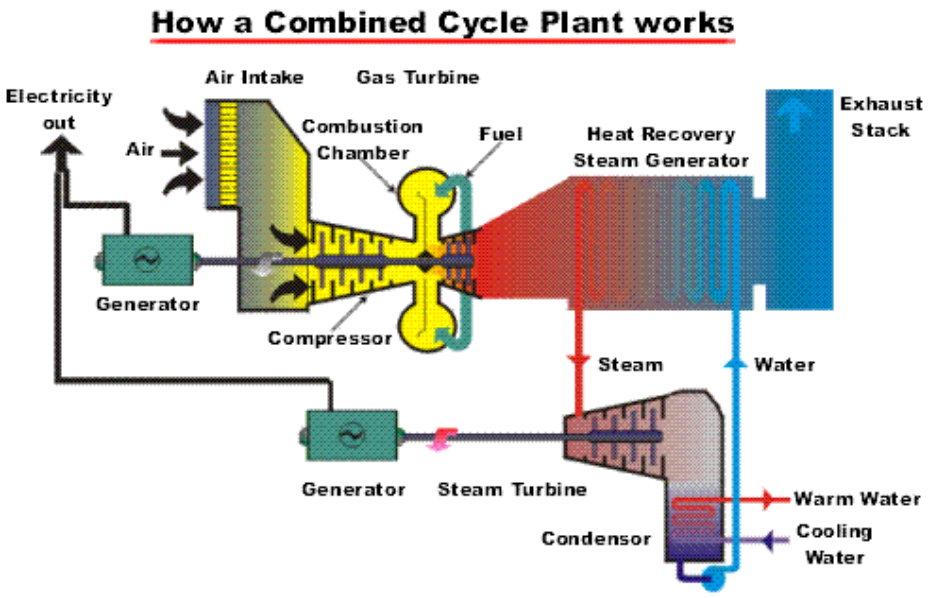

Figure 4: Diagram of a natural gas fueled combined cycle power plant. Source: Nooter/Eriksen Inc.

1.1.2 Corrosion in Gas Turbines due to Combustion of Sulfur Odorants in Pipeline Natural Gas

Leak detection of pipeline natural gas, composed mostly of methane, is difficult due to its colorless and odorless nature. Legislature in the U.S. and abroad mandates the use of trace amounts (ppm levels) of mercaptans as odorants in natural gas for ease of detection in the event of a gas leak. Based on the lower explosive limit (LEL) of natural gas in air (5%), regulations specify that the gas must be detectable by an average person at one-fifth of this limit, or at a maximum concentration of 1% in air.[10] While these mercaptans are useful for safety purposes, they are organosulfur compounds whose combustion products corrode gas turbines and the transmission / distribution pipelines in which they are used.

The combustion gas turbine in natural gas power plants can experience corrosion during use. This corrosion is largely caused by the combustion products of the sulfur present in the fuel reacting with alkali material such as salt (sodium chloride) taken in from the surrounding environment. This salt may come directly from seawater spray in offshore plants or from sea salt particles carried by the wind.[4] The combustion product is a molten reactive residue containing alkaline sulfates that settles and accumulates over turbine rotor blades, nozzle guide vanes, and other hot-section components, reacting with the oxide layer on the surface and destroying it.[4] Figure 5 shows three different types of hot corrosion that may happen on combustion turbine surfaces. The large amount of air taken in by a gas turbine for combustion results in a highly oxidizing atmosphere in the turbine's combustion zone, which also contributes to corrosion.[3] Even a small amount of sulfur in the fuel can effectively diffuse into the metal of the turbine and cause the accelerated oxidation-corrosion reaction commonly known as "hot corrosion."

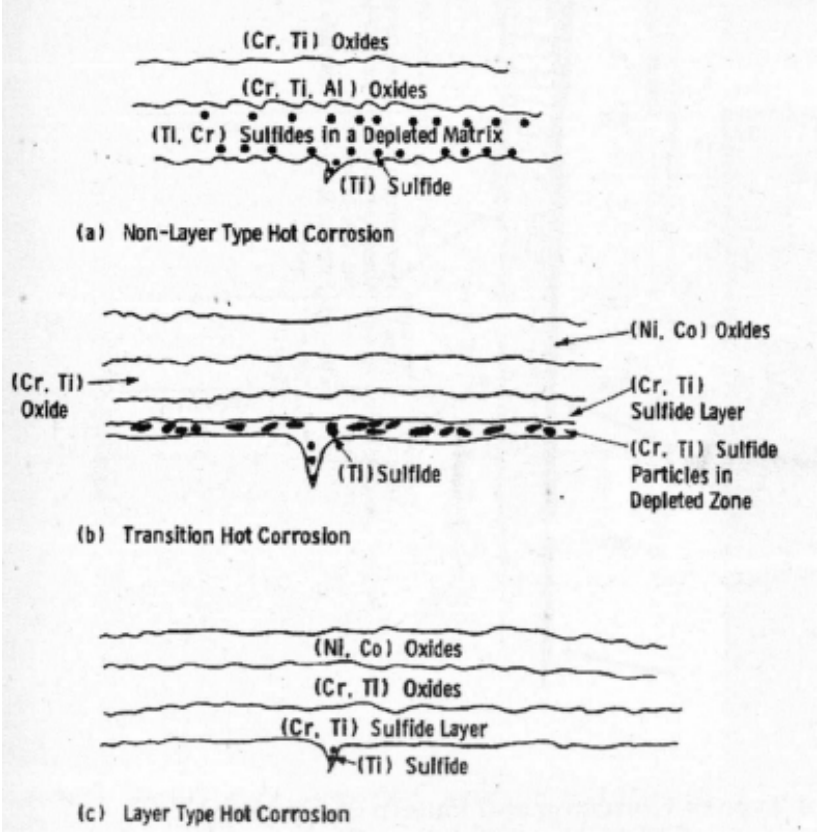

Figure 5: Schematic characterization of corrosion products found at areas typical of the three different hot corrosion regions. Source: Viswanathan R. *Case Histories on Integrity and Failures in Industry*, 1999.

Hot corrosion of combustion turbine surfaces reduces the overall turbine efficiency and lifetime through surface roughening and profile thickening of blades and other parts.[11-12] As shown in Table 1, combustion turbine corrosion, as well as corrosion of generators and transmission structures, costs industry millions of dollars per year.

Table 1: A short compiled list of the costs of corrosion problems affecting broad sectors of the electric power industry for 1998. Highest costs are listed first. The corrosion costs to the combustion turbine and transmission sector are substantial. Source: Corrosion Inspection and Monitoring, 2007.

Corrosion problem	Sector	$ Millions	Percent (%)
Turbine corrosion fatigue (CF) and SCC	Fossil and nuclear	792	6.75
Corrosion in electric generators	Fossil and nuclear	459	3.91
Flow-accelerated corrosion	Fossil and nuclear	422	3.60
Oxide particle erosion of turbines	Fossil	360	3.07
Corrosion of tower footings, anchor rods, and tower structures	Transmission	99	0.84
Hot corrosion of combustion turbine (CT) blades and vanes	Combustion turbine	93	0.79
Hot oxidation of CT blades and vanes	Combustion turbine	35	0.30
HRSG flow-accelerated corrosion and underdeposit corrosion	Combustion turbine	20	0.18
Heat recovery steam generator (HRSG) CF	Combustion turbine	20	0.17
Corrosion of CT compressor section and CT exhaust section	Combustion turbine	18	0.16
Conductor deterioration	Transmission	18	0.15
Corrosion of splices and shield wires	Transmission	18	0.15
Corrosion of substation equipment	Transmission	5	0.04

Figure 6 shows the widespread problem of corrosion in all types of economic sectors. Particularly of interest to this work are the corrosion of gas and liquid transmission pipelines costing approximately $7.0 billion dollars per year, the corrosion during gas distribution costing approximately $5.0 billion dollars per year, and the corrosion in the electrical utilities sector costing approximately $6.9 billion dollars per year. As such, there is a potential benefit to be derived from mercaptan odorant removal from natural gas prior to combustion in the gas turbine to prevent or delay corrosion

associated with SO_x production in the turbines. Additionally, for different applications, use of sulfur-free natural gas can also prevent deactivation in catalysts used for both exhaust gas cleanup and hydrogen production for fuel cells via steam reforming.[13]

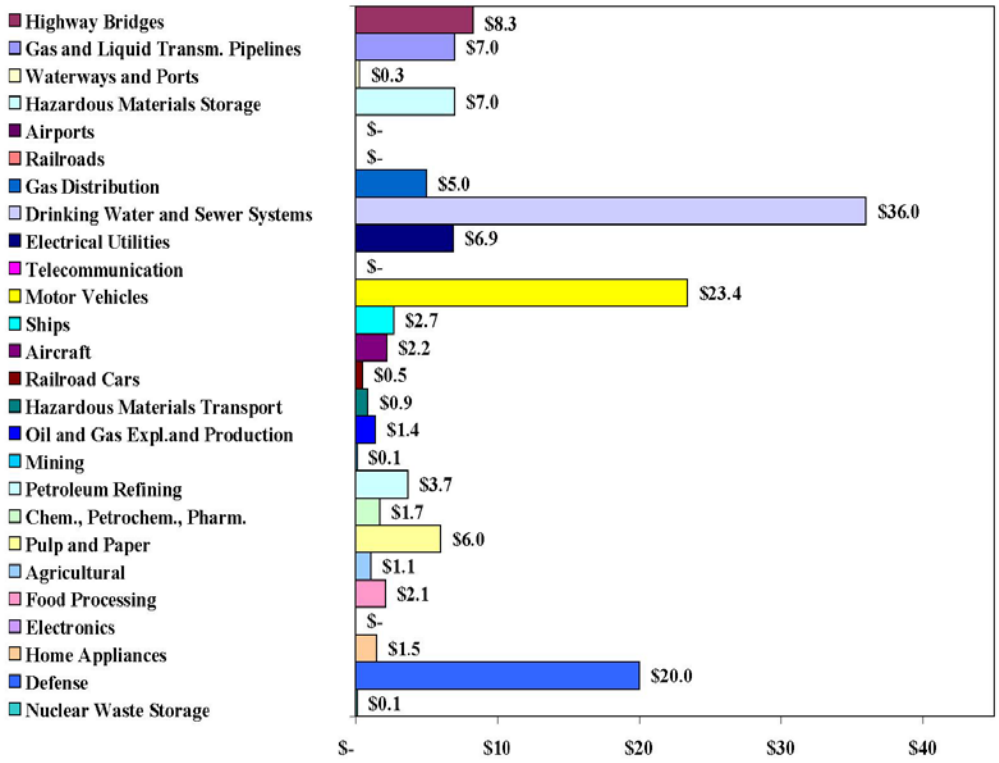

Figure 6: Cost of corrosion analyzed by economic sector in billions of dollars in year 2002. Source: NACE Cost of Corrosion Study, 2002.

Several corrosion prevention strategies have been proposed to combat corrosion and extend turbine lifetime. For light surface corrosion, reconditioning of the affected areas by cleaning and removing the chromium depleted zone can extend turbine life,[4] however, this requires on-going periodic monitoring by metallographic analysis or visual inspection to determine when reconditioning is necessary. This can be both time-consuming and costly, as it requires a complete shutdown and opening of the turbine for

an extended period of time. Another option is to use high temperature corrosion resistant alloys in the manufacturing of turbine blades and other parts, however, the process of selecting these alloys can be complex and time consuming and the most suitable material would be dependent on the operating conditions of the turbine. There is often disagreement over which alloys are best to use for any application. Misunderstanding and improper selection of alloys due to inconsistent studies can lead to equipment failure and corrosion, or conversely lead to the selection of a more expensive alloy than necessary.[3-4, 14] A third option is to remove sulfur and / or alkali compounds from both the fuel and the surrounding environment before introduction into the turbine, as hot corrosion requires both sulfur and an alkali to be present at high temperatures to form the corrosive residue. For the intake air, efficient air filters must be used to capture the trace amounts of salt and / or sulfur compounds (such as H_2S, COS, SO_2) before entering the compression chamber. This requires processing a large amount of gas, and the composition of ambient air is constantly changing such that it may be difficult to design a filter to sufficiently and selectively remove the desired compounds at all times. The final option would be to remove sulfur compounds from the natural gas. Much of the sulfur present in treated natural gas comes from the mercaptans added for safety, though a trace amount may also come from naturally occurring hydrogen sulfide impurities.[8] This method requires the processing of less gas than removing alkali from air and can be operated continuously and flexibly without shutting down the turbine. This option is the focus of this work, and will be discussed in more detail in the following sections.

1.2 Sulfur Removal from Pipeline Natural Gas

Much of the difficulty associated with sulfur removal from odorized natural gas comes from having to process the large quantity of high pressure gas to remove the ultra-low concentrations of odorants generally present. Some common techniques used to remove sulfur compounds from natural gas and other fuels are discussed below.

1.2.1 Catalytic Hydrodesulfurization (HDS)

A common method used to remove sulfur from natural gas and other fuels before combusting them is a two-step catalytic hydrodesulfurization process such as the one show in Figure 7. This is generally employed in the fuel refining process to reduce sulfur dioxide (SO_2) emissions from the exhaust gases of motor vehicles and other fuel combustion processes, as well as remove sulfur as a poisonous species in catalytic converters.[15] The process involves adding hydrogen to the sulfur compound in the presence of a Ni-Mo/Al_2O_3 or Co-Mo/Al_2O_3 catalyst to cleave the carbon-sulfur bond and replace it with a carbon-hydrogen bond with hydrogen sulfide (H_2S) produced as a by-product.[16] In the second step, the H_2S must then be removed through adsorption on an amine contactor, zinc-oxide, or other sorbent.[16-17]

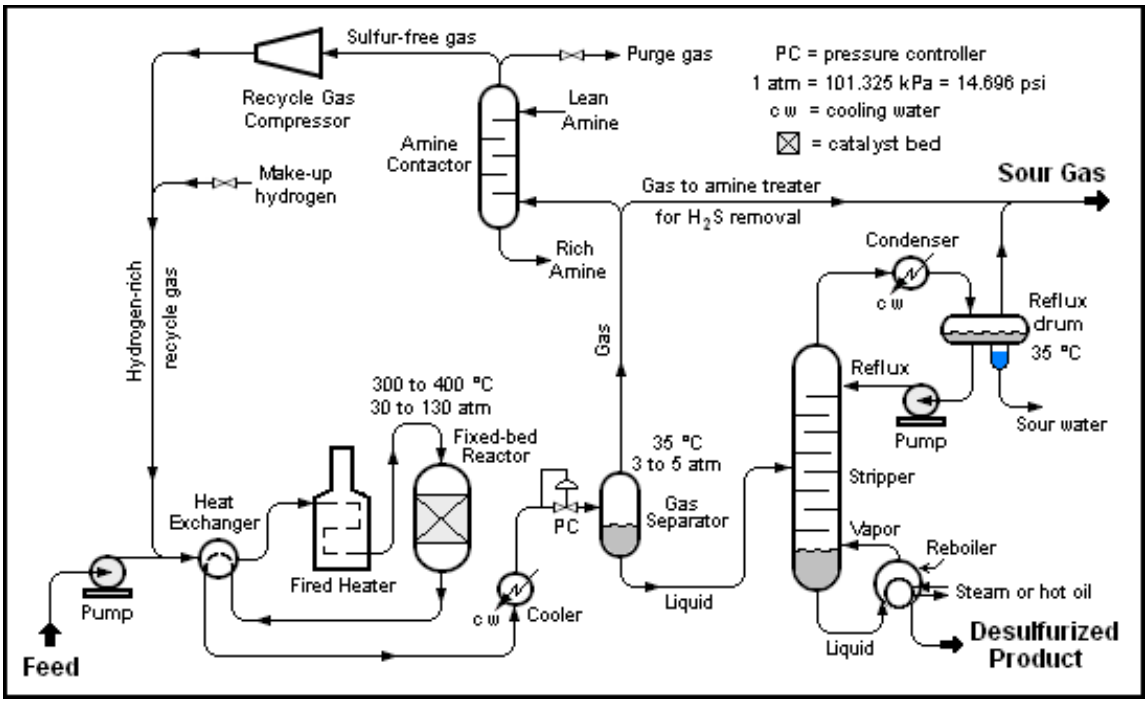

Figure 7: Schematic diagram of a hydrodesulfurization unit. The fuel feed is heated and pressurized before introduction into a fixed-bed reactor filled with catalyst where hydrodesulfurization happens. The H2S-containing hydrogen-rich product gas is treated with amines (or other sorbent) before being recycled back to the system. Source: Beychok, M. *Hydrodesulfurization*, 2006.

Industrially, the process takes place at high temperatures between 300-400°C and high pressures between 30-40 atms. This process is efficient in sulfur removal with high sorption capacities, and is good for treating large volumes of gas with long cycle times.[18] The drawbacks of this method are not only requiring a large and complex system setup, but is energy intensive and expensive due to the need to keep both the catalyst and the adsorbent at the elevated temperature, and the need to add and recycle hydrogen to the system.[16] Additionally, zinc oxide needs to be replaced periodically, the process requires a long time to start up, and it is generally not ideally suited for the removal of low concentrations of sulfur or small scale processes such as mercaptan removal from pipeline natural gas.[19]

1.2.2 Selective Catalytic Oxidation (SCO)

Another approach to sulfur removal uses activated carbon catalysts to selectively oxidize organosulfur compounds. For H_2S containing fuels, the products are water and elemental sulfur, which can then be separated from the fuel and sold.[20] An example of this process can be seen in Figure 8. For other organosulfur compounds, the electrophilic addition of oxygen to the sulfur atoms produces sulfoxides and sulfones, which can also be easily removed from the fuel stream. Air is commonly used as an oxidant for its oxygen content, but peroxides, peracids, and alkanols have also been used.[21]

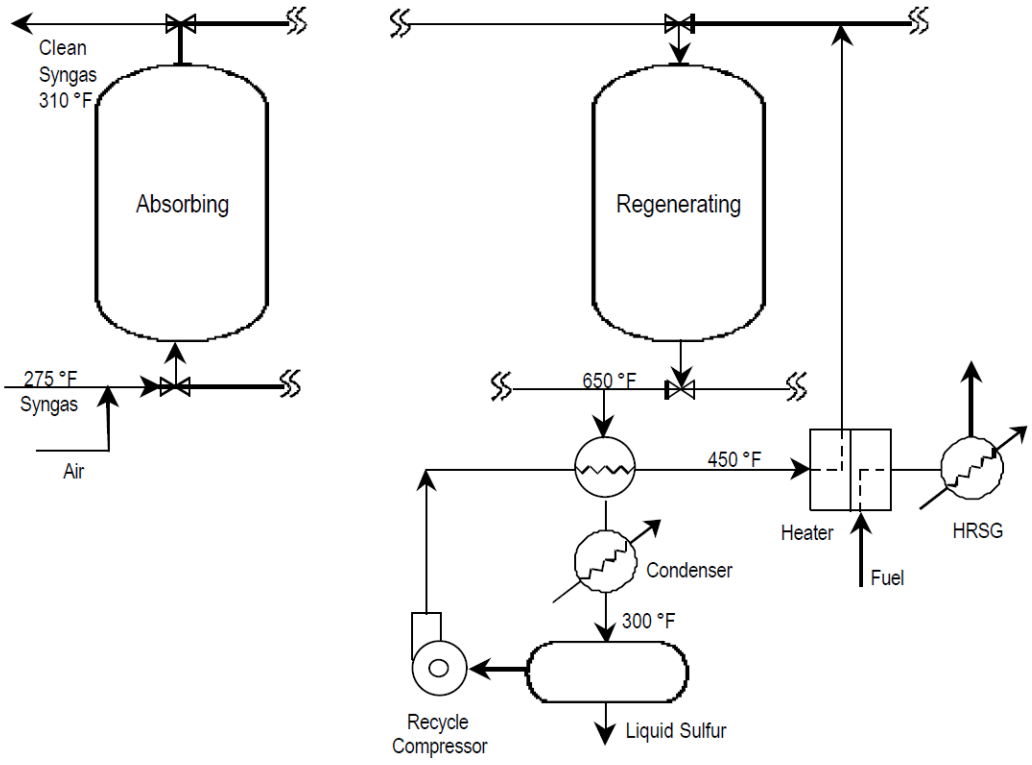

Figure 8: Simplified diagram of a selective catalytic oxidation process for H_2S removal. The heated fuel feed (depicted as syngas in this example) is mixed with air before introduction into a fixed-bed reactor filled with microporous catalyst where oxidation happens. The elemental sulfur product is continuously stored within the catalyst pores until they are saturated, at which point the catalyst is thermally regenerated with high temperature nitrogen. Source: DOE-NETL Proceedings Accession Number DE2004-832829, 2004.

This process requires the addition of heat to operate at temperatures of 150-280°C.[22] It is good for removing trace amounts of H_2S and other organosulfur compounds from gas streams and the process can operate continuously.[20, 23] However, the formation of poisonous byproducts such as SO_2 and COS and the need for their removal is an additional problem,[18, 23] and heating the catalyst bed for both the reaction and regeneration process is energy intensive.

1.2.3 Adsorption on Solid Sorbents

The last major approach for sulfur removal from fuels is selective adsorption on solid adsorbents such as metal oxides, activated carbon, zeolites, and metal organic frameworks (MOFs). This method does not convert the sulfur compounds to a different species before separation; instead, the acidic sulfur compounds are simply adsorbed onto the surface by its attraction to the basic surface sites of the adsorbent.[16, 24] There are two common modes of operation: temperature swing adsorption (TSA) process with low temperature adsorption and high temperature desorption, and pressure swing adsorption (PSA) process with high pressure adsorption and low pressure desorption.[25] Both kinds of desorption serves to regenerate the sorbent for subsequent cycles of adsorption. An example of TSA is depicted in Figure 9.

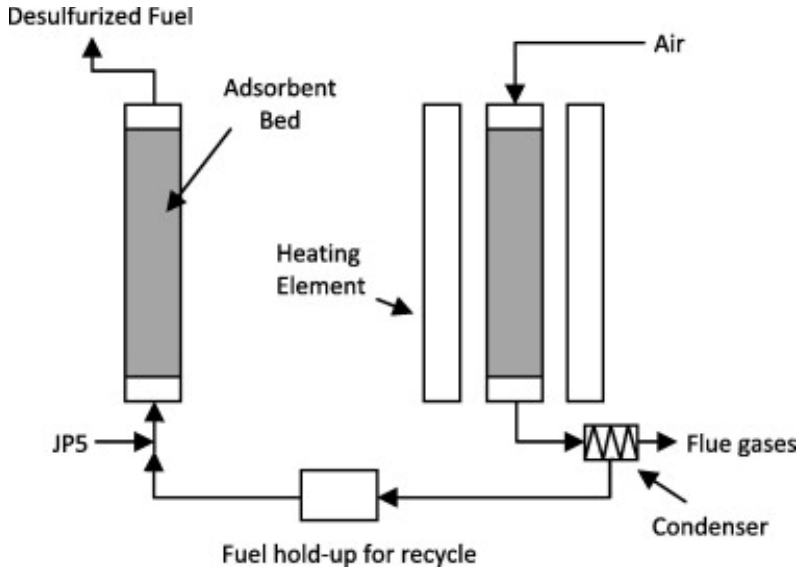

Figure 9: Schematic diagram of a laboratory scale adsorption-regeneration unit used for desulfurization using TSA. The fuel (depicted as JP5 in this example) is fed into a column packed with sorbent, where the sulfur compounds are adsorbed until breakthrough. Desulfurized fuel comes out of the back end of the bed. During desorption, the bed temperature was raised to 450C while air flowed through as a stripping medium. Source: Fuel 89(11), 2010

Selective adsorption is an attractive technology for this application due to its ability to be operated at ambient temperatures and pressures, with only high pressures needed for the adsorption cycle of a PSA process and high temperatures needed for the desorption cycle of a TSA process. This makes the process more energy and cost efficient than either HDS or SCO. This process is also good for removing trace amounts of sulfur from fuel, something that HDS is unable to offer.[24] Overall, the process is also simpler; no hydrogen gas is necessary and the sulfur compounds do not get converted to other hazardous products so there is no need for a second separation step to remove byproducts. Sorbents may also be regenerated by heating and / or purging with a flowing gas stream and used continuously over many cycles of adsorption and desorption. The drawbacks are that sulfur uptake capacity on the sorbent is often low, so that large quantities of sorbent are required[18] and there may be difficulties in selecting an

appropriate sorbent. Selectivity for the sulfur compounds over the fuel can also be a problem. Overall though, the advantages that solid sorbents offer to efficiently and effectively remove sulfur from fuels significantly outweigh their disadvantages, and this technology is explored more in the following sections.

1.3 Materials and Methods for Selective Adsorption

Some common solid sorbents used in selective adsorption of sulfur compounds from fuels include ion-exchanged or metal-containing zeolites, metal organic frameworks, supported metals, metal oxides, metal-containing aluminum oxide, activated carbons, and modified mesoporous silica.[19, 22, 24, 26-46]

Activated carbons have been extensively studied for desulfurization by adsorption, and are relatively inexpensive with high surface areas and pore volumes. The capacity of activated carbon is determined by physical, porous, and chemical structure, and can be increased by metal impregnation or oxidation.[22] Unfortunately, the sulfur capacity of activated carbons at ambient temperatures is generally lower than that of other porous materials, such as zeolites, even with a capacity boost facilitated by the addition of metals and oxides, and can become pyrophoric during the regeneration step.[22, 40, 46] A lower temperature (around 200°C) is needed for full regeneration of activated carbons compared to zeolites.[27] Similar other ion-exchanged materials, different types of metal modified activated carbons will be differently selective for sulfur compounds, and will have varying degrees of desulfurization performance depending on the composition

of the sulfur-containing fuel. These sorbents have been mainly used for the adsorption of sulfur compound from liquid fuels.[22, 24, 36, 40, 44, 46]

Zeolites are well-studied, attractive sorbents due to their large pores and surface area, polarity, high thermal stability, and surface acidity and basicity that lead to high removal ratios and capacities.[19, 37, 41-42, 44-45] Zeolites X, Y, ZSM-5, Beta, and USY, among others, have all been used successfully in many studies for adsorbing various sulfur compounds from different fuels.[17, 19, 24] The exchange of ions and metals such as Cu^{+}, Ag^{+}, Zn^{2+}, Na^{+}, Fe^{2+}, $AgNO_3$, Ag-Mn, and others typically increases the desulfurization performance of the zeolites, though the performance and selectivity is as much dependent on the composition of the sulfur and fuel species present as on the composition of the zeolite.[16, 47] The capacity of ion-exchanged zeolites is generally higher than that of activated carbon and metal-containing activated alumina, but some can be difficult to apply under water containing conditions due to their hydrophilicity.[16, 41] The sulfur capacity of strongly hydrophilic zeolites such as X and Y, decreases significantly in the presence of trace amounts (1000 ppm) of water because of the higher binding energy for and selectivity toward water over sulfur.[37, 41] Because pipeline natural gas typically contains 80 ppm of water, this selectivity problem with NaY presents a substantial hindrance to implementation in a real system. Exchanging the ions in these hydrophilic zeolites with silver, manganese, and / or copper can improve the sulfur capacity in the presence of water up to a certain level, but the capacity of these ion-exchanged Y zeolites continuously decreases with subsequent adsorption cycles because of the strong, only semi-reversible binding between organosulfur molecules and the exchanged ions.[47-48] Less hydrophilic zeolites, such as ZSM-5, have capacities and

removal efficiencies that are more resistant to adverse water effects in high humidity conditions, but may have lower capacities overall.[47] Zeolites can be easily regenerated with heat or pressure reduction in air or an inert gas.[27, 49-50]

Metal oxides are highly efficient at removing sulfur in fuel down to sub-ppmv levels, but require high temperatures to do so.[24, 35] Manganese oxide specifically is easily reduced at high temperatures so the range for temperature swing desorption is limited.[19] Also, metal oxides alone do not have a high sulfur capacity when compared to other sorbents.[41] A combination of metal-exchanged metal and aluminum oxide ($Cu/ZnO/Al_2O_3$) can have greater sorption capacity than either metal-exchanged metal oxide (Cu/ZnO), metal-exchanged aluminum oxide (Cu/Al_2O_3), or any other configurations (ZnO/Al_2O_3, ZnO).[16, 35] Activated alumina alone has good adsorptive properties but tends to have a lower selectivity for sulfur compounds over fuel species. Supported metals have a high sulfur capacity, but also require operating at high temperatures around 200˚C to reach these capacities.[24]

Metal modified mesoporous silica adsorbents show higher capacity than mesoporous silica without modification, but overall, the capacities are still generally lower than that of metal-exchanged zeolites. Such modified adsorbents can be regenerated at low temperatures around 100°C and the absence of aluminum should make them more water resistant.[26-27]

Metal organic frameworks, or MOFs, are a relatively new class of porous hybrid materials characterized by metal ions linked with organic bridging ligands that have been studied for the adsorption of thiophenes from liquid fuels such as gasoline, diesel, and jet fuel, as well as the adsorption of several types of hazardous sulfur-containing compounds

from both liquid and gas mixtures.[29-30, 33-34, 38-39, 51-54] MOFs have the potential to surpass current adsorbents, including benchmark zeolites, in terms of their high capacity and selectivity for sulfur compounds because of their high surface areas, pore volumes, and tunability. Cu-BTC was one of the first of these materials to be identified as having a remarkably high capacity for various organosulfur compounds in liquid fuels, surpassing that of zeolite Y.[30, 38-39, 53] Others identified later for this application are MIL-53(Fe), MIL-53(Al), MIL-53(Cr), MIL-47(V), MOF-5, CPO-27, MIL-100, and MIL-101,[30, 33-34, 39, 51, 54-57] some of which were also shown to display higher sulfur uptake capacities than zeolite Y. While there have been many studies on MOFs for the adsorption of liquid sulfur compounds, such as benzo-, dibenzo-, and 4,6-dimethyldibenzothiophenes from liquid fuels, and MOFs for the adsorption of other sulfur-containing gases, such as hydrogen sulfide[58-59] and sulfur dioxide,[60] there has been relatively little published work on the adsorption of gaseous sulfur odorants from gaseous fuels. Only a few studies concluding that Cu-BTC and MOF-199 may be good candidates for adsorbing gaseous tetrahydrothiophene, displaying higher capacities than that of commercial activated carbons, have appeared.[61-62]

The ability of solid sorbents to remove trace amounts of sulfur from fuel and for the process to operate at low temperatures and pressures gives them a significant advantage over traditional hydrodesulfurization and catalytic oxidation approaches. Adsorption is also relatively simple compared to the other two processes. Unfortunately, the energy savings gained from low operating temperatures and pressures can be counterbalanced by the use of the sorbents in pellet packed beds. Traditionally, for industrially practical systems, sorbents are formed into pellets with an inert binder

material and packed into stationary beds. The beds are temperature or pressure controlled columns where gas is fed into one end of the bed and the species of interest is adsorbed through its contact with the pellets, such that the exit gas is free of the adsorbed species. Figure 10 (left) illustrates the configuration of a typical pellet packed bed adsorber. As discussed previously, these beds may be operated in either temperature swing adsorption (TSA) or pressure swing adsorption (PSA) mode. TSA is typically preferred for the adsorption of trace impurities.[63] Flow through these packed beds often results in high pressure drop and particle attrition, especially at higher volumetric feed flow rates and smaller pellet sizes.[64-65] In order to lower the pressure drop in packed beds for applications with large flow rates, the flow would have to be significantly decreased or the sorbent pellet size would have to be increased.[64] Additionally, the pellet packed bed configuration can be difficult for heat and mass transfer equilibration, leading to long cycle times and underutilization of the sorbent.[65]

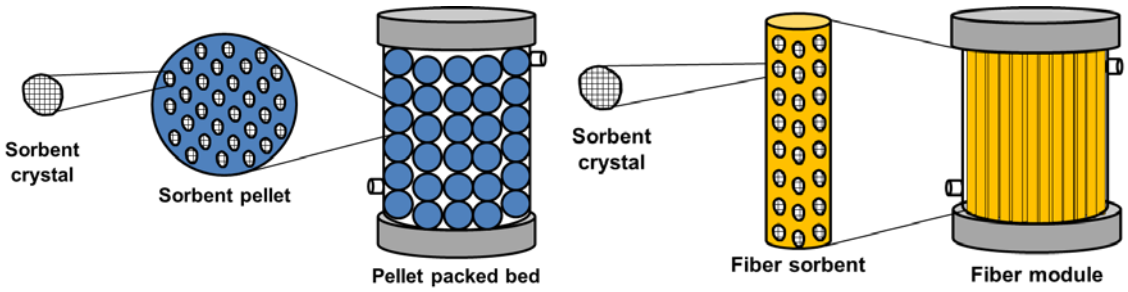

Figure 10: Pellet packed bed configuration (left) versus fiber sorbent configuration (right).

Fiber sorbents and extruded monoliths are two relatively new classes of gas and liquid separation materials that offer many potential advantages over conventional pellet packed beds in some cases. In such alternative configurations, porous sorbent materials

such as zeolites and MOFs are directly spun into[66-68] or grown on the surface of [69-70] polymer fibers, or in the case of monoliths, directly formed through extrusion[71-72] or coated with a sorbent film on the surface,[73-74] instead of pressed into pellets. The focus of this work is on fiber sorbents, which can be bundled into modules similar to that of a packed bed or monolith, as illustrated in Figure 10 (right). Fiber-based sorbents have been shown previously to offer significantly lower pressure drops due to simpler and more reliable flow patterns through the modules[75-76] than packed bed adsorbers, as well as better heat and mass transfer rates due to higher surface area/volume ratios.[12, 77-78] Additionally, particle attrition and pellet size distribution are avoided in a fiber sorbent module, which helps in producing sharper breakthrough curves[65] and improved durability. Fiber sorbent modules and their many potential advantages will be discussed in more detail in the following section.

1.4 Research Objectives

The overall goal of this thesis work was to create a hybrid fiber sorbent module system to selectively remove mercaptan odorants from pipeline grade natural gas. Sulfur-free natural gas is useful for preventing corrosion in gas turbines and for hydrogen production using catalysts. These fiber sorbents, combining the high sulfur capture capacity of powder adsorbents with the cost effectiveness and ease of manufacturing of established fiber production, were synthesized, characterized, and tested for adsorption of *tert*-butyl mercaptan (TBM, a common odorant) in a model natural gas in this work. The

fiber sorbents comprise porous solid polymer fibers embedded with a zeolite or MOF sorbent, bundled together into a module as shown in Figure 10 (right). The fiber sorbent module system was operated in TSA mode with model natural gas passing over the fibers at ambient temperatures and pressures. Hot regeneration gas and a cooling gas were used for regeneration and cooling of the fibers respectively.

In previous work for a Master's thesis, the main objective was to design, optimize, and perform a technoeconomic analysis of fiber sorbent modules for selective and continuous TBM removal from natural gas, as well as assess their advantages over other conventional and developing technologies. The insights gained from that evaluation of fiber sorbents guided the PhD work presented here.

Objective 1: Investigate the ability of several MOFs and zeolites to selectively adsorb TBM from both a mercaptan / inert gas feed and a model natural gas feed.

The first objective of this work was to synthesize several different MOFs and gravimetrically screen and compare them along with several commercially purchased zeolites for TBM adsorption capacity. The MOFs were chosen not only based on their potential high TBM uptake capacity and selectivity, but also practical factors such as stability toward liquid water, regenerability, and ease of synthesis and / or commercial availability. The performance of the best candidates, MOFs MIL-53(Al), Cu-BTC, and UiO-66(Zr), were then compared to a benchmark zeolite material, NaY, and further evaluated with regard to their cyclic regenerability and stability, and selectivity toward TBM over methane and other impurities contained within pipeline natural gas.

Objective 2: Fabricate and evaluate hybrid fiber sorbents with high sorbent loading and desired separation properties.

From objective 1, zeolite NaY and MOFs MIL-53(Al) and UiO-66(Zr) emerged as good candidate materials for further investigation with fiber creation. The second objective was to evaluate the ability of these chosen materials to be spun into a hybrid cellulose acetate (CA) polymer fiber and determine appropriate regeneration temperatures. Further, the performances of these hybrid fibers were again evaluated on the basis of TBM sorption capacity and selectivity, as well as fiber stability and regenerability. The performance of these novel MOF-polymer hybrid fibers was measured against conventional zeolite-polymer fibers as well as their sieve counterparts.

Objective 3: Assess the performance and stability of fiber sorbents in a cyclic temperature swing adsorption (TSA) system in a module configuration.

The third objective was to package the fiber sorbents into modules and test their adsorption performance in a laboratory scale temperature swing adsorption system. The system operating conditions of adsorption temperature and feed gas flow rate were varied to study their effects on adsorption behavior. To check short-term stability, the fibers were regenerated and cycled through several phases of TBM adsorption and desorption. To assess long-term stability, fibers which had been stored under normal laboratory conditions for over one year between their creation in objective 2 and their use in

modules in objective 3, were retested in the adsorption TGA under the same conditions. This final objective ties together the two major challenges of materials design and system implementation, which pushes forward the development of an industrial scale fiber sorbent TSA system for odorant removal from pipeline natural gas.

CHAPTER 2

BACKGROUND AND THEORY

Fiber sorbents are organic-inorganic composite materials that can be made using a dry-jet, wet-quench technique to incorporate a powder adsorbent such as a zeolite or MOF into a continuous porous polymer support matrix with desired gas or liquid separation properties.[79] The typically inexpensive and commercially available polymer gives the fiber its structure and flexibility while the zeolite or other filler performs the separation through selective adsorption of the species of interest, as discussed in previous sections. These fiber sorbents have been previously spun with high sorbent loadings of up to 75 wt%.[78]

In many cases, fibers are spun in a hollow form, with a water and gas impermeable barrier layer added to either the bore side or shell side of the fiber to enable thermal cycling.[77] This barrier layer allows for a heating or cooling fluid to be passed through or around each of the fibers to control the temperature and keep the process isothermal during adsorption and desorption. The feed and sweep gases are then passed on the other side.[80] In adsorption mode, for example, the feed gas may be passed over the shell of the fibers as a cooling fluid such as water is passed through bore of the fibers to accept the heat of adsorption and keep the fibers isothermal throughout the adsorption. Subsequent heating/desorption and cooling steps also use the barrier layer configuration with a heating or cooling fluid such as steam or hot and cold water, and an inert sweep

gas over the fibers to desorb the adsorbed species and then return the fibers back to the sorption temperature.[80]

For alternative cases such as odorant removal from natural gas where there are trace amounts of the adsorbing species in an otherwise inert or non-adsorbing gas feed, the overall heat of adsorption may be so low that the fibers stay practically isothermal during the adsorption step even without the use of a cooling fluid. In this case, the fibers can be spun as porous "solid" fibers instead of hollow fibers, and hot and cool inert gas streams flowing over the fibers can be used for the subsequent regeneration steps instead of water or steam.[12] This modification makes the fiber spinning process, the module fabrication process, and the actual separation process much simpler.

2.1 Potential Advantages of Fiber Sorbent Module Adsorption System

Fiber sorbent modules can offer several advantages over traditional beds packed with spherical pellets. One of the most important advantages is a lower pressure drop across the bed due to a simpler flow pattern.[65] This is important for maintaining the high delivery pressure of the pipeline natural gas so that no additional pumps or compressors are needed to feed the gas to the turbines, therefore reducing the operating cost.[12] Another advantage is faster heat and mass transfer equilibration times due to the smaller critical dimensions that can be achieved for fibers as well as a more uniform flow path.[12, 65, 81] The above advantages are valuable for high flow rate applications such as pipeline natural gas where large volumes of gas must be processed quickly and continuously. Because of the more uniform flow path in a fiber module as compared with a pellet

packed bed, channeling and dead spaces within the fiber bed are minimized.[64] Due to the rapid equilibration times and lower pressure drop (which also scales with velocity in both pellet and fiber systems), smaller (or fewer) beds are needed for fiber sorbents than for pellets to process the same amount of gas.[12]

As mentioned previously, a thermal cycling method known as temperature swing adsorption (TSA) is ideal for feed gases with low concentrations of adsorbate, and full regeneration of some adsorbent materials is possible in various regeneration media. For TSA, hot purge gases such as air, nitrogen, a fraction of the purified hydrocarbon feed gas, and steam (for hollow fibers with a barrier layer) have all been successfully employed for regeneration of zeolite sorbents. The final choice depends on process specifications, safety considerations, available space, and a balance between capital and operating costs. Figure 11 shows the envisioned adsorption, regeneration, and cooling steps that comprise one full TSA cycle in a fiber sorbent module for this application.

The top left bed shows the first step, adsorption, where pipeline natural gas is fed at the inlet of the module while treated (TBM-free) product gas exits on the opposite end. The top and bottom right beds show the second step, regeneration, where hot regeneration gas is fed at the inlet. Initially, the regeneration gas will displace the interstitial gas left over from the adsorption step. Then, the fibers will be heated to the selected desorption temperature by hot gas and TBM will be desorbed and carried out of the bed as a TBM-rich waste gas stream. The bottom left bed shows the third and final step, cooling, where cooling gas is fed at the inlet of the bed to return the fibers back to the adsorption temperature while the same cooling gas simply exists at a higher temperature.

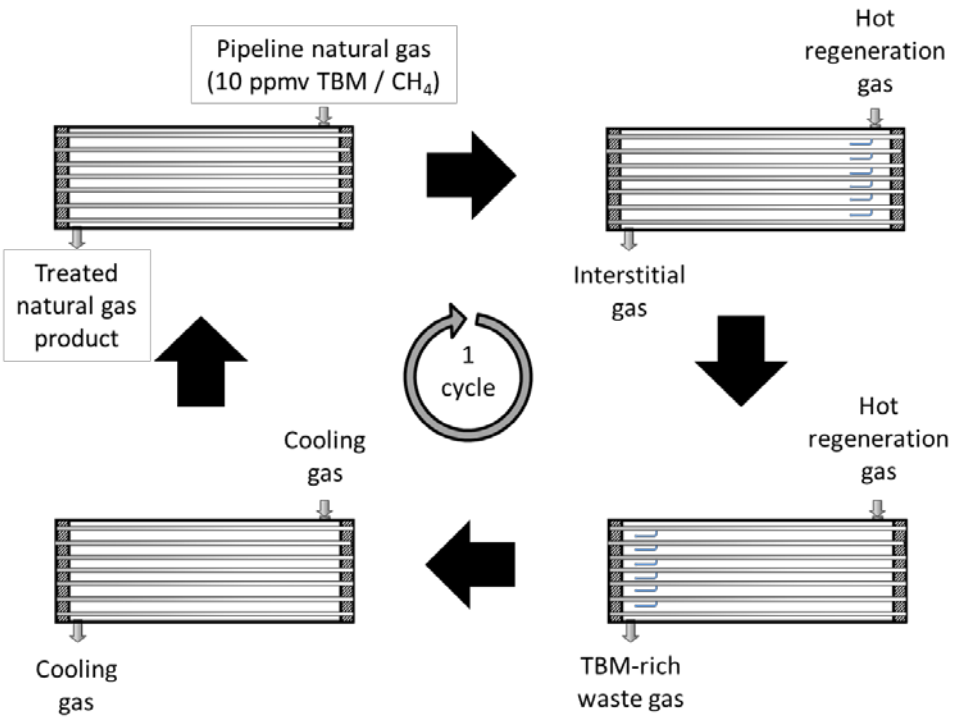

Figure 11: Schematic of the inlet and outlet gas streams of a solid porous fiber bed cycling through the continuous steps of adsorption and desorption.

To handle the large amount of natural gas needing to be processed, the incoming stream would need to be split among many fiber sorbent modules in parallel for the adsorption step. To make the process continuous, additional fiber modules would need to be used with staggered start-up and careful timing, such that some modules are in adsorption mode while others are in desorption mode to ensure all beds remain active. An example of this is illustrated in Figure 12.

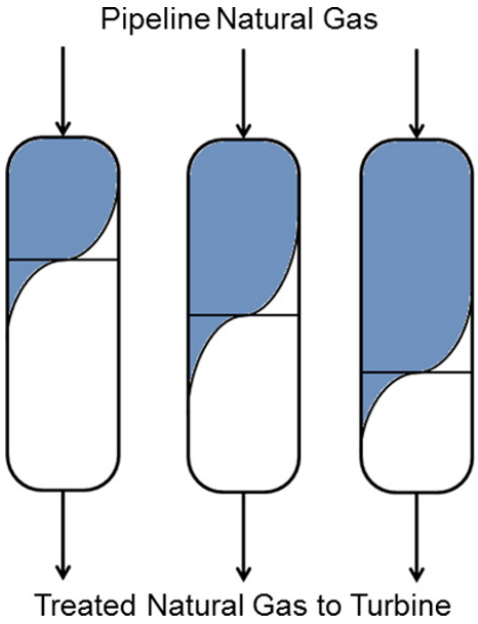

Figure 12: Difference in front positions of the three adsorption beds with staggered start-up.

Previous work examining the overall process design and capital and operating costs associated with fabricating and implementing a fiber sorbent system for TBM removal from pipeline natural gas turbines has determined the process to be economically feasible when compared to the cost of turbine replacement.[12] The potential savings as functions of original turbine lifetime and years of life extension brought about by implementing the fiber sorbent system ahead of the gas turbine is shown in Figure 13. Savings are greatest when the original turbine lifetime (without implementing the TBM removal system) is short and the life extension with TBM removal system implementation is long.

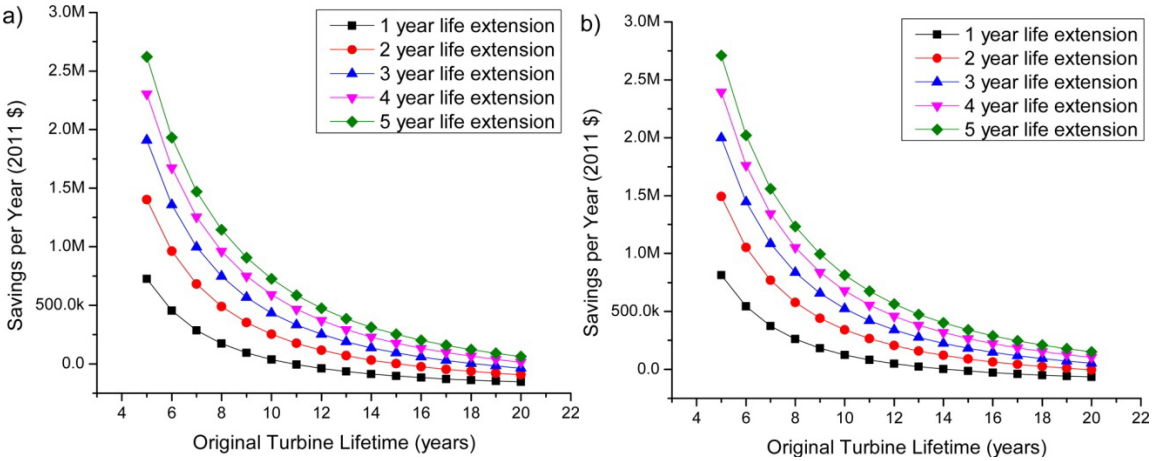

Figure 13: Potential savings per year by implementing the fiber sorbent system as a function of original turbine lifetime and length of turbine life extension (a) without heat integration and (b) with heat integration. Negative values indicate a net cost rather than savings. Source: Ind. Eng. Chem. Res. 53, 2014.

2.2 Transport Properties of Fiber Sorbents

The transport properties of porous solid sorbents usually determine their adsorption and desorption rates. Two major transport mechanisms that are commonly present with fiber sorbents are: molecular diffusion and Knudsen diffusion. Molecular diffusion occurs in the external boundary layer surrounding the fiber and within large pores of the fiber. Knudsen or transition diffusion occurs within small pores of the fiber and within the pores of the individual sorbent particles.[81]

There are three distinct regions for gas transport in and around a fiber sorbent: external, internal meso or macropore, and internal micropore. High surface area zeolite crystals (particle sizes typically 1 μm) intrinsically contain small, uniform micropores. Traditionally, these crystalline powders are compressed into pellets (diameters typically 1-3 mm) with or without an inert binding material to decrease the pressure drop in packed

bed adsorbers, which forms a new network of macropores from the intergranular void space.[82] In this work, the zeolite powder will be spun into porous polymer fibers (diameters typically 100-400 μm) such that the macropores will be located within the void space of the fibers. As discussed previously, the use of a fiber sorbent morphology rather than pelletized sorbents has the advantage of decreasing the pressure drop even more.

The three regions for gas transport are depicted in Figure 14. The first region involves the diffusion of the adsorbing species through a stagnant boundary layer that surrounds the external surface of the sorbent. The transport within this region is referred to as the external, or interphase diffusion. The second region involves diffusion of the adsorbing species through the meso and macropores of the fiber, while the third region encompasses diffusion of the species through the micropores of the powder adsorbent, in this case, zeolite. Transport within the second and third regions are referred to as internal, or intraphase diffusion. Both external and internal transport regions may provide significant resistances when considering adsorption rates.[82-83]

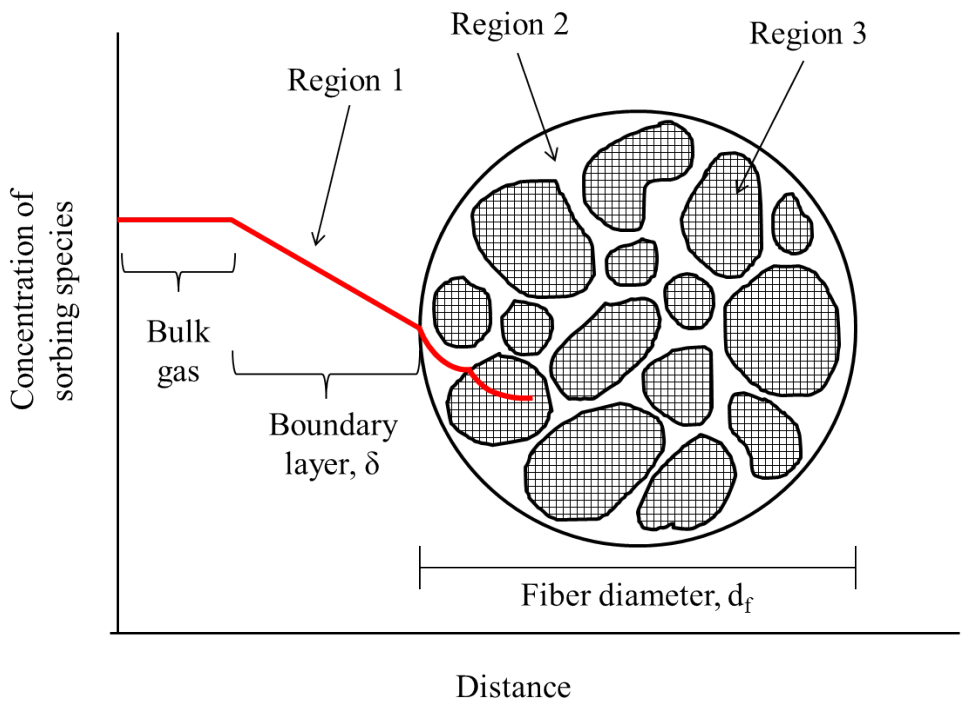

Figure 14: General concentration profile of the sorbing gas species around and within the cross-section of a porous fiber sorbent (figure lengths not drawn to scale). The three main regions for mass transfer are indicated. Region 1 depicts external diffusive mass transport through the stagnant film (or boundary) layer surrounding the fiber. Region 2 depicts internal diffusive mass transport through fiber meso and macropores. Region 3 depicts internal diffusive mass transfer and subsequent adsorption onto zeolite crystal micropores.

2.2.1 External (Bulk) Transport through the Boundary Layer

External or bulk diffusion involves the transport of gas molecules from the bulk gas stream to the outer surface of the sorbent. The diffusion occurs through a stagnant boundary layer of thickness δ that surrounds the fiber sorbent. Fick's First Law can be written for a two component gas mixture for this region of transport:

$$\nabla C_A = \frac{1}{D_{AB}}\left[X_A(N_A + N_B) - N_A\right] \quad (1)$$

where C_A is the concentration of species A, D_{AB} is the diffusivity of species A in B, X_A is the mole fraction of species A, and N_A and N_B are the fluxes of species A and B respectively. When equimolar counter-diffusion or a very dilute concentration of species A is assumed, equation (1) simplifies to:

$$N_A = -D_{AB}\nabla C_A \tag{2}$$

Further assuming a very thin boundary layer relative to the radius of curvature of the fiber, the equation can be simplified to just one dimension. Solving that equation with the appropriate boundary conditions returns the flux of species A through the film layer in the direction of interest (denoted as x here):[82]

$$N_{Ax} = \frac{-D_{AB}}{\delta}(C_{A\delta} - C_{AS}) \tag{3}$$

where δ is the boundary layer thickness, and $C_{A\delta}$ and C_{AS} are the concentrations of species A in the bulk gas phase and at the surface of the sorbent respectively. The magnitude of the boundary layer thickness is unknown, such that a mass-transfer coefficient is typically used instead.

Molecular Diffusion

Molecular diffusion occurs when collisions between the diffusing molecules dominates the mass transport, such as in the external boundary layer. Molecular diffusivity, D_M or D_{AB} in a two component gaseous system can be fairly accurately calculated from the Chapman-Enskog equation as follows:[82, 84]

$$D_M = D_{AB} = \frac{1.858\times10^{-27}T^{3/2}}{P\sigma_{12}^2\Omega}\left(\frac{1}{M_1}+\frac{1}{M_2}\right)^{1/2} \quad (4)$$

where T is temperature in Kelvin, P is total pressure of the gas mixture in atmospheres, σ_{12} is the average collision diameter in meters given by $\sigma_{12} = 0.5(\sigma_1 + \sigma_2)$, Ω is the dimensionless temperature-dependent collision integral, and M_1 and M_2 are the molecular weights of the two species in the gas mixture in g/mol. This equation shows that the molecular diffusivity in binary gas mixtures is independent of concentration, but varies inversely with pressure, meaning that this diffusion coefficient is expected to be small for the high pressure system of this work.

2.2.2 Internal (Mesopore and Macropore) Transport through Fiber Pores

In highly porous solid adsorbents like zeolites, most of the adsorption sites are contained within the pore network, so mass transport within these enclosed spaces generally controls the adsorption rate. At the fiber surface and within the pores of the sorbent, there is generally negligible bulk flow, such that transport can be considered to happen only through diffusion. Additionally, there is generally only diffusion through the pores of the sorbent, and no transport through the solid sorbent itself. Fick's First Law can again be written in one dimension to describe transport within the particle in terms of the effective diffusivity D_p^{eff} through the pores (such that the flux happens only through the area of the pores and not through the solid):[82, 85]

$$N_A = -D_p^{eff}\frac{\partial C}{\partial x} \quad (5)$$

The void space within a sorbent fiber or pellet can be considered as a randomly oriented interwoven network of pores through which diffusion takes place. This pore diffusivity can be defined as:[82, 85]

$$D_p^{eff} = \frac{D\varepsilon_p}{\tau} \tag{6}$$

where D_p is the pore diffusivity, D is the diffusivity that would exist in a straight cylindrical pore at the same conditions, ε_p is the overall porosity in the solid sorbent (ratio of void volume to total volume of a fiber or pellet), and τ is the tortuosity factor that accounts for random pore orientation and any variations in pore diameter. The tortuosity factor normally ranges between 2 to 6, and is commonly inversely proportional to porosity. The diffusivity D that would be used in equation (6) depends on the mechanism of transport within the meso / macropores. These different contributing mechanisms are described below in more detail.

Molecular Diffusion

Molecular diffusion inside of a fiber sorbent can occur within the large pores of the fiber, but unlike molecular diffusion in the external boundary layer, it will be subject to the effects of tortuosity and porosity and will therefore be effectively smaller. For molecular diffusion to take place internally, the mean free path of a gas molecule must be smaller than the pore diameter of the adsorbent.[85] Otherwise, Knudsen or transition diffusion will occur.

Knudsen Diffusion

Knudsen diffusion occurs when collisions between the diffusing molecules and the pore walls of the sorbent dominates the mass transport. This results when the mean free path of the gases exceeds the pore diameter and molecules become more likely to collide with the pore walls than with other molecules. From kinetic theory and the ideal gas law, the mean free path, λ, of a molecule may be calculated as:[86-87]

$$\lambda = \frac{k_B T}{\sqrt{2}\pi d_A^2 P} \tag{7}$$

where k_B is Boltzmann's constant in J/K, T is temperature in Kelvins, P is pressure in Pascals, d_A is the diameter of the gas molecule of interest in meters.

Typically, Knudsen diffusion is important with small sorbent pores and at low pressures. For the current system sorbing a large gas molecule at high pressure, this type of diffusion is unlikely to be important, but is still mentioned here for completeness. Knudsen diffusivity can be estimated with the following equation:[82, 85]

$$D_K = 9700 r_p \sqrt{\frac{T}{M}} \tag{8}$$

where r_p is the mean sorbent pore radius in centimeters, T is temperature in Kelvin, and M is the molecular weight of the species of interest.

Transition Region Diffusion

When molecular diffusivity and Knudsen diffusivity are equally important, both must be accounted for to accurately describe mass transport within the sorbent macropores. In the case of a binary gas mixture with equimolar counter diffusion, the diffusivity in the transition region may be approximated as:[82, 87]

$$\frac{1}{D_{transition}} = \frac{1}{D_M} + \frac{1}{D_K} \tag{9}$$

Because the mean free path of any molecule depends on pressure, any adsorbent-adsorbate pair can experience a transition from molecular to Knudsen diffusion. Table 2 summarizes the mean free path conditions relative to the pore radius in which the three main types of diffusion will dominate.[81, 88]

Table 2: Range of conditions under which different types of diffusion are important

Diffusion Region	Condition for Diffusion Type
Molecular	$\lambda < 0.1\ r_p$
Transition	$10\ r_p > \lambda > 0.1\ r_p$
Knudsen	$\lambda > 10\ r_p$

2.2.3 Internal (Micropore) Transport through Sorbent Pores

A second region of internal transport exists within the micropores of the powder sorbent supported within the polymer fiber network. The kinetic selectivity of sorbents

such as the zeolites studied in this work is dependent on the micropore diffusion that occurs in the intracrystalline pores. Zeolites are crystalline, highly porous aluminosilicate materials with frameworks made out of SiO_4 and AlO_4 tetrahedra. The 3D pore system has precisely defined diameters due to its crystal structure. The silicon to aluminum ratio in zeolites, which is always 1 or greater, determines the affinity for polar molecules such as water; lower Si/Al ratios result in more hydrophilic materials while higher ratios result in more hydrophobic materials. Exchangeable cations on negatively charged sites contribute to different adsorptive properties.

The crystalline structure of these zeolite and metal organic frameworks and the cations within them are critical to the diffusivity of guest molecules. The framework determines the free diameter(s) of the pores in the crystalline structure of the zeolite, which in turn restricts the size of molecules that are able to pass through. However, the effective diameters are usually larger than the free diameters due to vibrations in both the framework and the diffusing molecule. This allows molecules with critical diameters slightly larger than the free diameter of the crystal framework to diffuse in. Cations on the surface of the framework block the pores and reduce their diameters, further reducing the diffusivity of guest molecules. Varying the type and number of exchangeable cations on these surface sites can change this diffusivity.

Zeolites Y has an effective diameter of 8.5 Å. The presence of sodium cations on zeolite Y (NaY) decreases its effective diameter. Zeolite NaY has a Si/Al ratio close to 2 and its effective diameter of is about 8.3 Å. This diameter is large enough to allow the easy passage of large molecules such as t-butyl mercaptan (TBM), which has a critical diameter of 5.6 Å. As there is no significant barrier for the entrance of TBM molecules

through the pores, diffusion is very fast. Similarly, MOFs have much larger pore diameters than zeolites, typically, and should also fast diffusion through its pores. This internal mass transfer resistance through the sieves is not considered to the rate limited diffusion step. Figure 15 shows the structure of zeolites Y, which are used in this work.

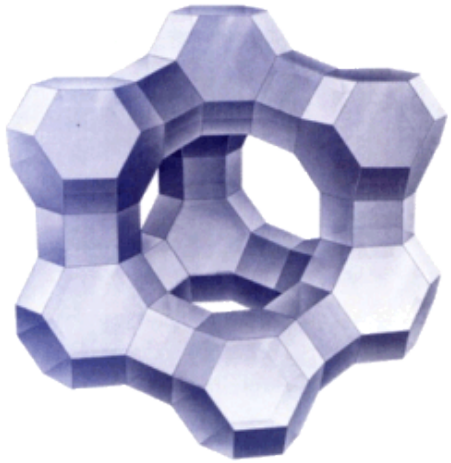

Figure 15: Framework structure of zeolite X and Y (faujasite) unit where each vertex represents a Si or Al atom and each line represents an O atom. The free diameter of the window is about 7.4 angstroms, but due to vibrations within the zeolite crystal structure and the diffusing guest molecule, the effective diameter is slightly larger at 8.5 angstroms. Cations on the surface will reduce this diameter. Source: International Zeolite Association

With the Si/Al ratio of zeolite Y being close to 2, polar molecules such as TBM will preferentially adsorb over nonpolar methane in pipeline natural gas. However, the presence of molecules with larger dipole moments such as water in the natural gas may present a problem, as zeolite Y will preferentially adsorb these species over weakly polar TBM.

2.3 Mass Transfer Influences on Sorption Kinetics

The physical adsorption and desorption rates at the surface of porous adsorbents are usually very high in comparison to the mass transfer resistance and other non-idealities such as channeling and axial dispersion. As such, the adsorption process is considered to be diffusion-limited or diffusion-controlled rather than reaction (sorption)-limited. There are three regions for gas transport associated with fiber sorbents, and thus, it follows that there are also three mass transfer resistances associated with each of the regions. Externally, in binary gas mixtures, mass transfer resistance exists in the boundary layer circumscribing the fiber. Internally, diffusional mass transfer resistance exists in the micropores of the sorbent crystals and in the macropores of the fiber. The sorption rate of the system can be affected by any combination of these resistances with other non-idealities, and the overall dynamics of the fiber sorbent module controls the effectiveness of the sorption process.[85] This section briefly discusses the overall system response to these resistances and how they are compounded, followed by an elaboration of the resistances in each region and how the equilibration times are affected.

2.3.1 Breakthrough Curves

In an ideal plug flow situation, the concentration signal at the outlet of the bed would be identical to the input with only a time delay difference due to the time it takes to reach adsorption equilibrium in the bed. In real systems however, the outlet concentration signal will be dispersed due to the effects of mass transfer resistances

and/or axial dispersion. Studies of adsorption beds can be carried out using a step change to the concentration of the adsorbing species at the inlet and measuring the response at the outlet, called a breakthrough curve. Another common option is to inject a pulse of the adsorbing species at the inlet and measure the response at the outlet, called a chromatographic response.[85] An example of both an ideal (perfect) and real breakthrough curve in response to an inlet step change is shown in Figure 16.

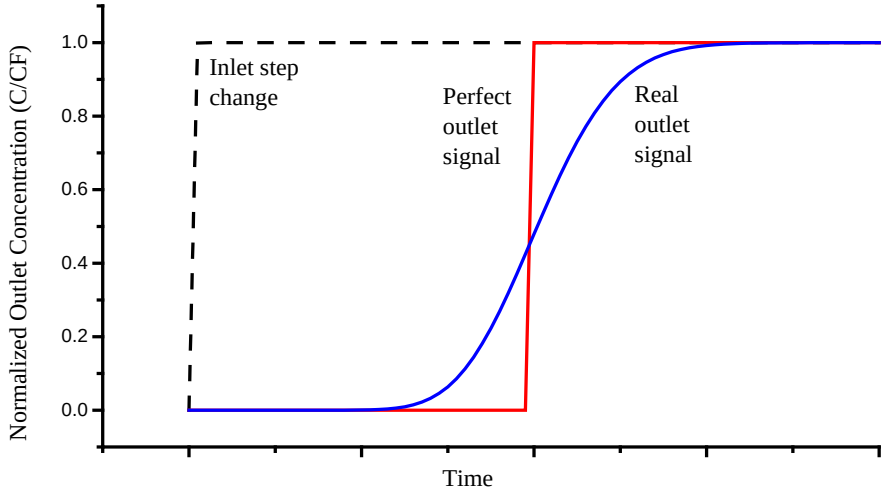

Figure 16: Representative breakthrough curve in response to a step change in inlet concentration of the adsorbing species. The y-axis plots the normalized concentration – the concentration measured at the inlet and outlet divided by the concentration in the feed gas. The perfect outlet signal shows only the time delay due to adsorption in the bed until saturation. The real outlet signal shows both the time delay and spreading due to mass transfer resistances and non-idealities in the bed.

The spread of the outlet response to a perfect step or pulse injection at the inlet is directly related to the resistances and any axial dispersion. In a breakthrough curve, the adsorbate concentration at the outlet is zero until the breakthrough time. The time delay in both cases is due to adsorption; the adsorbing species only shows up in the effluent once the bed has been saturated.[89]

2.3.2 Resistance in Series

The overall outlet response can be said to be affected by the overall mass transfer coefficient encompassing external and internal resistances, and by axial dispersion, if it exists. The resistances and non-idealities add up in series to create an overall response. This can be represented by the following relationship in which all resistances and dispersion are considered to be important:[85]

$$\frac{1}{Kk'} = \frac{D_L}{v_s^2}\left(\frac{1-\varepsilon_b}{\varepsilon_b}\right) + \frac{R_f}{3k_c} + \frac{R_f^2}{15\varepsilon_f D_p} + \frac{r_s^2}{15KD_s} \tag{10}$$

where k' is an overall effective rate coefficient that relates diffusion, dispersion, and mass transfer coefficients (s), K is the dimensionless Henry's law constant (or adsorption equilibrium constant) for linear adsorption isotherm (q=Kc), v_s is the superficial velocity of the fluid in the bed (cm/s), D_L is the axial dispersion coefficient (cm^2/s), ε_b is the bed porosity, R_f is the radius of the fiber (cm), k_c is the external mass transfer coefficient (cm/s), ε_f is the fiber porosity, D_p is the diffusion coefficient through the fiber pores (cm^2/s), r_s is the radius of the zeolite crystals (cm), and D_s is the diffusion coefficient through the micropores of the zeolite crystal (cm^2/s). The first term on the right-hand side of the equation represents the axial dispersion contribution to the overall effective rate, the second term represents the external film resistance contribution, the third term represents the internal macropore (fiber) resistance contribution, and the last term represents the internal micropore (zeolite) resistance contribution. If no axial dispersion is assumed, equation (10) can be simplified to:[85]

$$\frac{1}{Kk} = \frac{R_f}{3k_c} + \frac{{R_f}^2}{15\varepsilon_f D_p} + \frac{{r_s}^2}{15KD_s} \tag{11}$$

where k is the overall mass transfer coefficient and all other terms remain the same.

The time, t, it takes to reach mass transfer equilibrium in any of the regions can be estimated from:[88]

$$t \approx c\frac{L^2}{D} \tag{12}$$

where L is the characteristic length (cm) and D is the diffusion coefficient (cm^2/s) associated with that region, and c is a dimensionless constant that varies with each region.

2.3.3 External Resistance and Mass Transfer Coefficient

External mass transfer resistance can occur in binary component systems as a stagnant boundary layer or film layer forms around the outer surface of the fiber sorbent. The velocity of the gas flowing parallel to the fibers will change depending on its position relative to the fiber outer surface, decreasing with proximity to the fiber radius. This is due to the no-slip constraint at the fiber surface. The boundary layer is defined as the distance from the fiber where the concentration of the adsorbing species is 99% of the concentration in the bulk or feed gas.[90] The external resistance occurs as a result of the adsorbing species in the feed gas having to diffuse through this film layer to reach the fiber.

It is difficult to determine the thickness of the boundary layer, so a mass transfer coefficient is typically used instead to describe the flux of the species from the bulk gas to the sorbent surface:[82, 91]

$$N_A = k_c(C_{A\delta} - C_{AS}) \tag{13}$$

where N_A is the average molar flux in the x-direction (moles/cm^2-s), and k_c is the external mass transfer coefficient (cm/s). This external mass transfer coefficient can be estimated from appropriate Sherwood correlations relating the properties and velocity of the flowing fluid to the dimensions of the sorbent. The Sherwood number is defined as:[92]

$$Sh = \frac{k_c d_f}{D_M} \tag{14}$$

where d_f is the fiber diameter and D_M is the molecular diffusivity. For flow outside and parallel to a bundle of fibers, the Sherwood number can be correlated as:[93]

$$Sh = 1.45\left[ReSc\frac{d_f}{L_b} \right]^{0.33} \tag{15}$$

where L_b is the length of the fiber bed and the fibers, Re is the Reynolds number used to characterize different flow regimes, and Sc is the Schmidt number used to characterize the importance of viscosity versus diffusivity in fluid flows, defined as:[91]

$$Re = \frac{\rho d_f v_s \varepsilon_b}{\mu} \tag{16}$$

$$Sc = \frac{\mu}{\rho D_M} \tag{17}$$

where μ and ρ are the viscosity and density of the moving fluid respectively, v_s is the fluid superficial velocity, and ε_b is the porosity of the fiber bed. As can be seen from equations (14) to (17) the external mass transfer coefficient is a function of fluid velocity and other fiber and module properties.

2.4 Adsorption Properties and Patterns in Fiber Sorbents

As mentioned previously, the intrinsic properties of the feed gas, fiber materials, and fiber morphology directly control the mass transfer of adsorbate from the bulk feed gas to the adsorption sites within the sorbent. The shape and timing of the breakthrough curve as it is influenced by mass transfer resistances and dispersion, is then closely related to how efficiently the bed and the sorbent itself is utilized, and the types of patterns that will be observed within the bed. These patterns can be characterized a number of ways so as to describe bed performance, and will be discussed further in this section.

2.4.1 Mass Transfer Zone and Length of Unused Bed

The spreading of the breakthrough curve response at the outlet of the bed can be correlated to one side of the concentration front moving faster than the other inside the bed, as shown in Figure 17. The breakthrough concentration in an adsorption bed is a user chosen point at which the concentration of the adsorbing species in the outlet reaches

a maximum allowable level. The time it takes to reach this point is called the breakthrough time, t_b. The stoichiometric time point, t_s, represents the time at which the ideal concentration front (no spreading) would reach the end of the bed such that the breakthrough curve response would be identical to the inlet step function. This ideal concentration front can be applied to the previous stages of the bed before breakthrough as well, in the middle of the actual concentration front, such that the bed area in the side that moves faster is equal to the bed area in the side that moves slower. The equilibration time, t_e, is the time at which the adsorbent reaches its saturation capacity and the adsorbate concentration in the effluent becomes the same as that in the feed.

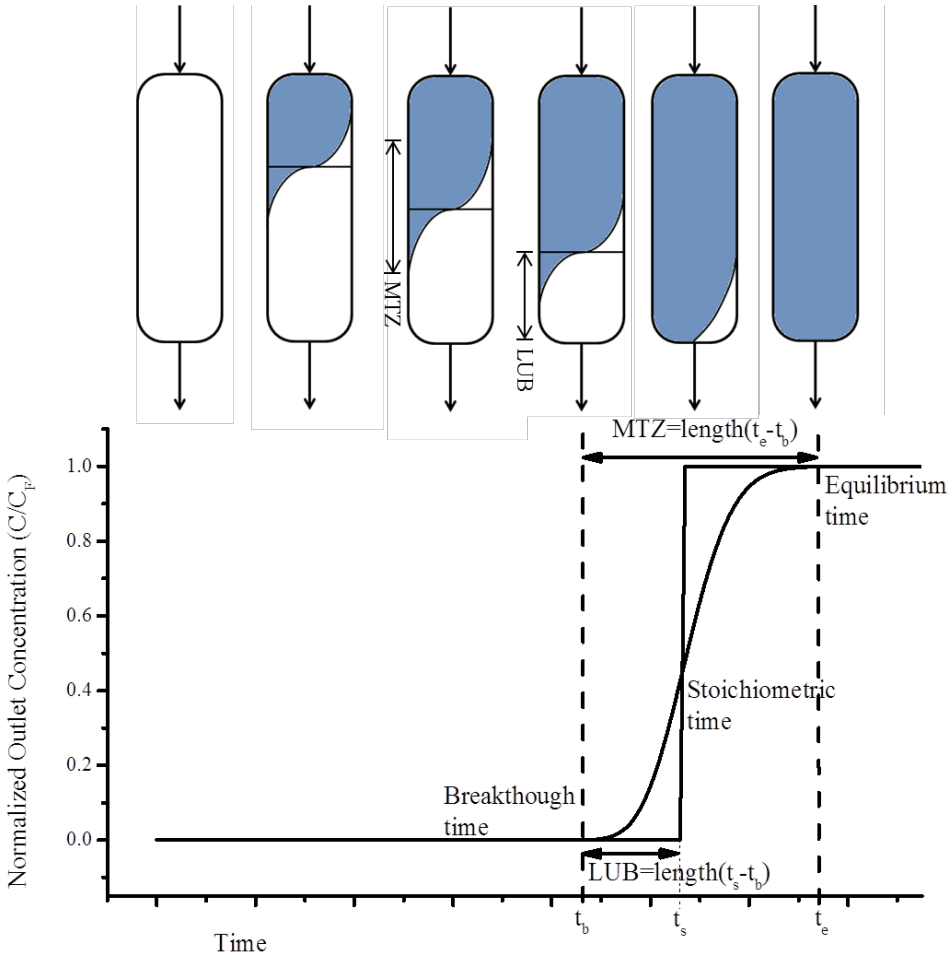

Figure 17: Adsorption over time of the species of interest in a bed and its corresponding breakthrough curve showing breakthough time tb, stoichiometric time ts, and equilibrium time te. Figure adapted from Seader and Henley, 1998.[94]

The length equilibrium section (LES) is the ideal required bed length if there was no spreading of the concentration front. The LES is then the length in the adsorption bed between the ideal concentration front and the inlet of the bed at breakthrough time. However, due to spreading, if the LES were employed as the actual bed length to be used, the bed would not achieve the same capacity as in the ideal case. The length of unused bed (LUB) is then the additional length needed in the bed to reach that same capacity.

In Figure 17, the LUB is the length in the adsorption bed between the ideal concentration front and the beginning of the actual concentration front at the breakthrough time.[94-95] The LUB can be calculated with the following equation:[96]

$$LUB = \left(1 - \frac{t_b}{t_s}\right) L_b \tag{18}$$

where t_b is the breakthrough time, t_s is the stoichiometric time, and L_b is the actual length of the bed. The side of the bed where the feed gas enters will adsorb the species first and become saturated with the adsorbate, therefore coming to equilibrium with the feed gas. The side of the bed where the product gas exits will contain only the residual adsorbate that did not desorb during the regeneration phase until the concentration front reaches it. The section of the bed where the amount adsorbed varies from the equilibrium concentration to the residual concentration (the moving concentration front) is called the mass transfer zone (MTZ), as shown in Figure 17. This transition zone is where the adsorption is actively taking place, and moves forward through the bed until breakthrough occurs.[97] The length of the MTZ is directly related to the overall mass transfer resistances and dispersion and to the shape / spreading of the breakthrough curve.

CHAPTER 3

MATERIALS AND EXPERIMENTAL METHODS

Appropriate materials selection and characterization are important for spinning fiber sorbents. A polymer is selected for the creation of the porous fiber body, and zeolite and metal organic framework (MOF) sorbent materials with high sulfur capacity, selectivity, and cyclic regenerability and stability are contained within the pores of the fiber. Both the original crystalline sorbent materials and the fiber sorbents created were characterized for adsorption performance and to identify any changes that occur after exposure to TBM gas.

3.1 Preparation of Materials

3.1.1 Adsorbents – zeolites and metal organic frameworks

The metal organic frameworks (MOFs) Cu-BTC,[98] MIL-53(Al),[99] and UiO-66(Zr)[100] were synthesized and activated[101] according to the previously published literature. All MOF synthesis chemicals were purchased from Sigma-Aldrich. Briefly, for Cu-BTC, 0.91 g of copper(II) nitrate, trihydrate was mixed and sonicated with 12 mL DI water in one container. In a second container, 0.42 g trimesic acid was mixed and sonicated with 12 mL ethanol. These two solutions were then mixed together in a 40 mL Parr bomb and reacted at 100°C for 18 hours. After cooling, the product was filtered and washed with DI water followed by ethanol, then dried and activated in air at 150°C

overnight. For MIL-53(Al), 2.60 g aluminum nitrate nonanhydrate, 1.15 g terephthalic acid, and 20 mL DI water were mixed together in a 40 mL Parr bomb and reacted at 220°C for 3 days. After cooling, the product was filtered and washed with DI water and the resulting powder was placed back into the Parr bomb with 20 mL dimethylformamide (DMF) and reacted at 150°C for 12 hours. Again after cooling, the product was filtered and washed with DMF followed by methanol, then dried and activated under vacuum at 200°C. For UiO-66(Zr), 0.636 g zirconium(IV) chloride, 0.453 g terephthalic acid, and 106 mL DMF were mixed together in a beaker until all solids were dissolved, then split equally into ten 20-mL scintillation vials. The vials were placed in a sand bath in an oven and reacted at 120°C for 22 hours. After cooling, the product was filtered and washed with DMF, then dried and activated under vacuum at 200°C.

These MOFs were chosen based on several critically necessary and desirable criteria for this application. These criteria include stability in the open atmosphere over time, a history of use in the published literature for the adsorption of acid gases (such as CO_2, H_2S, and toxic gases) in general and the desulfurization of fuels (such as removing thiophenes from liquid model fuels such as octane, dodecane, etc.) specifically, stability to liquid water, and current and future commercial availability. These factors are necessary for the practical and economical application of fiber modules for odorant removal from natural gas.

An additional MOF, ZIF-8, was purchased directly from Sigma-Aldrich (Basolite Z1200). Zeolites NaY (CBV100, with a SiO_2/Al_2O_3 mole ratio of 5.1), Beta (CP814E, with a SiO_2/Al_2O_3 mole ratio of 25), and ZSM-5 (CBV28014, with a SiO_2/Al_2O_3 mole ratio of 280) were purchased separately from Zeolyst International as a basis for

comparison with the MOFs. These zeolites were chosen based on similar criteria to the MOFs. These zeolites are all commercially available and economical in bulk and have been well studied and characterized over the years for various applications. In contrast, MOFs are still relatively new materials and many are very expensive and even difficult to purchase in bulk, or not commercially available at all. However it is reasonable to assume that as more research is done with MOFs over time, they will eventually become economically available as zeolites are currently. It is also possible that because MOFs have such higher capacities and selectivities for certain adsorbates, that they could become more relevant to these types of applications than zeolites in the future, providing justification for their use and discussion in this current study.

The most promising adsorbents identified from the initial screening studies were used in preliminary fiber-synthesis experiments using a syringe which will be discussed in more detail in the following sections. Additionally, a different proprietary procedure was used to separately synthesize large batches of UiO-66(Zr) for further studies using the spinneret fiber-spinning system, which will also be discussed later.[102] Figure 18 shows the framework structures of the most promising sorbents.

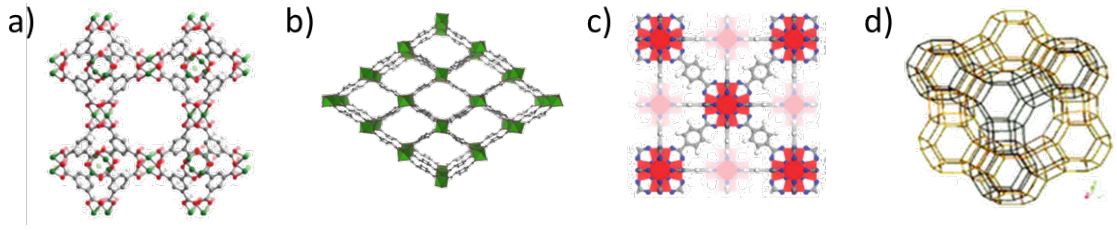

Figure 18: Framework structures of a) Cu-BTC, b) MIL-53(Al), c) UiO-66(Zr), and faujasite zeolite NaY. Source: J. Hazard. Mater. 244, 2013.

3.1.2 Fiber polymer and solvents

Polymer fibers incorporating these sorbent materials were mixed with cellulose acetate (CA) (MW ≈ 50 000) polymer as the fiber body, poly(vinylpyrrolidone) (PVP) (MW ≈ 55 000) as the pore former, N-methyl-2-pyrrolidone (NMP) as the spinning solvent, and deionized (DI) water as the non-solvent to form the spin dope.[103] Cellulose acetate was chosen to form the fiber body due to its commercial availability, low-cost, high glass transition temperature, and its well known properties due to the abundance of research conducted on it over the years. Figure 19 shows the structure of the repeat units of cellulose acetate.

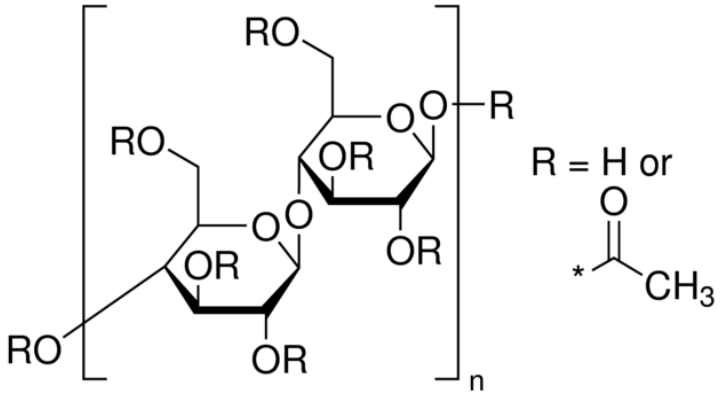

Figure 19: Repeat unit of cellulose acetate. Source: Sigma-Aldrich.

PVP was chosen was the pore former due to its ability to suppress macrovoids during non-solvent quench of the nascent fiber, and its successful use in past literature for creating fibers of similar composition to the ones used in the current study. NMP was chosen as the solvent in the fiber sorbent dope solution due to its miscibility with water and solvency for cellulose acetate, as well as relative low toxicity compared to other potential solvents.

Additionally, methanol and hexane were used for solvent exchange in the fibers after their formation to maintain the pore structure during drying.[79] The water remaining in the fibers after spinning is first exchanged with methanol, followed by exchanging the methanol with hexane. This solvent exchange process prevents capillary forces from collapsing the porous structure of the fiber by replacing high surface tension fluids with lower surface tension fluids. All fiber spinning chemicals and materials were purchased from Sigma-Aldrich, and solvents and nonsolvents were used as received without further modification.

3.1.3 Fiber sorbent spin dope preparation and spinning

Fiber sorbent spin dopes were created in the desired compositions according to a general procedure. The CA and PVP polymers were first dried in a vacuum oven at 110 °C for 24 hours, and the adsorbent material (MOF or zeolite) was dried at 200 °C for 24 hours to remove residual solvents or species adsorbed from the atmosphere. To form the spin dope, NMP was first mixed with DI water, followed by adding the sorbent and sonicating periodically with a 1000 W horn for 5 min to ensure adequate crystal dispersion in the dope. PVP and CA polymers were then slowly added and stirred with a high-speed impeller for 24 hours, followed by additional mixing on a roller for 24 hours to ensure complete polymer dissolution and dope homogeneity.

Spin dopes were first created in small quantities with varying amounts of sorbent, polymer, solvent, and nonsolvent to determine the binodal curve separating the one- and two-phase regions in the ternary diagram of this system.[104] Preliminary fiber-formation tests were carried out by loading these varying dopes into 10 mL syringes and extruding

into a water bath at room temperature to simulate fiber spinning, as shown in Figure 20 (left). Syringe fibers were synthesized as an initial test to visually observe spinnability and phase separation kinetics, as well as to test fiber sorbent properties and ensure consistency between the fiber dope mixture and the finally produced dry fiber. After these factors were ensured, larger amounts of dope in the chosen compositions were created for use in the spinneret fiber-spinning system.

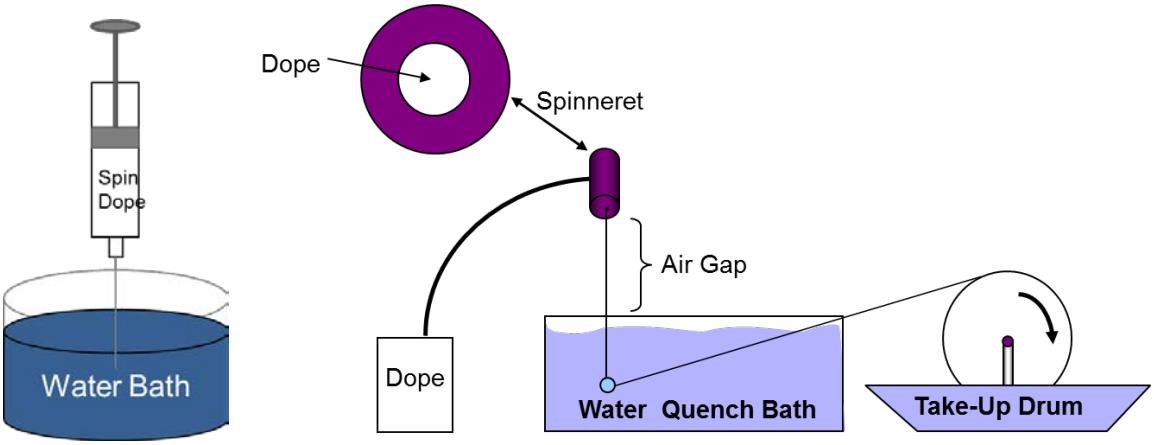

Figure 20: Syringe fiber synthesis setup (left) versus spinneret fiber synthesis setup (right).

Fibers were then created on a larger scale using a dry-jet, wet-quench technique using the spinning apparatus shown in Figure 20 (right) to incorporate sorbents into a polymer matrix with desired gas-separation properties.[105] The spin dope created with the desired composition was first loaded into a syringe pump and degassed for 24 hours under vacuum. The dope was then pumped and extruded through a spinneret into a hot water quench bath where it phase separates and PVP leaves to form the porous structure. The newly formed fiber was then taken up on a rotating drum with a secondary cold water bath to extract residual solvent. The effect of different spin states on the diameter

of the final fibers was investigated by varying the dope flow rate between 100-700 mL/hr and the drum uptake rate between 10-15 m/min. The air gap between the spinneret and the hot water quench bath was adjusted between 2-4 cm to optimize fiber formation. The spun fibers were then removed from the drum after 20 minutes and solvent exchanged in a water bath three times for over 3 days, thereby exchanging the NMP in the fibers with water.

The excess water in the fibers was then further solvent exchanged, by soaking first in methanol 3 times for 30 minutes each and then in hexane once for 30 minutes to prevent capillary forces from collapsing the fiber pore structure. The fibers were then dried in air for 3 hours followed by drying under vacuum at 80 °C for 3 hours.

As a first pass on these fibers, syringe spinning was used, and an easily achievable target weight loading of 50 wt % was selected for all sorbents. Once preliminary characterization results were obtained for these first syringe fibers, 50 wt % NaY was spun with the spinneret system to verify that syringe and spinneret fibers had similar properties. Once the agreement was demonstrated, NaY/CA and UiO-66(Zr)/CA spinneret fibers were created at the higher target sorbent loading of 75 wt %. These higher sorbent weight loaded fibers exhibit a satisfactory balance between the fiber spinnability and strength obtained with low sorbent loading and the high sulfur capacities per gram of fiber obtained with high sorbent loading.

3.1.4 Fiber module creation

To create fiber modules for temperature swing adsorption (TSA) system testing, polymer-sorbent hybrid fibers were bundled together at various void fractions in a ¼ inch

diameter, 8 inch length stainless steel Swagelok tubing with 90 degree elbow unions at the ends as shown in Figure 21. Model natural gas flows into the inlet of the module, TBM is adsorbed inside the fibers, and TBM-free natural gas exits the outlet of the module once connected to the TSA system described in later sections.

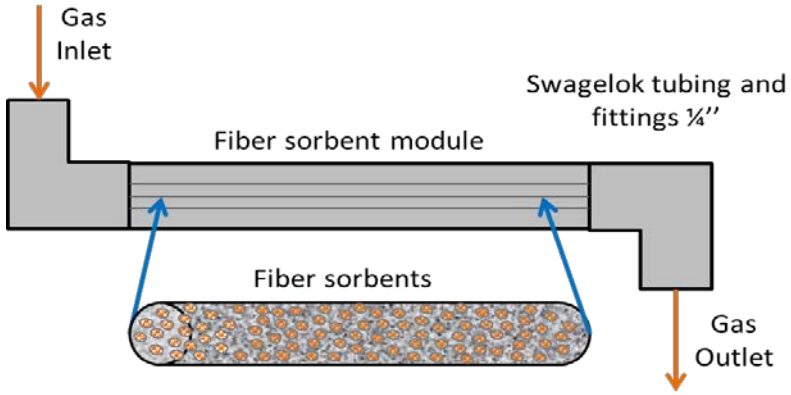

Figure 21: Schematic of a fiber sorbent module.

3.2 Characterization of Materials

Several characterization experiments were carried out on both the original powder sorbents and the fiber sorbents to understand how the spinning process and incorporation into the fiber affects the sorbents. These tests were also performed on both fresh materials and "used" materials after exposure to many cycles of TBM adsorption and desorption to determine the cyclic effects of TBM sorption and heating on the properties of the materials.

3.2.1 X-Ray diffraction

Powder X-ray diffraction (XRD) using a PANalytical X'Pert Pro diffractometer was used to collect XRD patterns on both the original sorbent crystals and the resulting fiber sorbents. The XRD patterns were used to characterize the crystal structures of the original sorbents and to confirm proper synthesis of the MOFs by comparing the patterns obtained to those in the published literature. Powder sorbent samples were pressed as flat as possible into the sample holder with a glass slide before clipping the sample holder into the instrument for measurement. For the fiber sorbents, XRD patterns were used to verify successful sorbent incorporation into the polymer fiber, as well as the retention of sorbent crystallinity within the fiber. Fibers were cut into thin slices with a razor blade and placed vertically (cross-sectional area facing up) in a single layer into the sample holder. The 1D X'Celerator detector was used with an incident beam path radius of 240 nm and take-off angle of 6.000°. The X-ray generator was set to a tension of 45 kV and current of 20 mA, with mask fixed at 10 mm, divergence slit fixed at 1/8'', and anti-scatter slit fixed at ¼''. The same scanning protocol was used for both the crystal sorbent samples and the fiber sorbent samples.

3.2.2 Scanning electron microscopy

Scanning electron microscopy (SEM) using a Hitachi SU8010 cold field emission scanning electron microscope was also used to characterize both powder sieves and fiber sorbents. SEM images taken of the powder sieves were used to determine crystal size range and distribution. SEM images taken of the fibers to were used to verify fiber sorbent morphology (pore structure, interfacing, and sorbent crystal distribution, as well

as any defects or deformations in the fiber itself). For these SEM images, dry fiber sorbents were first submerged in liquid N_2 and then sheared with fine point tweezers to produce sharp fiber breaks. Both fiber and crystal SEM samples were mounted on a SEM mount and sputter-coated with a 10−20 nm thick gold coating before imaging. Fibers were mounted both vertically and horizontally on the SEM mount to capture images of both the cross-sectional area and the outer surface of the fiber.

3.2.3 Elemental analysis and thermogravimetric analysis

Elemental analysis (EA) by ALS Environmental and simultaneous thermogravimetric analysis (TGA) and differential scanning calorimetry (DSC) using a Netzsch STA 449 F3 Jupiter TG-DSC were performed on both powder sorbents and fibers. Elemental analysis of carbon (C), hydrogen (H), nitrogen (N), sulfur (S), and the corresponding metal center (Cu, Al, and Zr for Cu-BTC, MIL-53(Al), and UiO-66(Zr) respectively) was requested for MOF samples while silicon (Si), Aluminum (Al), and sulfur (S) was requested for NaY samples. For TGA experiments, a sample is loaded into the sample holder and heated from 25 ºC to 900 ºC at a ramp rate of 10 ºC / min under an atmosphere of air flowing at 90 mL/min while recording the sample weight. For this analysis, fibers must first be chopped with a razor blade into small enough pieces to fit into the sample holder.

The EA and TGA results on sorbent materials were used to further verify proper synthesis and estimate the amount of water adsorbed by each material. The EA and TGA results on fiber sorbents were also used to calculate the actual sorbent loading in the fiber and compare it with the target weight loading for accuracy. The EA on “used” materials

which have been exposed to heat and TBM was also used to determine if any residual sulfur remains in the material even after desorption.

3.2.4 Nitrogen physisorption

Nitrogen adsorption measurements at 77 K using a Micromeritics ASAP 2020 physisorption analyzer were taken on both powder and fiber sorbents to determine sorbent characteristics and identify any changes in surface area and pore volume that happened with the spinning process.

3.2.5 Other supporting characterization experiments

X-ray photoelectron spectroscopy (XPS) was done using a Thermo K-Alpha spectrometer with a monochromatic A1 Kα X-ray source, and ultraviolet−visible spectroscopy (UV−vis) was done using a Cary 5000 UV−vis−NIR spectrophotometer. Raman spectroscopy was done using a WiTec Alpha 300R confocal Raman microscope with Ar^+ ion laser of wavelengths 514 and 785 nm and were performed on powder sorbent samples only to further describe the changes that occur after many cycles of TBM adsorption and desorption.

3.3 Adsorption Measurements

Adsorption measurements were performed on both the original powder sorbents and the hybrid fiber sorbents using three different feed streams of various compositions. The first composition was a model natural gas feed containing 60 ppm of TBM in a

balance of methane (Nexair, 99.0% purity methane). This model gas odorant concentration and pressure produced a somewhat lower odorant partial pressure than typically present in pipeline natural gas (about 17 atm pressure and ≤10 ppm odorant) but provided a convenient range for testing in this study by shortening the time to reach equilibrium adsorption. The second feed stream was 60 ppm of TBM in a balance of helium (Nexair, ultrahigh purity), and the third was the model natural gas feed without TBM (Nexair, 99.0% purity methane). These additional two gases were tested for the purpose of separating the adsorption effect of the trace impurities that may be present in the pipeline natural gas and that were present in the model natural gas used in this study, from the TBM itself.

3.3.1 Thermogravimetric analysis (TGA) adsorption

In an initial screening process, the MOF and zeolite adsorbent materials were tested for their equilibrium adsorption capacity at 35 °C and atmospheric pressure in a thermogravimetric analyzer (TA Instruments Q500 with evolved gas furnace) flowing the model natural gas feed. This setup is shown in Figure 22. Prior to adsorption, all materials were pretreated at 200 °C for 1 hour in flowing helium (Airgas, ultrahigh purity). The feed flow rates were fixed at 90 mL/min with the internal mass flow controller of the instrument and bubble flow meter for the helium pretreatment gas and sulfur-containing gas, respectively. Desorption and adsorption steps were carried out in two separate programs. At the end of the desorption program, the model natural gas was first set at the desired flow rate, then the two 3-way valves switched simultaneously to change the inlet feed flow to the TGA from the helium desorption gas to the model

natural gas to be adsorbed. After flowing over the sample, the outlet gas passed through a scrubber before venting to the fume hood in which the entire setup was located.

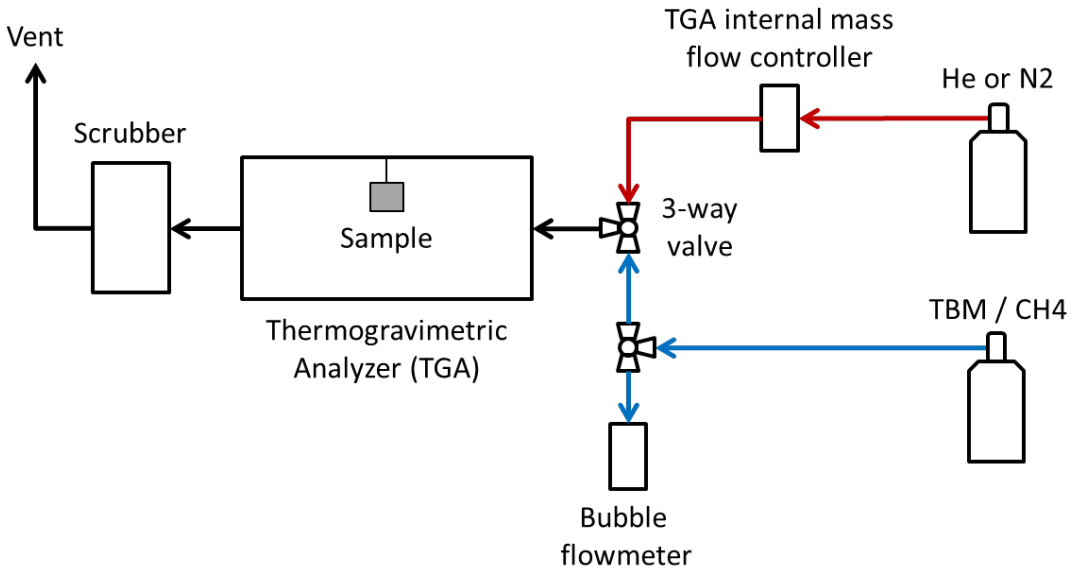

Figure 22: Thermogravimetric analyzer (TGA) for cyclic adsorption experiments on adsorbent sieve materials and fiber sorbents.

After this initial screening, the most promising sorbent materials were further tested for cyclic regenerability by desorbing the adsorbed species at 200 °C for 1 hour in flowing helium (the same conditions as the pretreatment step), followed by switching back to the model natural gas feed for several cycles. The used adsorbents were then characterized with the techniques described in the previous section and compared against those of the fresh materials to identify any structural changes, irreversible adsorption, or reactions that may have occurred as a result of several cycles of TBM exposure. Additionally, these chosen materials were then evaluated for equilibrium adsorption capacity in the same manner for the TBM / He feed and the TBM-free model natural gas

feed. The most promising adsorbent materials from these cyclic studies were further chosen to be spun into fiber sorbents.

The hybrid polymer-sorbent fibers created were also tested for equilibrium adsorption capacity and cyclic stability at 35 °C and atmospheric pressure in the same TGA flowing the same model natural gas feed. Prior to adsorption, fibers had to be chopped with a razor blade into pieces small enough to fit into the TGA sample holder. The fibers were then pretreated at 120, 200, and/or 300 °C for 1 hour in flowing helium (Airgas, ultrahigh purity). Cyclic desorption of the samples was performed using the same temperature, gas, time, and flow conditions as the pretreatment step. The higher temperature 200 °C desorption was performed on MOFs and MOF containing fibers to obtain results that can be more directly compared against traditional adsorption methods in the published literature utilizing 200 °C as the desorption temperature. The 300 °C desorption was performed on the NaY sieves for the same reason; however, to maintain the structural integrity of cellulose acetate, desorption temperatures higher than 200 °C could not be used for NaY/CA hybrid fibers. The 120 °C desorption was performed on all materials to evaluate the effect of a lower-temperature pretreatment method that could potentially provide energy savings.

The feed flow rates of both the desorption and adsorption gases were again fixed at 90 mL/min for the internal mass flow controller of the instrument and bubble flow meter for the helium pretreatment gas and sulfur-containing gas, respectively. Equilibrium was reached within 24 hours of adsorption for all materials. Gas selectivity in the fibers was evaluated using the same procedure as with the sieves with a feed of 60

ppm TBM in a balance of helium (Nexair, ultrahigh purity) and the model natural gas feed without TBM (Nexair, 99.0% purity).

3.3.2 Temperature swing adsorption (TSA) system

After verifying the adsorption capacity and characteristics of fiber sorbents in the TGA system, fiber sorbent module were created and tested in a temperature swing adsorption system shown in Figure 23. The system is fully automated and controlled by a Labview program, and the entire physical setup is located inside of a walk-in fume hood. The flow rates of both desorption and adsorption gases are regulated by mass flow controllers (MFC) while automated pneumatic valves control which gas flows into the system. The fiber sorbent module is wrapped with heating tape to control the temperature of the module, and then connected to the system inside of a process control cabinet with a cabinet heater to control the temperature of the atmosphere surrounding the module. Pressure and temperature of the flowing gas is monitored and recorded continuously at both the inlet and outlet of the module. A small portion of the outlet gas was sampled continuously by a mass spectrometer that continuously analyzed and recorded the molecular composition of the gas. The remainder of the outlet gas flowed through a scrubber before being vented to the hood. The variables tested in this system were: feed flow rate, module packing fraction, and adsorption temperature.

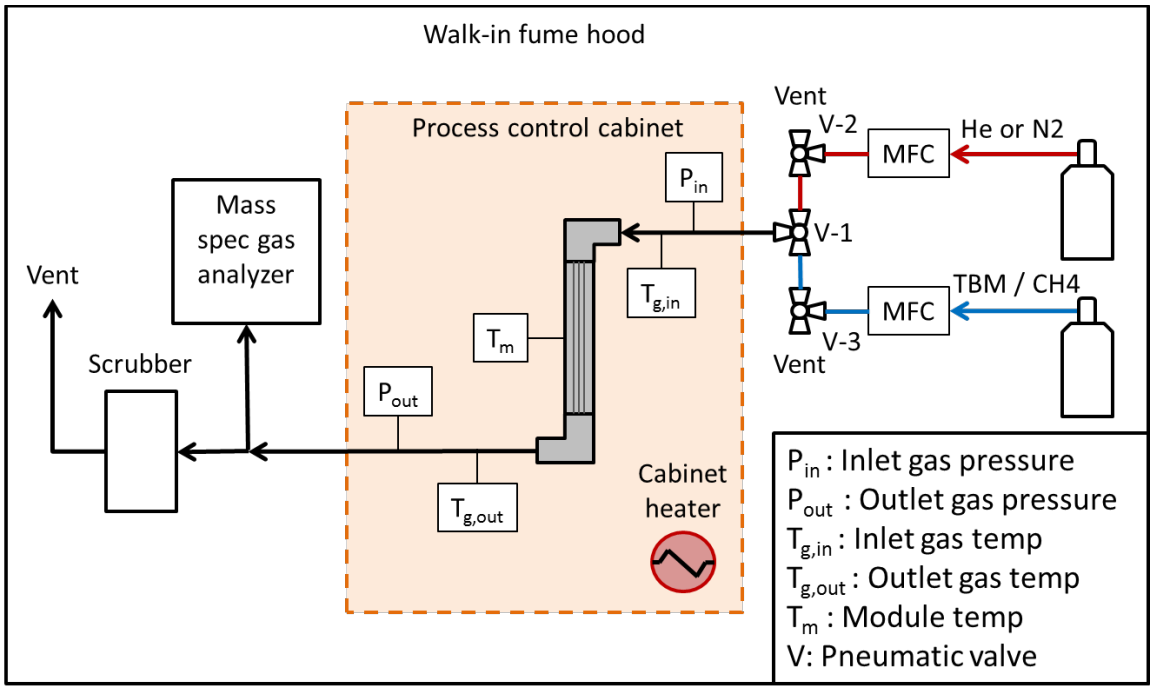

Figure 23: Temperature swing adsorption (TSA) system schematic for cyclic adsorption experiments on fiber sorbent modules.

Similar to the TGA experiments mentioned previously, the fiber sorbent module was first pretreated at 200 °C for 3 hours in a flow of 80 sccm helium (Airgas, ultrahigh purity) at atmospheric pressure to desorb any previously adsorbed gases. This was followed by a 30 minute cooling step in helium flowing at the same rate to cool to module down to 35 °C in preparation for adsorption. The gas feed was then switched to the model natural gas feed flowing at 10, 20, 40, or 80 sccm until equilibrium was reached to evaluate the effect of different feed flow rates on the breakthrough curve and final adsorption capacity. Additionally, the fiber sorbent module packing fraction was tested at 1, 3 and 10 fibers and adsorption temperatures were tested at 35, 45, and 55 °C. Due to the evidence from previous fiber sorbent experiments in the TGA that all of the fibers created are regenerable, each module created at a certain packing fraction was used

multiple times for the variables listed. These used fibers were then characterized after adsorption experiments were finished with the characterization test described in the previous section.

CHAPTER 4

METAL ORGANIC FRAMEWORK SYNTHESIS, CHARACTERIZATION, AND PERFORMANCE RESULTS

The ability of selected MOFs to selectively adsorb t-butyl mercaptan (TBM), a common odorant, from both a mercaptan / inert gas feed and a model natural gas feed was first investigated. As mentioned previously, the long-term goal was focused on eventually incorporating these powder materials into hybrid polymer fiber sorbents for use in a novel gas−solid contacting system. Therefore, the MOFs used in this study were chosen not only based on their potential high TBM uptake capacity and selectively but also other practical factors, such as stability in atmospheric air, stability toward liquid water, cyclic stability and regenerability, and ease of synthesis and / or commercial availability.

First, several different MOFs which have been studied previously for the adsorption of acid gases, especially for the desulfurization of fuel, were screened for their adsorption capacity [Cu-BTC, MIL-53(Al), UiO-66(Zr), and ZIF-8], and were compared to the capacities of several different benchmark zeolites [NaY, Beta, and ZSM-5]. Further characterization and regeneration experiments were then performed with the most promising materials.

4.1 Initial Characterizations of Materials

4.1.1 Nitrogen physisorption isotherms

The Brunauer−Emmett−Teller (BET) surface area and t-plot micropore volume measured from the nitrogen physisorption isotherms at 77 K and particle size range measured from SEM images or taken from manufacture information are summarized in Table 3.

Table 3: Surface areas, pore volumes, and particle size ranges of adsorbent materials used in this study

Sample	BET Surface Area (m^2/g)	t-plot Micropore Volume (cm^3/g)	Particle Size (μm)
Cu-BTC	1504	0.55	3-7
MIL-53(Al)	1329	0.54	1-4
UiO-66(Zr)	1002	0.40	1-4
ZIF-8	1528	0.68	1-5
Zeolite NaY	868	0.35	1-3
Zeolite Beta	530	0.15	1-3
Zeolite ZSM-5	648	0.15	1-3

The nitrogen physisorption isotherms used to calculate the BET surface areas and micropore volumes shown in Table 3 of Cu-BTC, MIL-53(Al), UiO-66(Zr), and NaY before and after exposure to five cycles of TBM adsorption are shown in Figure 24. All fresh materials displayed type I isotherms without hysteresis, which is typical for microporous materials. After exposure, Cu-BTC displayed a type III isotherm, UiO-66(Zr) displayed a type II isotherm, and MIL-53(Al) and NaY both displayed type I

isotherms. Other material characterization results will be discussed in later sections, along with the analysis of the fresh versus used adsorbent samples.

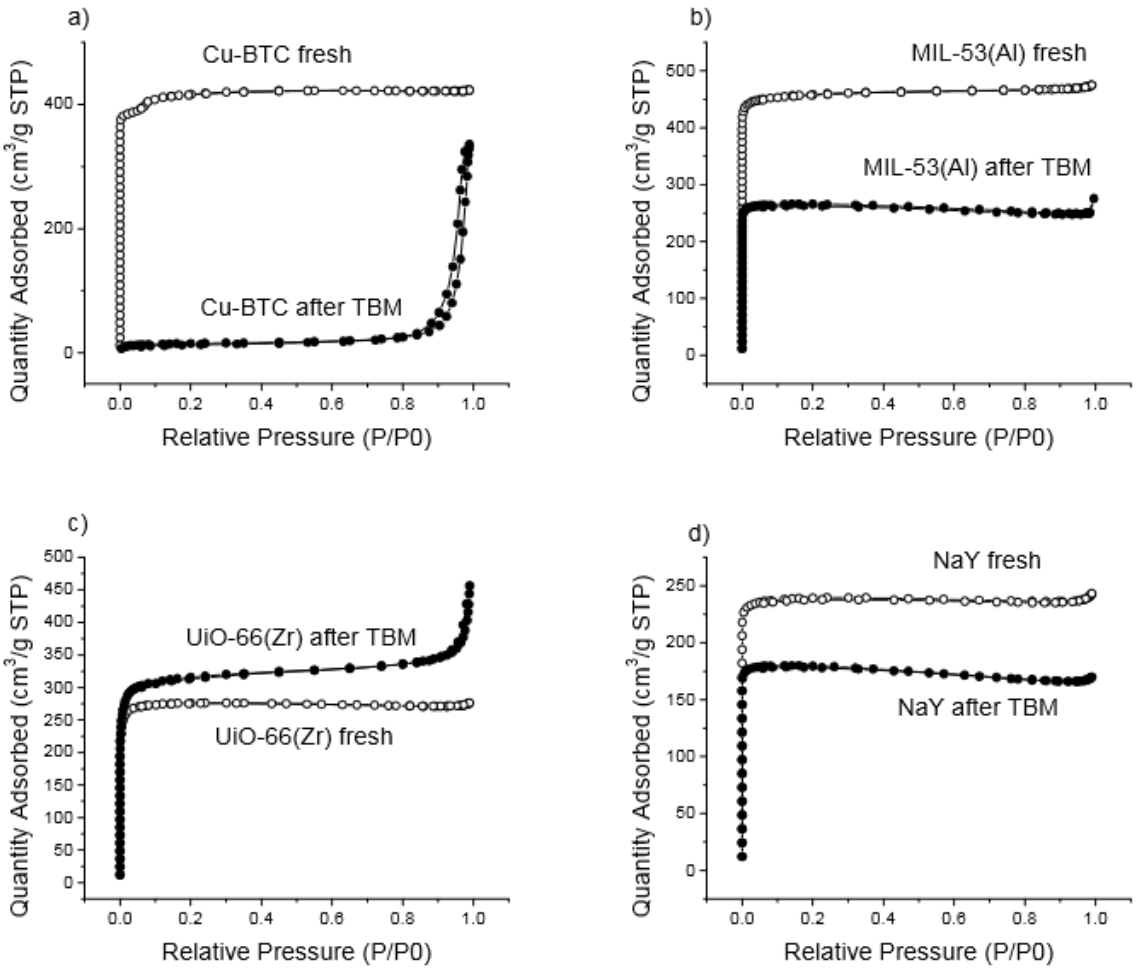

Figure 24: Nitrogen physisorption isotherms of chosen materials before and after five cycles of TBM exposure: (a) Cu-BTC, (b) MIL-53(Al), (c) UiO-66(Zr), and (d) NaY.

4.1.2 Degradation TGA curves

The TGA curves of the chosen materials used to further verify that the correct adsorbent materials were synthesized are shown in Figure 25. The MOF materials all show a slight initial weight decrease from adsorbed water leaving the pores, followed by

a much larger sharp weight decrease from the ligand burning off, leaving behind only the metal oxides. Zeolite NaY only shows the initial weight decrease from leaving water.

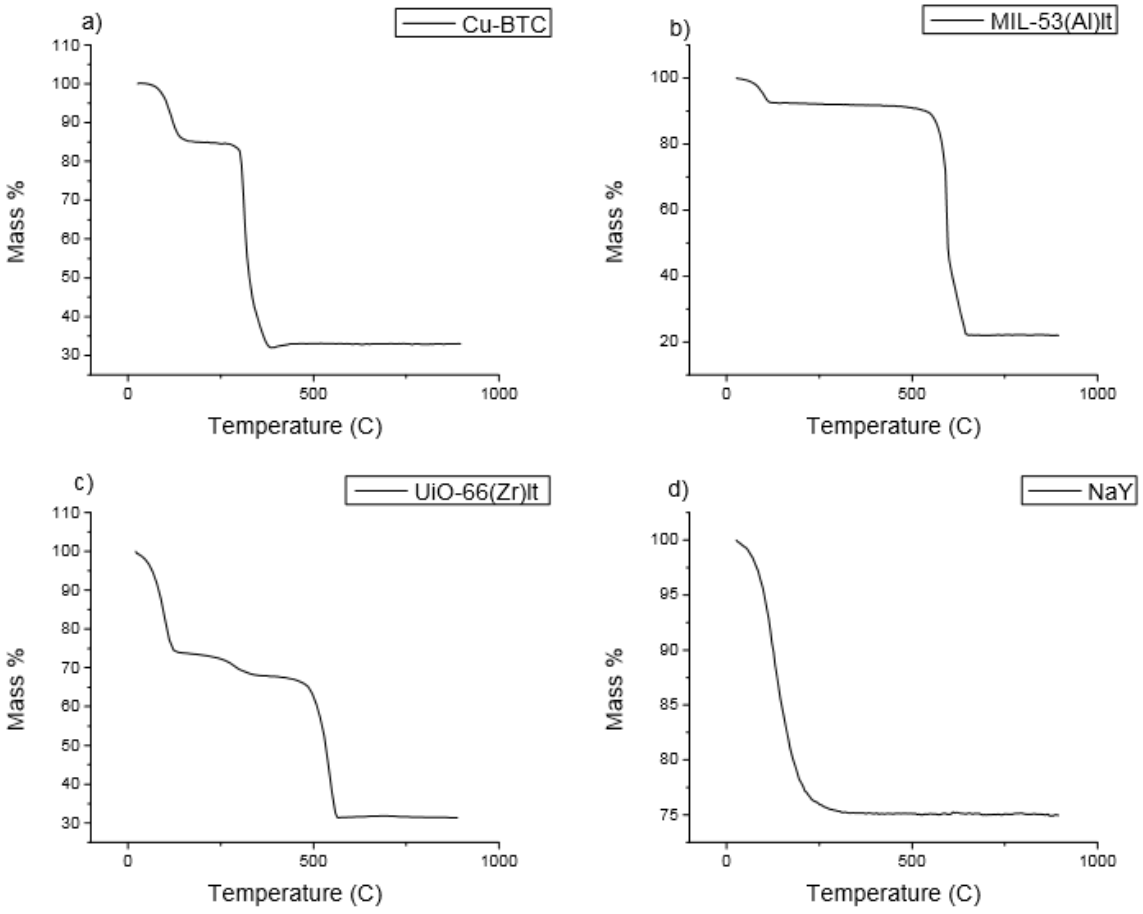

Figure 25: Thermogravimetric weight loss curves of chosen fresh materials: (a) Cu-BTC, (b) MIL-53(Al), (c) UiO-66(Zr), and (d) NaY.

4.1.3 SEM Images

The SEM images of the chosen materials used to determine the crystal size range listed in Table 3 are shown in Figure 26. The crystal sizes are all in the range of 1 to 7 microns.

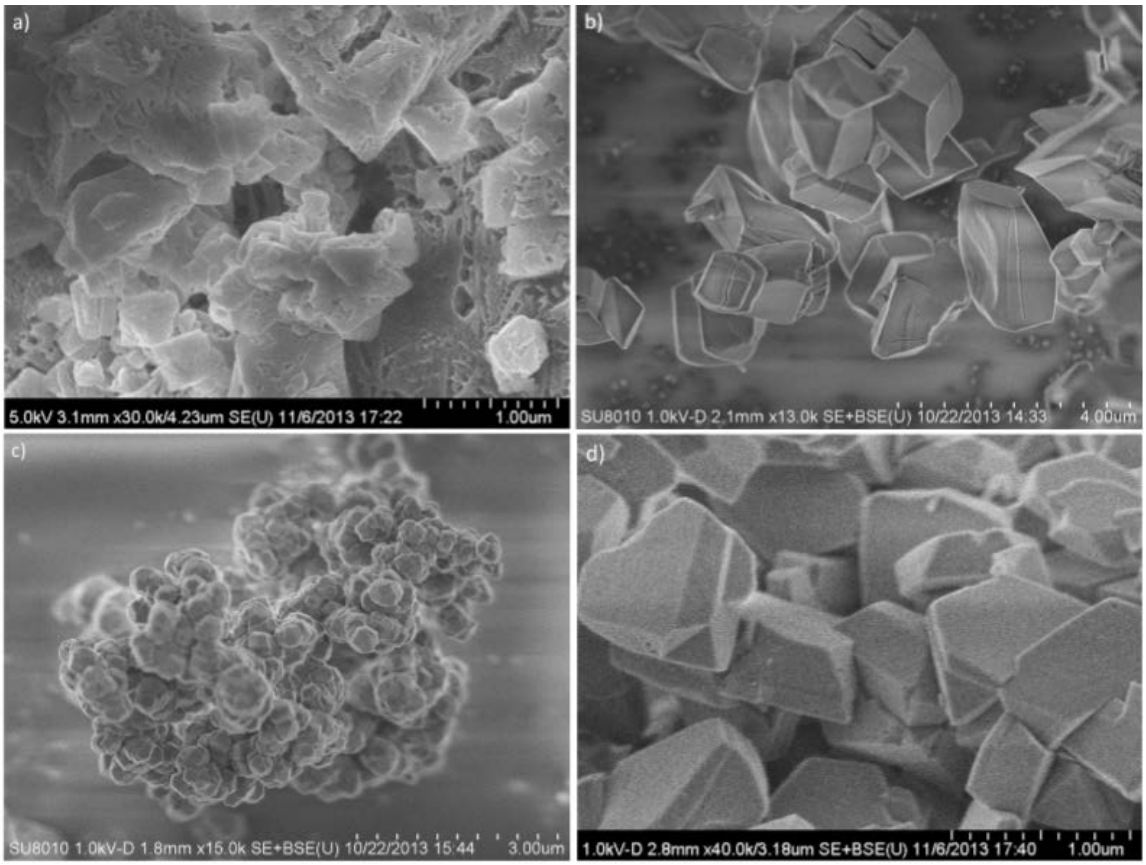

Figure 26: SEM images of chosen fresh materials: (a) Cu-BTC, (b) MIL-53(Al), (c) UiO-66(Zr), and (d) NaY.

4.2 Initial Screening Experiments with Model Natural Gas

The TGA setup inside a fume hood for performing the adsorption experiments in this chapter and Chapter 4 is pictured in Figure 27. A manual switch and bubble flow meter were used to switch the feed gas between the helium desorption gas and the adsorptive gas.

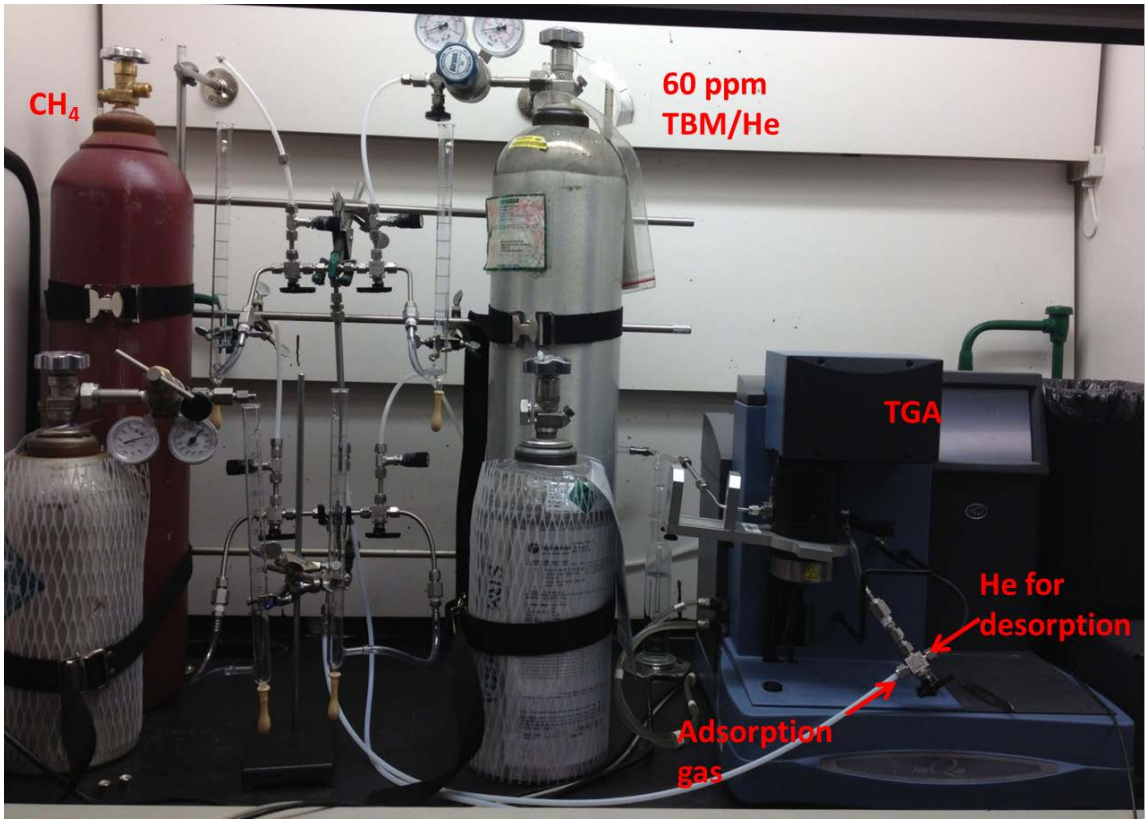

Figure 27: Photo of the adsorption TGA system setup located inside a fume hood, with inert desorption gas flowing in from the right (He cylinder located outside of the hood) and flammable adsorption gas flowing in from the left. All plastic tubing pictured here were switched out to stainless steel tubing.

Figure 28 shows the initial equilibrium uptake of a gas mixture of 60 ppm of TBM in methane of all adsorbents screened in this study (other collected data, shown in

later sections, were further used to estimate what fraction of this uptake was TBM as opposed to methane or other gas impurities). Cu-BTC and MIL-53(Al) display significantly higher uptakes of 0.30 and 0.22 g/g of adsorbent respectively than the benchmark zeolite NaY at 0.16 g/g of adsorbent. All other materials had lower uptakes than NaY. However, UiO-66(Zr), with an uptake of 0.09 g/g of adsorbent, has shown remarkable stability in the presence of water vapor and selectivity toward acid gases over methane and water in the past literature.[100, 106-108] On the basis of these initial screening results, the MOFs Cu-BTC, MIL-53(Al), and UiO-66(Zr) were chosen as the most promising new materials for further study as well as zeolite NaY for comparison as the highest performing (in terms of fresh material capacity) benchmark material.

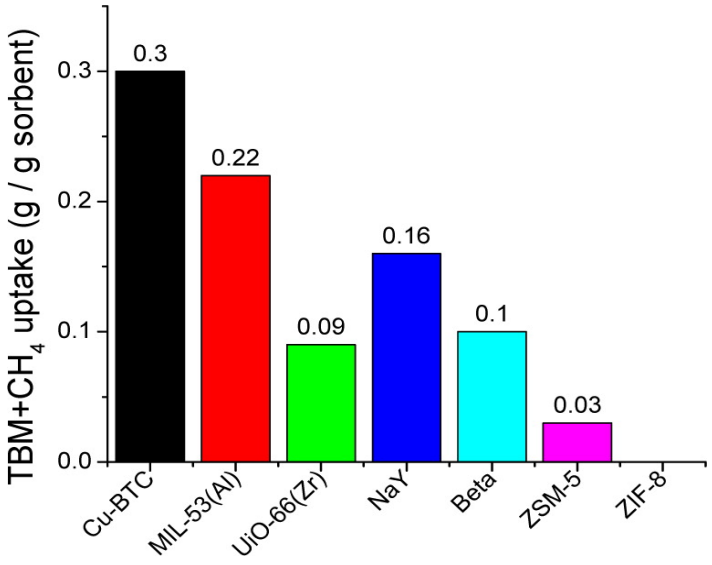

Figure 28: Initial equilibrium uptake of several materials in grams of gas adsorbed per gram of fresh material in a flowing model natural gas feed (60 ppm of TBM in methane) at 1 atm and 35°C.

4.3 Cyclic Regenerability of Selected Materials

Cyclic regenerability is important for implementation in a practical process to reduce the costs associated with adsorbent replacement. Because of the low partial pressures of TBM gas used in this application, a temperature swing adsorption (TSA) technique using changes in the temperature to release the adsorbed gas is employed instead of pressure or vacuum swing adsorption. An example of the raw sample weight as a function of time data recorded by the TGA over multiple cycles of adsorption and desorption is shown in Figure 29.

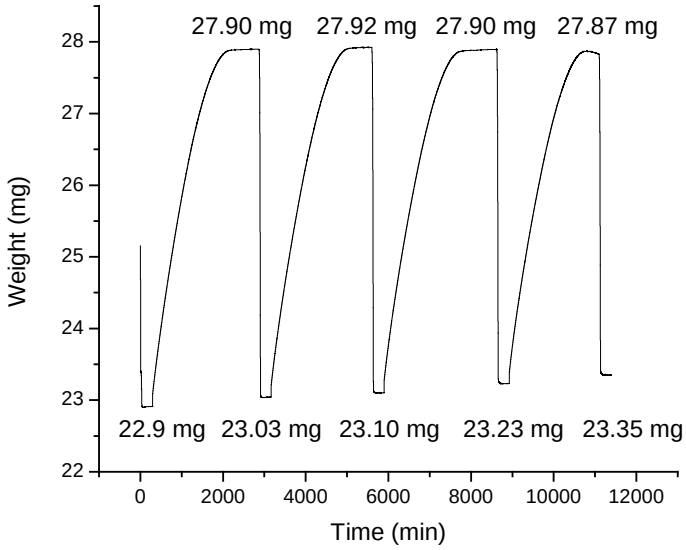

Figure 29: Example of raw TGA data for MIL-53(Al) showing multiple cycles of adsorption of model natural gas (60 ppm TBM/CH_4) at 35°C and desorption at 200°C in flowing helium.

The target initial sample weight to be loaded into the TGA is between 20-30 mg. In the example, about 25 mg is loaded initially, then the sample loses approximately 2 mg during the initial pretreatment / desorption step. This stable weight of approximately 23 mg at the end of the desorption step is the weight of the "clean" sample which is mostly

free of any guest molecules which may have been left over from synthesis or adsorbed from the atmosphere. The subsequent weight gain of the sample up to approximately 28 mg happens during the adsorption step as the sample adsorbs TBM. Once the sample has reached equilibrium adsorption, defined as a weight change of >0.1% over 1 hour, the sample is once again desorbed for the next cycle using the same temperature and flow rate as the pretreatment step.

To estimate the uptake capacity of the material in each cycle from the TGA raw data, the sample weight gain in each adsorption cycle is first calculated by subtracting the weight of the sample at the very end of the desorption step (once the sample has been equilibrated at the adsorption temperature under inert gas) from the weight of the sample at the end of the adsorption step (at equilibrium adsorption capacity). The weight gain is then divided by the weight of the sample at the end of the high temperature portion of the desorption step (the weight of the "clean" sample without guest molecules) to get the uptake value in g/g sorbent. The uptake of the chosen materials over 5 cycles of adsorption−desorption is shown in Figure 30.

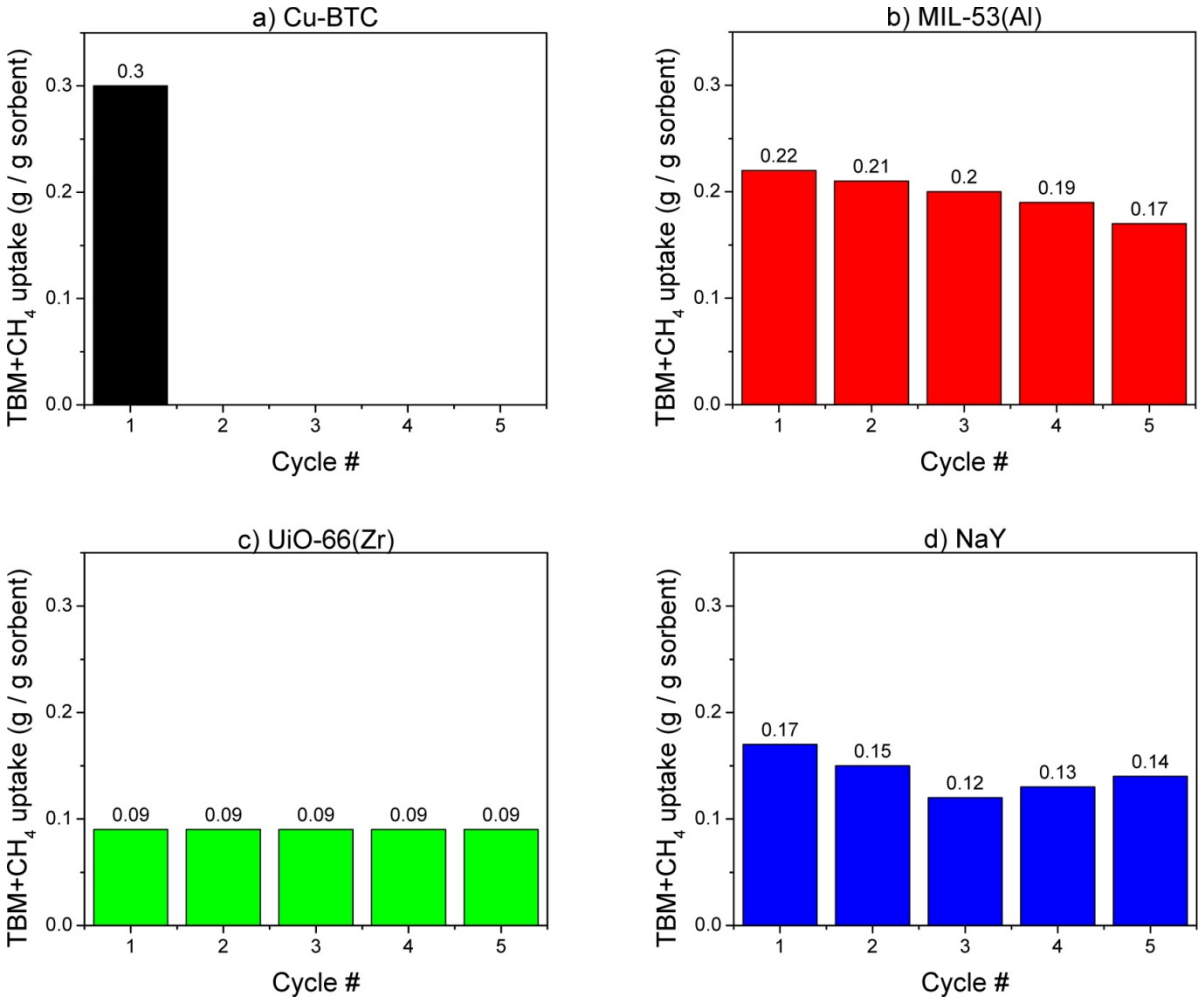

Figure 30: Cyclic regenerability of chosen materials toward model natural gas feed (60 ppm of TBM in methane) at 1 atm and 35°C: (a) Cu-BTC, (b) MIL-53(Al), (c) UiO-66(Zr), and (d) NaY.

From Figure 30(a), it can be seen that Cu-BTC loses all of its uptake capability (100% capacity loss compared to the fresh sample) after just 1 cycle of TBM adsorption. Figure 30(b) shows that MIL-53(Al) loses about 4−7% of its uptake capability in each subsequent TBM adsorption cycle after the first cycle, such that, after 5 cycles, it has lost 19.9% of its initial uptake. Because the initial uptake of MIL-53(Al) is so high, its fifth cycle uptake of 0.17 g/g of adsorbent is still higher than that of the initial uptakes of UiO-66(Zr) and NaY. However, the continuously decreasing uptake capability trend showed

no signs of stabilization, even beyond the fifth regeneration cycle, as shown in Figure 31. Figure 30(c) shows that UiO-66(Zr) is remarkably stable and displays no significant changes in uptake over all 5 TBM adsorption cycles. Figure 30(d) shows that NaY loses 13.6 and 14.7% of its uptake capability in cycles 2 and 3, respectively; however, unlike MIL-53(Al), this trend stabilizes after the third cycle, such that, after 5 cycles, it has lost only 23.6% of its initial uptake and the capacity still remains at a relatively high value of 0.14 g/g of adsorbent. The reasons behind these trends are explored in detail later in sections.

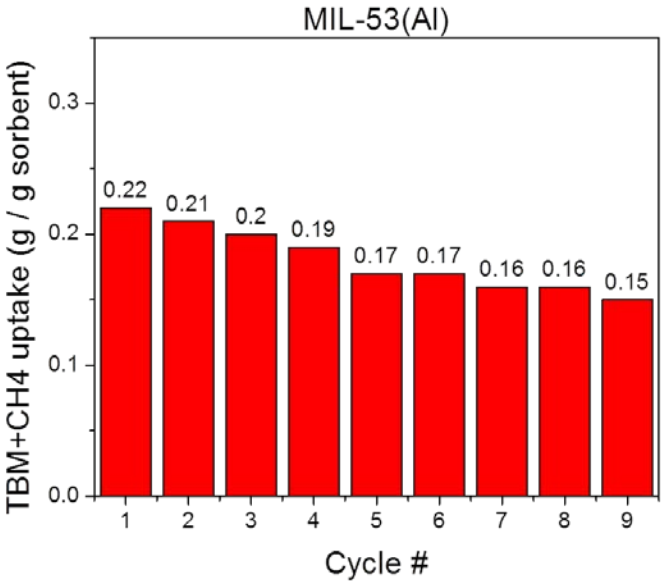

Figure 31: Cyclic uptake of MIL-53(Al) using a model natural gas feed (60 ppm of TBM in methane) at 1 atm and 35°C.

When the data in Figure 30 are normalized to grams of TBM per mole of metal in MOF, the same general trend appears in first cycle uptake values, with Cu-BTC having the highest uptake, followed by MIL-53(Al) and then UiO-66(Zr). However, the ratios of uptakes are slightly different. Cu-BTC shows an uptake of 93.73 g of TBM/mol of Cu;

MIL-53(Al) shows an uptake of 44.97 g of TBM/mol of Al; and UiO-66(Zr) shows an uptake of 34.35 g of TBM/mol of Zr. In terms of ratios, the uptake values shown in the form of grams of TBM per gram of sorbent in Figure 30, Cu-BTC and MIL-53(Al) display uptake values 2.4 and 3.3 times higher than that of UiO-66(Zr), respectively, whereas for uptake values normalized in the form of grams of TBM per mole of metal in MOF, Cu-BTC and MIL-53(Al) display uptake values 1.3 and 2.7 times higher than that of UiO-66(Zr), respectively.

It is likely that strong interactions between TBM molecules and the open metal sites of Cu-BTC lead to its framework destruction and incomplete evacuation with the regeneration treatment. In contrast, MIL-53(Al) and UiO-66(Zr) lack these open metal sites, which may contribute to their partial to full regenerability while still maintaining a high sulfur uptake capacity. Adsorption sites created from structural defects or impurities may also contribute to the adsorption properties of both MOFs and zeolites.

4.4 Estimated Selectivity

The adsorption selectivity of materials toward TBM over methane and natural gas impurities is important for implementation in a practical system (which contains both) to increase process efficiency, reduce waste, and lower energy costs. The uptake capabilities of the chosen materials for a 99.0% methane cylinder (same grade as used in the 60 ppm of TBM in methane model natural gas mixture) and for a mixture of 60 ppm of TBM in UHP helium are shown in Figure 32.

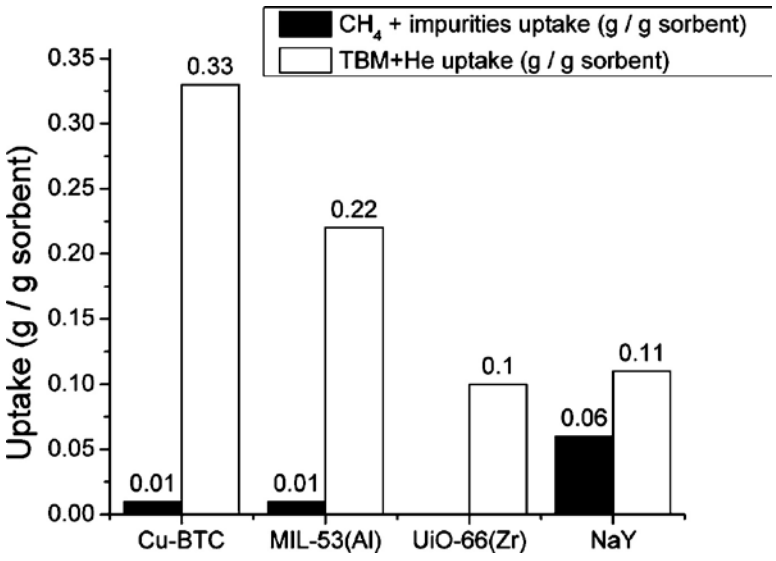

Figure 32: Equilibrium uptake of selected materials in grams of gas adsorbed per gram of fresh material toward both methane gas and a gas mixture of 60 ppm of TBM in UHP helium at 1 atm and 35°C.

In comparison to the uptake capabilities of the materials to 60 ppm of TBM in model natural gas shown in Figure 28, Cu-BTC displays a slightly higher uptake when exposed to TBM in an inert gas, indicating that adsorption of TBM may be slightly hindered by the presence of methane or other impurities for this material. There are no significant differences in the uptake capabilities of MIL-53(Al) and UiO-66(Zr) between the TBM mixture in helium versus 99.0% methane, indicating no hindrance or other effects because of the carrier gas.

Other studies on mercaptan adsorption on MIL-53(Al) have indicated a higher isosteric heat of adsorption for methyl mercaptan than methane, indicating mercaptans interact more with the adsorption sites on MOFs and are therefore more selective towards mercaptans than methane.[109] This selectivity is likely due to the polarity of mercaptans versus the non-polarity of methane. In contrast, NaY shows a significantly lower TBM capacity for the mixture in helium versus the mixture in methane. This indicates that NaY

is adsorbing a large amount of other gases, likely trace amounts of water because of its well-known hydrophilicity, from the TBM in methane feed gas, and that its true uptake for TBM alone is closer to 0.11 g/g of adsorbent rather than the 0.16 g/g of adsorbent estimated above.

Equation (19) below was used to calculate a lower bound for material selectivity toward TBM over methane and other impurities in the 60 ppm of TBM in 99.0% methane gas mixture:

$$S_{TBM/CH_4} = \frac{x_{TBM,adsorbed} / x_{CH_4,adsorbed}}{y_{TBM,bulkgas} / x_{CH_4,bulkgas}} \quad (19)$$

where $y_{TBM,\ bulk\ gas}$ is the mole fraction of TBM in the bulk gas phase (feed) contacting the adsorbent, $y_{CH4,\ bulk\ gas}$ is the mole fraction of the rest of the bulk gas feed, $x_{TBM,\ adsorbed}$ is the estimated mole fraction of TBM adsorbed inside the adsorbent, and $x_{CH4,\ adsorbed}$ is the estimated mole fraction of the rest of the gas adsorbed (calculated as $1 - x_{TBM,\ adsorbed}$). The mole fraction of TBM adsorbed was estimated by subtracting the uptake of the material for the 99.0% methane gas alone from the uptake of the material for the 60 ppm of TBM in methane gas mixture, and this was considered to be the lower bound uptake capability for TBM alone. This lower bound uptake was then divided by the total uptake of the material for the 60 ppm of TBM in methane gas mixture to obtain the lower bound mole fraction of TBM adsorbed in the material and subsequently used in equation (19) to calculate the minimum selectivity, as shown in Table 4.

Table 4: Minimum selectivities of the selected materials for TBM over methane and other gas impurities in the model natural gas (60 ppm TBM/CH_4) at atmospheric pressure and 35°C adsorption temperature

Sample	Minimum selectivity
Cu-BTC	228,000
MIL-53(Al)	263,000
UiO-66(Zr)	198,000
Zeolite NaY	14,000

These selectivities represent the most conservative estimate, assuming that the 99.0% methane present in the TBM/methane gas mixture will adsorb on the materials until saturation, and only then will the rest of the adsorption sites be populated with TBM molecules until equilibrium. From Table 4, it is clear that the MOF materials are all more selective toward TBM than the benchmark zeolite NaY. Additionally, the true uptake of NaY toward TBM as measured by the 60 ppm of TBM in helium mixture, shown in Figure 32, is much closer to that of UiO-66(Zr), again making UiO-66(Zr) interesting for further study as a promising candidate material for implementation in a practical system, because it is both more selective and regenerable for the same capacity performance and stability as the benchmark zeolite material, and is not as sensitive to water as NaY.

4.5 Methods of Deactivation

4.5.1 Nitrogen physisorption isotherms after TBM adsorption

The BET surface area and t-plot micropore volume of the materials were measured again after exposure to 5 cycles of TBM adsorption. The results are summarized in Table 5.

Table 5: Surface areas and pore volumes of adsorbent materials after 5 cycles of TBM exposure

Sample	BET Surface Area (m^2/g)	t-plot Micropore Volume (cm^3/g)
Cu-BTC	53	0.01
MIL-53(Al)	972	0.40
UiO-66(Zr)	1142	0.41
Zeolite NaY	653	0.28

In comparison to the fresh material, Cu-BTC experiences a near complete loss in surface area and pore volume, indicating a total structural collapse. MIL-53(Al) shows slight decreases in surface area and pore volume, which could be due to some degree of irreversible binding of TBM on the surface and / or a change in crystallinity, which leads to the continuous decrease in uptake over each adsorption cycle. These potential reasons for capacity decrease over the cycles will be discussed in more detail later. UiO-66(Zr), in contrast, experiences no significant changes in either surface area or pore volume, giving evidence that its structure remains intact and unchanged even after the repeated exposure. NaY shows small decreases in surface area and pore volume, likely because of small amounts of residual TBM and/or water molecules accumulated during the feed gas

adsorption cycles that could not be removed at the relatively low zeolite desorption temperature of 200 °C. However, it was desired to keep this variable constant across all materials used in this study, and therefore, a higher desorption temperature was not used, even for zeolites.

4.5.2 XRD patterns before and after TBM adsorption

The XRD patterns of the fresh materials versus those of the materials after 5 cycles of TBM exposure are shown in Figure 33. The XRD patterns for the fresh samples (before TBM exposure) for Cu-BTC,[98] MIL-53(Al),[101] UiO-66(Zr),[100] and NaY[110] matched well with those reported in the previously published literature.

From Figure 33(a), with the loss of all crystalline peaks in the "after TBM exposure" sample, it is clear that Cu-BTC loses essentially all of its crystallinity upon exposure to the TBM-containing gas, suggesting a complete breakdown of the MOF structure because of gas exposure.

Figure 33(b) shows a significant change in the crystal structure of MIL-53(Al) after TBM exposure, evidenced by shifts in the peak position for the after TBM sample relative to the fresh sample, which may contribute to the stepwise decrease in sulfur adsorption capacity with each cycle. This crystallinity change is likely due to the MOF shifting from the MIL-53(Al) *lt* form to the MIL-53(Al) *ht* form.[99] MIL-53(Al) has a flexible network structure with a large breathing effect, whereby during hydration at room temperature, a water molecule occupies the center of each channel. The water molecules contribute to hydrogen-bonding within the structure, which closes the channels

of the MOF; in this form, it is named MIL-53(Al) *lt* and has the XRD pattern of the "fresh" material shown in Figure 33(b). At higher temperatures, the water molecules are desorbed and leave the structure in its open form with empty channels; this form is named MIL-53(Al) *ht* and has the XRD pattern of the "after TBM" material shown in Figure 33(b).[99]

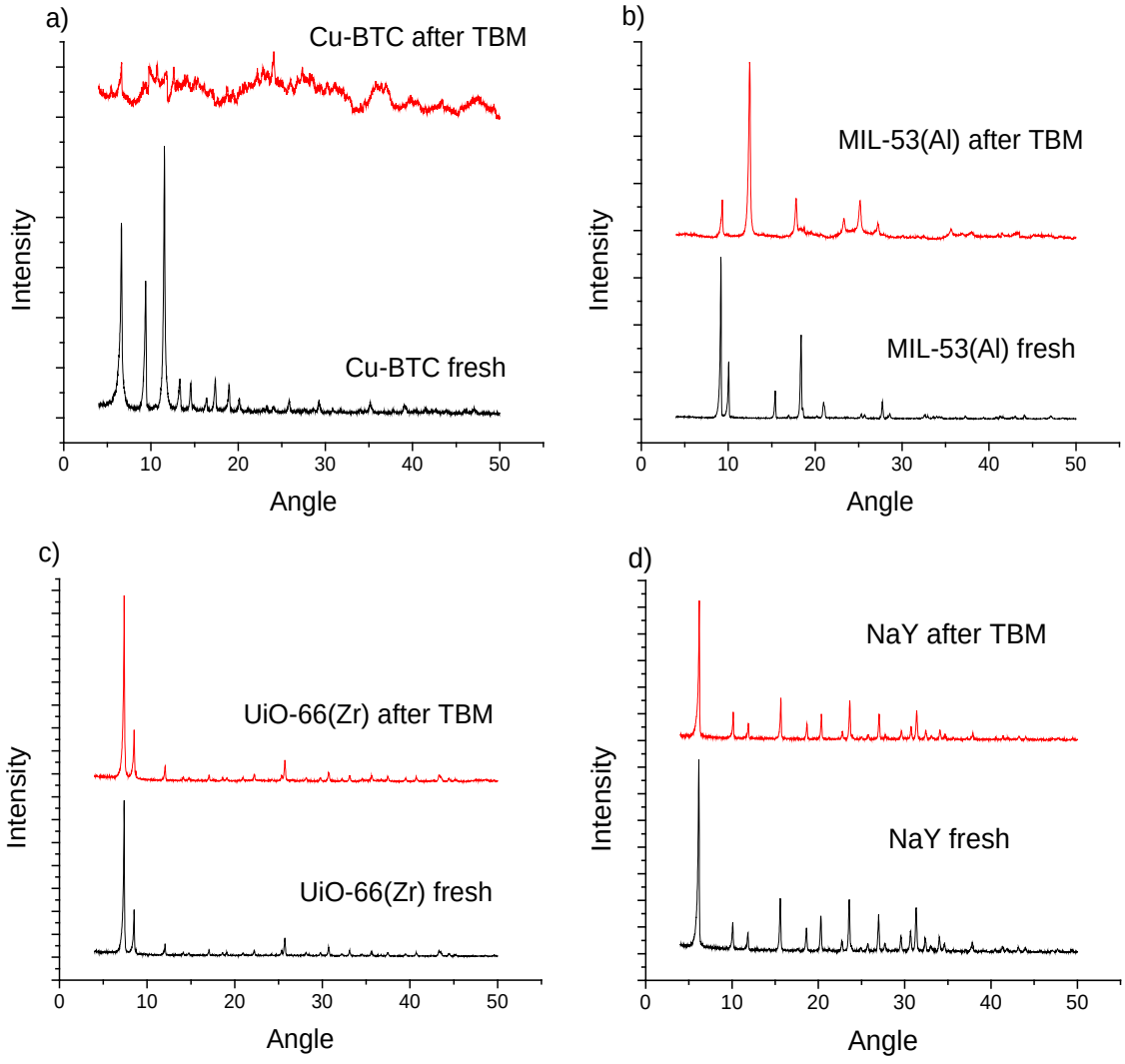

Figure 33: XRD patterns of chosen materials before and after 5 cycles of TBM exposure: (a) Cu-BTC, (b) MIL-53(Al), (c) UiO-66(Zr), and (d) NaY.

Though the XRD of the “after TBM” sample was taken at room temperature and not a high temperature where water molecules would normally leave the structure, a possible explanation is that TBM was not fully desorbed from the sample and the large TBM molecules occupying the channels change the structure to its large pore (MIL-53(Al) *ht*) form.

Panels (c) and (d) of Figure 33 show no significant changes in the crystallinity peaks of UiO-66(Zr) and NaY after TBM exposure, suggesting no significant changes in their crystal structures. There may be a slight increase in crystallinity of the exposed UiO-66(Zr) sample, which may contribute to the very slight increase in capacity over 5 TBM adsorption cycles. It is hypothesized that this is due to trace amounts of remaining synthesis solvent being released from the MOF with each desorption cycle. In contrast, there may be a slight decrease in crystallinity of the exposed NaY, which may contribute to the slight decrease in capacity over the first 3 TBM adsorption cycles.

4.5.3 XPS results before and after TBM adsorption

The XPS results showing the surface composition of the selected materials before and after 5 cycles of TBM exposure are summarized by Figure 34.

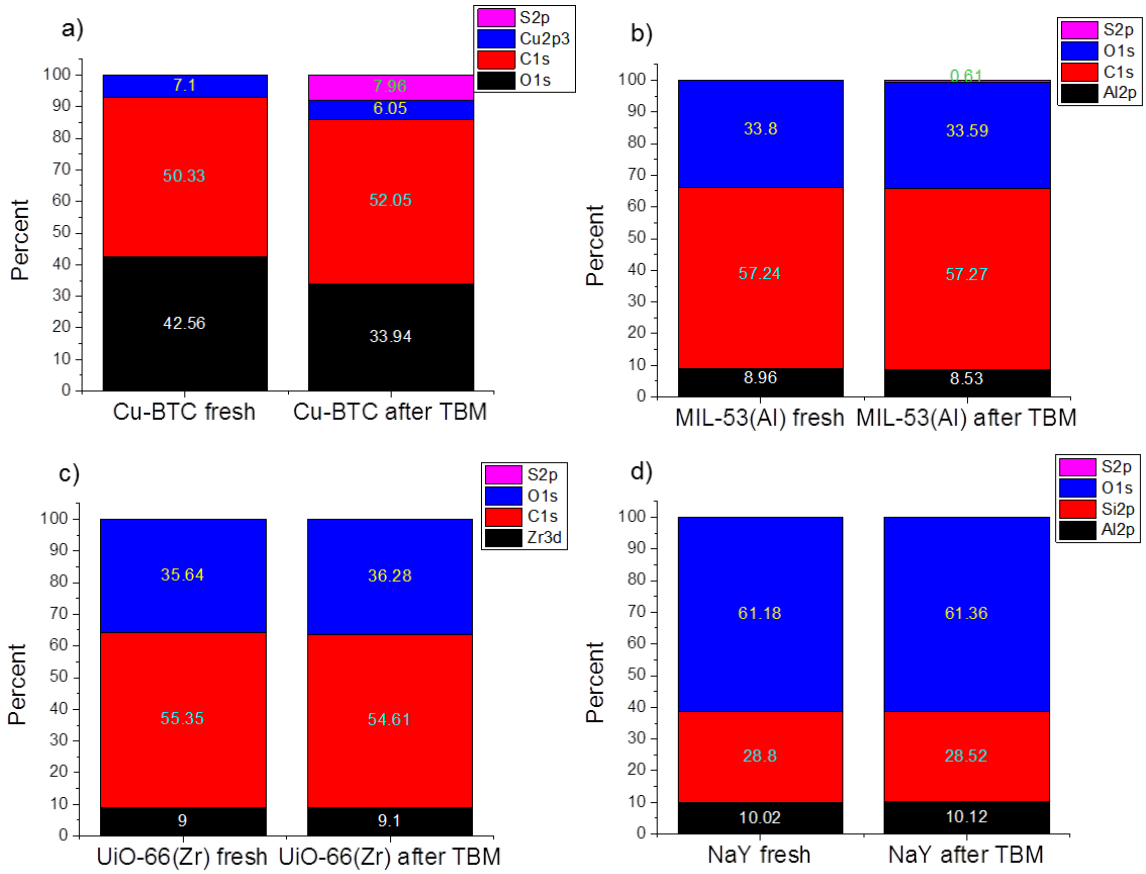

Figure 34: XPS surface composition results of chosen materials before and after 5 cycles of TBM exposure: (a) Cu-BTC, (b) MIL-53(Al), (c) UiO-66(Zr), and (d) NaY.

It can be seen from Figure 34(a) that Cu-BTC retains a significant amount of TBM on its surface after exposure, indicated by the about 8% of sulfur detected in the after exposure material that is absent from the fresh sample. This inability for all of the TBM to be removed even after thermal treatment likely also contributes (along with crystallinity loss) to the inability of Cu-BTC to be regenerated. In addition, an analysis of the Cu 2p spectra peak values shows a binding energy shift of 0.4 eV in the first peak and a shift of 0.66 eV in the second peak between the fresh Cu-BTC sample and the Cu-BTC sample after 5 cycles of TBM adsorption. These shift values suggest a shift to one higher oxidation state in the used sample. Figure 34(b) shows that MIL-53(Al) retains a small

amount of TBM on its surface after exposure; nearly 1% of its elemental composition for the TBM-exposed sample is sulfur. Therefore, this incomplete desorption likely contributes to the gradual decrease in capacity of MIL-53(Al) with each regeneration cycle. Panels (c) and (d) of Figure 34 show that neither UiO-66(Zr) nor NaY retain any detectable TBM after exposure, and both maintain the same surface elemental composition before and after the 5 adsorption cycles, which is consistent with the cyclic adsorption results above.

4.5.4 Elemental analysis before and after TBM adsorption

Elemental analysis (EA) was also performed on the fresh and used materials to determine their bulk compositions, which are shown in Table 6 for Cu-BTC, MIL-53(Al), UiO-66(Zr), and NaY.

Table 6: Elemental analysis (EA) bulk composition results of chosen materials before and after 5 cycles of TBM exposure: (a) Cu-BTC, (b) MIL-53(Al), (c) UiO-66(Zr), and (d) NaY

Sample	C (wt%)	H (wt%)	Cu (wt%)	Zr (wt%)	Al (wt%)	Si (wt%)	S (wt%)
Cu-BTC fresh	28	4	20	n/a	n/a	n/a	n/a
Cu-BTC after TBM	19	2	34	n/a	n/a	n/a	10
MIL-53(Al) fresh	43	4	n/a	n/a	13	n/a	n/a
MIL-53(Al) after TBM	43	4	n/a	n/a	12	n/a	1
UiO-66(Zr) fresh	26	5	n/a	27	n/a	n/a	n/a
UiO-66(Zr) after TBM	26	4	n/a	23	n/a	n/a	0
NaY fresh	n/a	n/a	n/a	n/a	9	26	n/a
NaY after TBM	n/a	n/a	n/a	n/a	10	24	0

While there are some discrepancies in the actual weight percentage values measured between the surface elemental measurement of XPS and bulk measurement of EA, the same general trends appear. For the used materials, elemental sulfur is present in a significant amount on Cu-BTC, in trace amounts on MIL-53(Al), and negligible on UiO-66(Zr) and NaY after exposure to 5 cycles of TBM adsorption.

4.5.5 UV-vis spectra before and after TBM adsorption

The UV−vis spectra of selected materials before and after 5 cycles of TBM exposure are shown in Figure 35. Figure 35(a) shows a significant difference for fresh Cu-BTC versus that after exposure, also potentially indicating a change in the copper oxidation state or decoordination from ligands. This was visually obvious in the sample itself as well, with a color change in the Cu-BTC MOF from blue to black. In contrast, panels (b)−(d) of Figure 35 show no significant changes in the light absorption and, therefore, the bonds of the other materials were also presumably unchanged, though slight discolorations were observed in all three materials, changing from white to light grey.

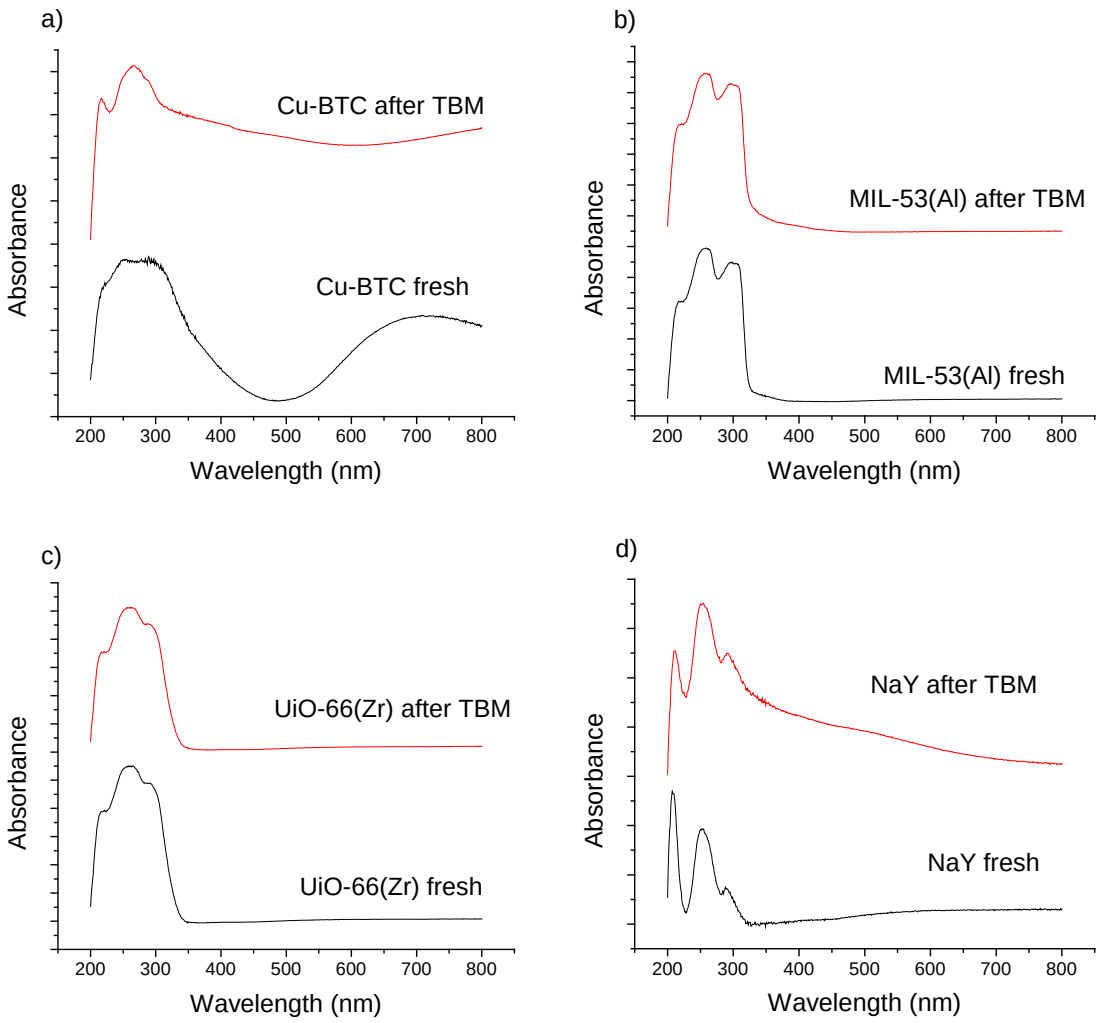

Figure 35: UV-vis spectra of chosen materials before and after 5 cycles of TBM exposure: (a) Cu-BTC, (b) MIL-53(Al), (c) UiO-66(Zr), and (d) NaY.

4.5.6 Raman spectra before and after TBM adsorption

The Raman spectra of the selected materials before and after 5 cycles of TBM exposure are shown in Figure 36. From Figure 36(a), it can be seen that Cu-BTC is completely destroyed and likely all metal−ligand bonds are broken after TBM exposure, which would definitely contribute to the tremendous capacity loss after the first adsorption cycle. Unfortunately, although Cu-BTC has the highest sulfur capacity out of

all of the materials in this study and good selectivity, it is not suitable for practical applications of odorant removal from natural gas because of its total structural collapse, leading to total capacity loss after just 1 adsorption cycle. Panels (b) and (c) of Figure 36 show no significant changes in the Raman spectra before and after TBM exposure for MIL-53(Al) and UiO-66(Zr), indicating that there is no significant irreversible binding or reactions happening in the structures as a result of TBM exposure. For MIL-53(Al), this suggests that the capacity loss is mostly or only due to changes in its crystal structure rather than changes in molecular bonds or irreversible sulfur uptake and that it may be possible to recover some of this lost capacity by solvent exchange or heat treatment to revert the crystal structure back to its original form. This Raman spectroscopy result for UiO-66(Zr) is consistent with the cyclic adsorption and other sample characterization results for this material, demonstrating the extreme stability, selectivity, and regenerability of this MOF. Unfortunately, as shown in Figure 36(d), no useful Raman data were obtained of NaY as a result of the sample giving no signal or fluorescing.

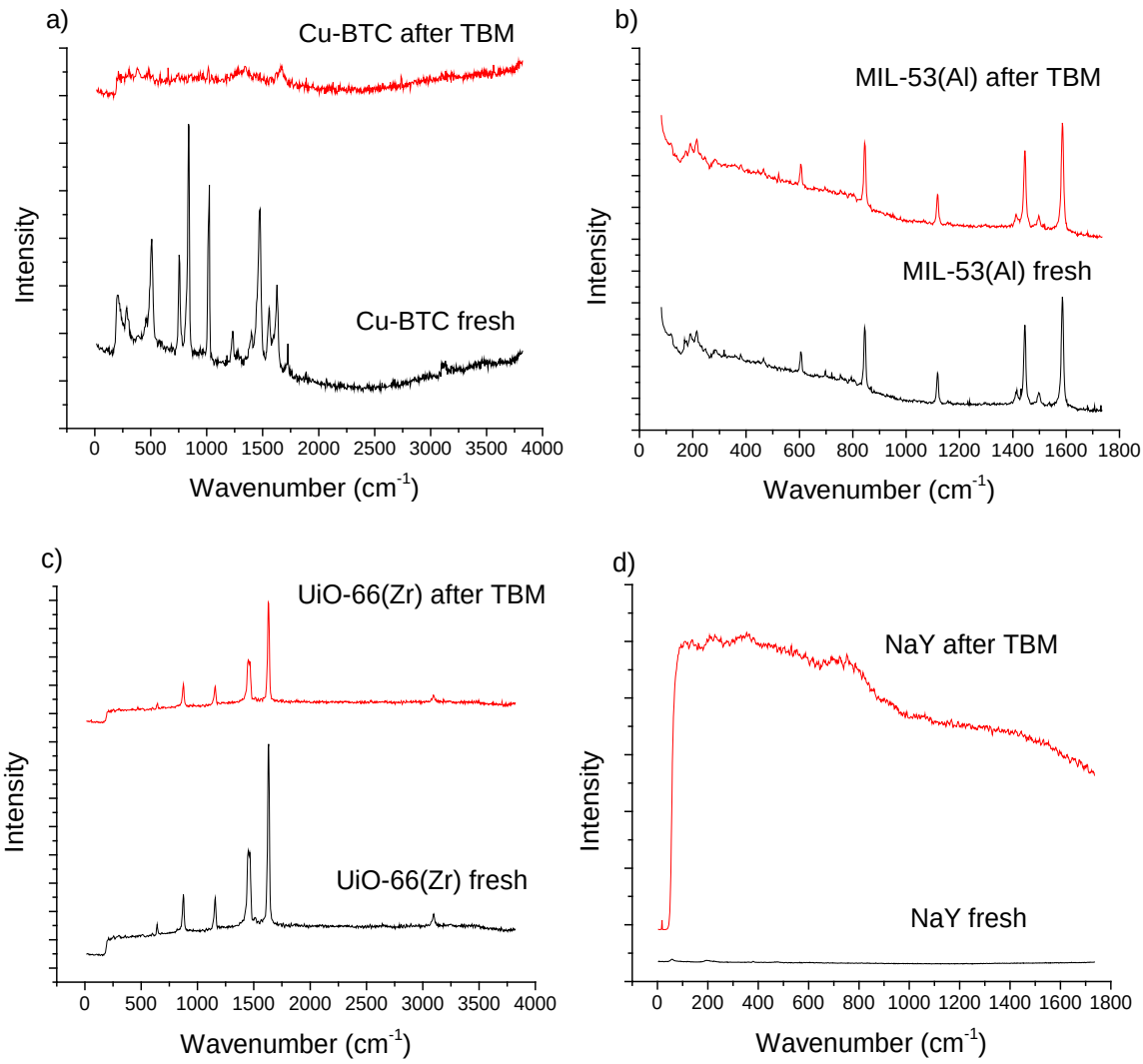

Figure 36: Raman spectra of chosen materials before and after 5 cycles of TBM exposure: (a) Cu-BTC, (b) MIL-53(Al), (c) UiO-66(Zr), and (d) NaY.

Zeolite NaY would not be selective toward TBM over water, whereas according to the literature, UiO-66(Zr) is more selective toward acid gases over methane and water, and its characteristics remain unchanged even after the adsorption of these compounds.[107, 111-112] Coupled with a capacity comparable to that of benchmark zeolite NaY, UiO-66(Zr) is a promising new adsorbent material for the removal of odorants from

natural gas in a practical system. Currently, the cost of the few commercially available MOF materials, such as Cu-BTC, available as Basolite C 300 from Sigma-Aldrich for $16,280 per kg, and MIL-53(Al), available as Basolite A 100 from Sigma-Aldrich for $9,590 per kg, are prohibitively high for implementation in a commercial system. Zeolite NaY, in contrast, can cost as little as $10 per kg when purchased on a large scale. A technoeconomic analysis of a cellulose acetate−zeolite 13X hybrid fiber sorbent module system for the removal of TBM from natural gas was performed in our previous work, and the estimated raw material costs to make one commercial scale fiber sorbent module was $4,300 per module.[12] Again, while this current MOF cost is today not practical for a commercial-scale system, because MOFs are relatively new sorbent materials with promising properties for many applications, their high costs will decrease over time such that they may eventually become a viable option for commercial adsorption applications.

CHAPTER 5

HYBRID FIBER ADSORBENT FABRICATION, CHARACTERIZATION, AND PERFORMANCE RESULTS

5.1 Initial Syringe Fiber Spinning and Characterizations of Materials

5.1.1 Syringe fiber formation with MOF and zeolite sorbents

Initially, syringe fibers were formed with an easily achievable target sorbent weight loading of 50 wt % to evaluate the general tolerance of the sorbents to the spinning process and the performance of the hybrid fibers. The spin dopes created from MIL-53(Al), UiO-66(Zr), and NaY, and syringe fiber formation are shown in the pictures in Figure 37 below.

Figure 37: Photos of the spin dopes of MIL-53(Al), UiO-66(Zr), and NaY (in order from left to right in the left side photo), and spin dope loaded into a syringe for initial syringe fiber formation (right).

During formation of the MIL-53(Al)/CA syringe fibers, the water quench bath became cloudy as the fibers were extruded into it and also during subsequent solvent exchanges. This suggests that the MIL-53(Al) dissolved and disintegrated back into its precursor components in the water. Because of this instability in liquid water, noted before in the literature,[106] MIL53(Al) was eliminated from consideration for fiber spinning with the spinneret apparatus. In contrast, NaY and UiO-66(Zr) dopes were easily extruded into fibers with no observable cloudiness in the water quench bath or during solvent exchange, and dried fibers showed good mechanical strength. All three syringe fibers are pictured in Figure 38 in their water quench baths. Larger volume dopes with varying sorbent loadings were therefore made with these two sorbents for spinneret fiber spinning and further characterization and adsorption testing.

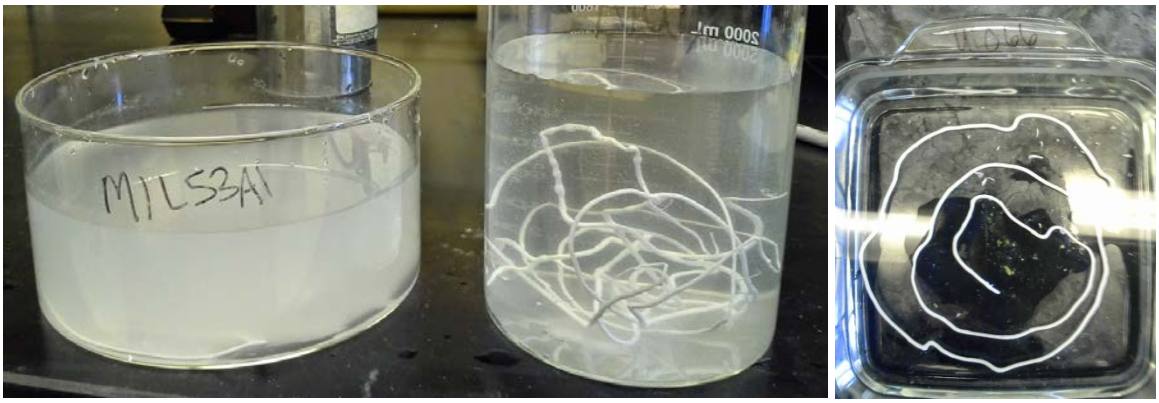

Figure 38: Photos of the initial 50 wt% sorbent loaded extruded syringe hybrid fibers of MIL-53(Al)/CA, NaY/CA, and UiO-66(Zr)/CA (in order from left to right).

5.1.2 Large batch versus small batch synthesis of UiO-66(Zr) for fiber spinning

Spinneret fiber spinning requires a minimum of ~50 g of sorbent material, especially for high sorbent loaded fibers. At the time of this portion of the study, the

synthesis procedure available in the literature for MOF UiO-66(Zr) had only been tested for small batch yields of 1 g or less, and UiO-66(Zr) has only recently become commercially available for research purposes only, an alternative proprietary large-batch synthesis procedure developed by Schoenecker et al.[102] was used to produce enough material to make spinneret fibers. As seen in Table 7, Table 8, and Figure 39 below, there is little difference between the UiO-66(Zr) materials synthesized using the original small-batch (labeled SB) technique and the new proprietary large-batch (labeled LB) technique.

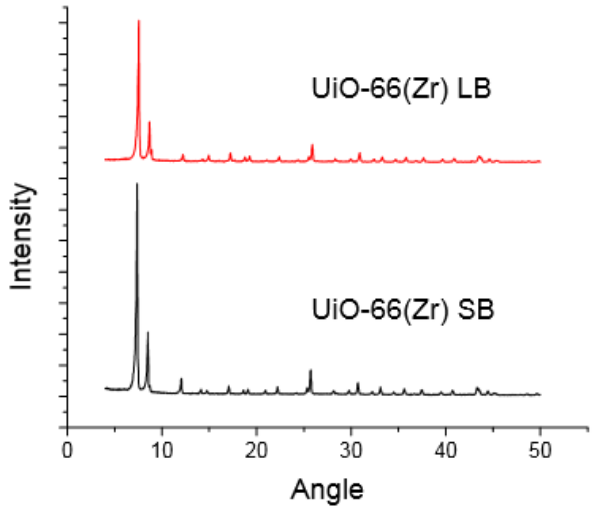

Figure 39: XRD pattern comparison showing good agreement between UiO-66(Zr) made using large batch (LB) and small batch (SB) techniques.

The XRD patterns of UiO-66(Zr) synthesized using the original small batch (SB) technique versus that of the proprietary large batch (LB) technique are shown in Figure 39. The patterns show good agreement, displaying the same peak positions, though the LB shows slightly lower signal intensity. Thus, all subsequent fiber studies were conducted using the UiO-66(Zr) synthesized with the LB technique.

Table 7: Elemental analysis results of the powder sorbent samples and hybrid polymer-sorbent fibers at various sorbent weight loadings

Sample	Carbon (wt %)	Hydrogen (wt %)	Nitrogen (wt %)	Aluminum (wt %)	Silicon (wt %)	Zirconium (wt %)
NaY sieve	n/a	n/a	n/a	9	26	n/a
75 wt% NaY/CA fiber	10	4	0	8	18	n/a
50 wt% NaY/CA fiber	20	4	0	5	12	n/a
UiO-66(Zr) SB sieve	32	5	1	n/a	n/a	24
UiO-66(Zr) LB sieve	33	4	3	n/a	n/a	25
75 wt% UiO-66(Zr)/CA fiber	38	4	0	n/a	n/a	21
50 wt% UiO-66(Zr)/CA fiber	42	5	0	n/a	n/a	14
Sorbent-free CA fiber	49	6	0	n/a	n/a	n/a

5.1.3 Nitrogen physisorption isotherms of fiber sorbents

The nitrogen physisorption isotherms used to calculate the Brunauer−Emmett−Teller (BET) surface areas and micropore volumes of NaY, UiO-66(Zr), and MIL-53(Al) in original sieve forms (powders) and after being spun into cellulose acetate polymer fibers at various sorbent loadings are shown in Figure 40. All materials, including fibers, displayed type I isotherms without hysteresis, typical for microporous materials. These nitrogen physisorption curves are Gibbs excess adsorption isotherms, measured by default by the Micromeritics ASAP 2020 instrument as the standard for experimental measurements of amount adsorbed. Excess adsorption can be considered to be equal to absolute adsorption in the low pressure region, while problems

such as negative adsorption seen in the NaY/CA samples can occur in the high pressure region. However, as only values in the low pressure region are used to calculate BET surface area and micropore volume of these materials, the issue with the isotherm curves does not affect the accuracy of the calculated values of surface area and micropore volume. The adsorption community remains divided on the use of absolute versus Gibbs excess to measure and interpret the quantity of gas adsorbed by solids.[113]

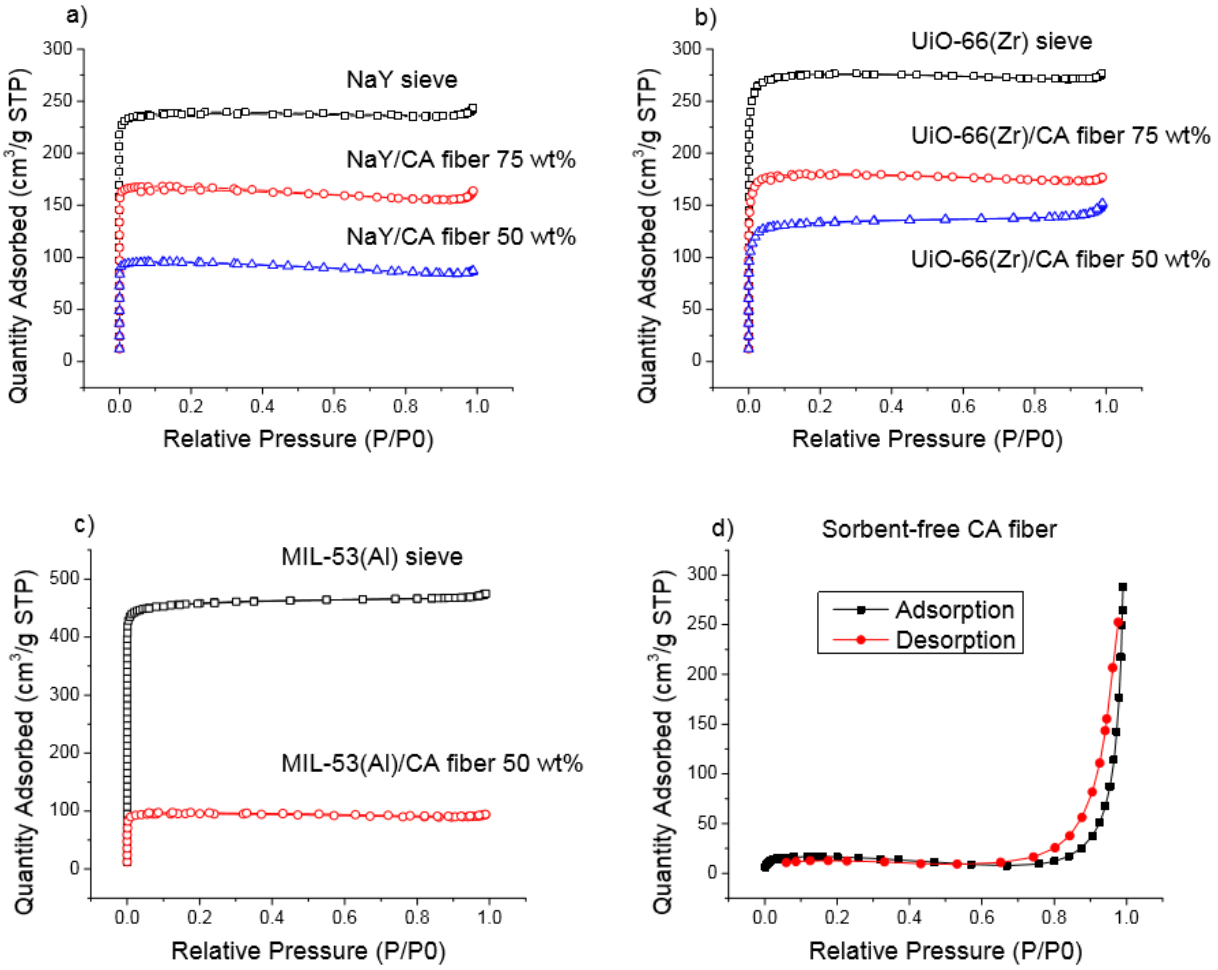

Figure 40: Nitrogen physisorption isotherms of chosen materials in original sieve form and after fiber spinning: (a) NaY, (b) UiO-66(Zr), (c) MIL-53(Al), and (d) a sorbent-free CA polymer fiber.

The surface area and micropore volume of these materials are summarized in Table 8 along with particle size range measured from SEM images. Both MOF and zeolite composite fiber sorbents experienced changes in the nitrogen isotherms corresponding to the weight percentages of microporous material loaded into spun fibers. This surface area difference between fibers and powders produced of the same material has been previously observed.[114]

Table 8: Textural properties of surface area and pore volume of adsorbent sieve materials and hybrid fibers

Sample	BET Surface Area (m^2/g)	t-plot Micropore Volume (cm^3/g)	Particle Size (μm)
NaY sieve	868	0.35	1-3
75 wt% NaY/CA fiber	598	0.26	
50 wt% NaY/CA fiber	339	0.15	
UiO-66(Zr) SB sieve	1002	0.40	1-4
UiO-66(Zr) LB sieve	1063	0.38	
75 wt% UiO-66(Zr)/CA fiber	652	0.26	
50 wt% UiO-66(Zr)/CA fiber	481	0.18	
MIL-53(Al) sieve	1329	0.54	1-4
50 wt% MIL-53(Al)/CA fiber	334	0.14	
Sorbent-free CA fiber	60	0.02	

5.1.4 XRD patterns of fiber sorbents

The XRD patterns of the parent NaY and UiO-66(Zr) sorbent materials are shown in Figure 41 alongside that of a sorbent-free CA polymer fiber and hybrid sorbent−polymer fibers of various loadings. The peaks of the hybrid fiber patterns are less

intense than those of the original sieve materials, but match the parents peak positions, giving evidence that the sieves were successfully integrated into the polymer fibers.

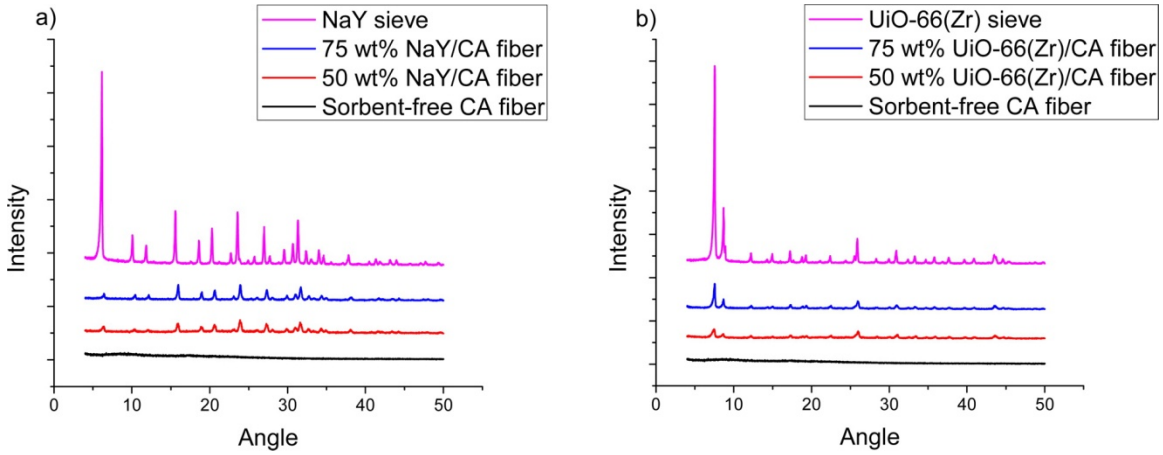

Figure 41: XRD patterns of the powder sorbent samples and hybrid polymer-sorbent fibers at various sorbent weight loadings: (a) NaY and (b) UiO-66(Zr).

5.1.5 TGA degradation curves of fiber sorbents

Thermal analysis (TGA) curves of hybrid NaY/CA and UiO-66(Zr)/CA fibers at various sorbent weight loadings are shown in Figure 42, plotted alongside the curves for the original microporous powders and a cellulose acetate fiber without sorbent. Again, this figure shows that there is little difference between UiO-66(Zr) synthesized using SB versus LB techniques. The weight percent of zeolite NaY loaded into NaY/CA hybrid fibers can be directly calculated based on their TGA curves due to the original sieve losing only solvent, such that any weight loss for the fibers after 300 °C can be attributed to the burning off of CA polymer alone. Target sorbent loading values for the NaY/CA

fibers were 50 and 75 wt % NaY, and the calculated weight percentages actually achieved from TGA curves were 49 and 76 wt %, respectively.

The TGA curves of UiO-66(Zr) show an initial weight loss from adsorbed water and solvents leaving the pores, followed by a much larger weight loss from the elimination of terephthalic acid molecules from the structure. The weight percent of UiO-66(Zr) loaded into the fibers can be estimated by using stoichiometry to back-calculate the amount of UiO-66(Zr) in each sample from the amount of ZrO_2 left as the final species at the end of the TGA experiment. The calculated sorbent loadings actually achieved for target loadings of 50 and 75 wt % were 53 and 72 wt %, respectively. Sample calculations detailing how these sorbent loading values were obtained from the raw data have been included in the Appendix. These results demonstrate the accuracy and reliability of the dope formation and fiber-spinning procedure for both NaY and UiO-66(Zr) fibers.

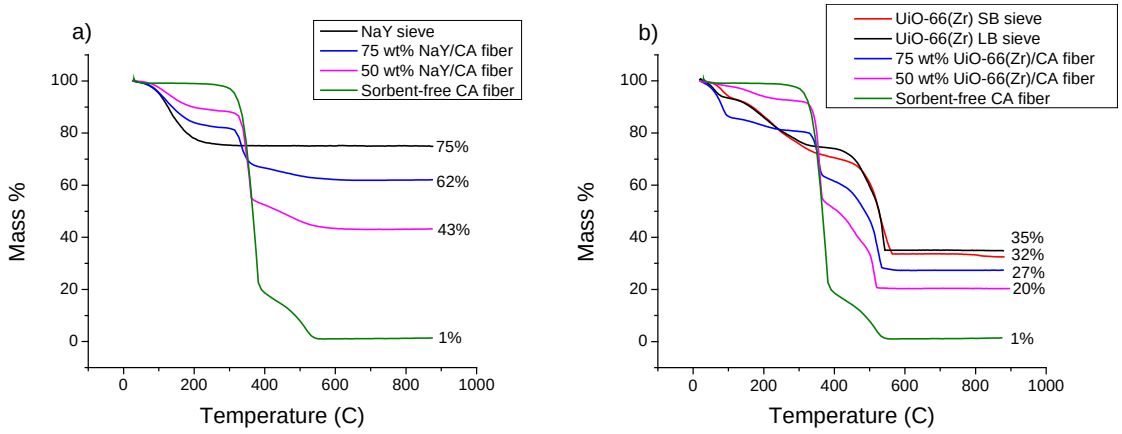

Figure 42: TGA curves of the powder sorbent samples and hybrid polymer-sorbent fibers at various sorbent weight loadings: (a) NaY and (b) UiO-66(Zr).

The elemental analysis (EA) results for NaY and UiO-66(Zr) sieves, pure CA polymer fiber, and various sorbent-loaded hybrid fibers are reported in Table 7 to verify the loading estimates obtained from TGA curves and confirm ZrO_2 as the species left at the end of the thermal analysis. Sample calculations of this verification have also been included in the Appendix.

5.2 Spinneret Fiber Spinning Parameters and Characteristics

After fiber sorbent dope compositions were optimized for both NaY/CA and UiO-66(Zr)/CA with syringe fiber tests, larger quantities (150−250 mL) of spin dope were made to be spun with the spinneret apparatus. For both NaY and UiO-66(Zr), 75 wt % sorbent loading was the highest easily achievable fiber. Higher sorbent loading dopes either were unable to be spun or produced brittle, fragile fibers. The fiber spinning apparatus located inside a walk-in fume hood is pictured in Figure 43.

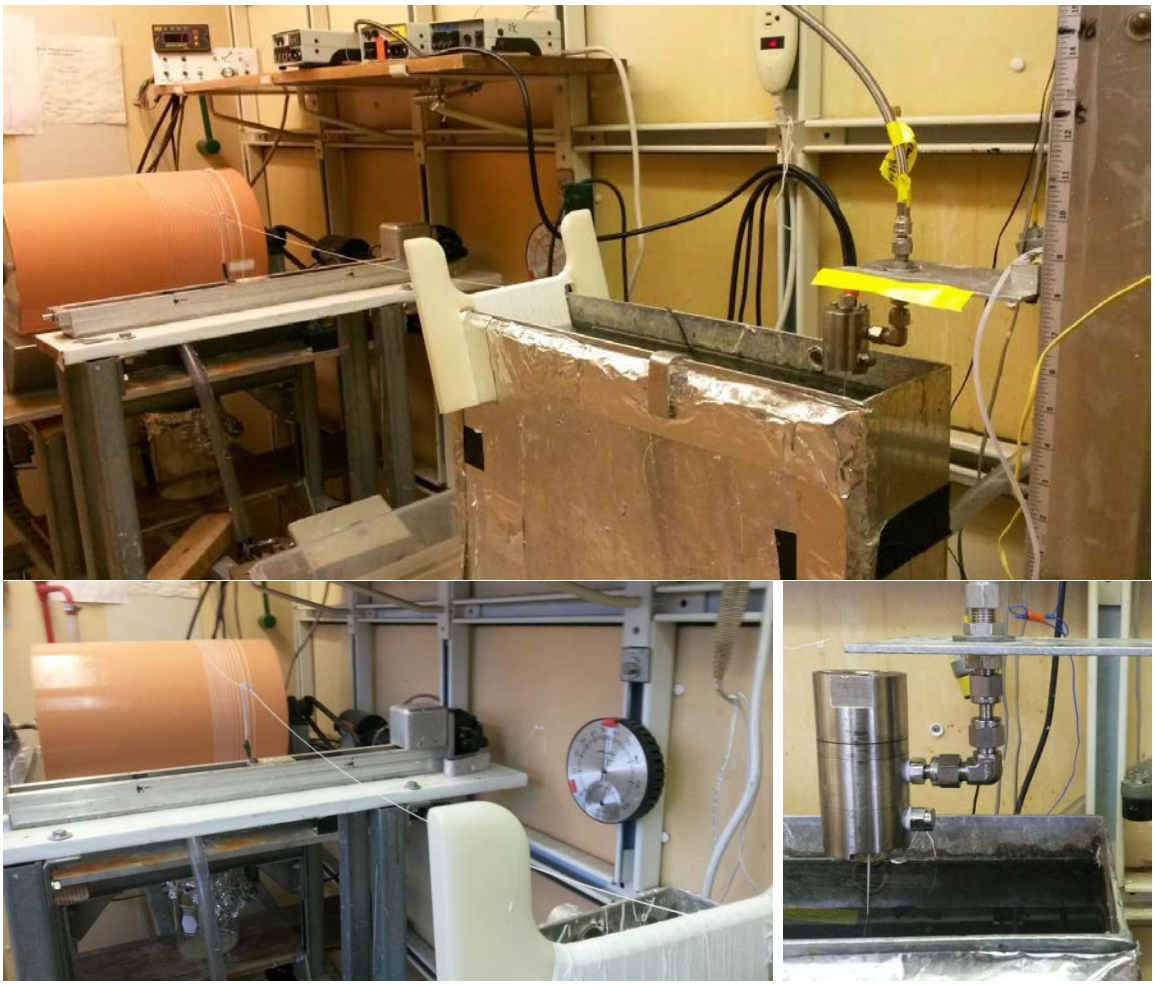

Figure 43: Photo of the fiber spinning apparatus in full (top) and with close-ups of the fiber uptake drum (bottom left) and spinneret extruding spin dope (bottom right).

First, 50 wt % NaY/CA spinneret fibers were created to ensure scalability of the optimized syringe fiber compositions. Once this was verified, the high sorbent loading 75 wt % NaY/ CA and 75 wt % UiO-66(Zr)/CA (dry fiber weight basis) fibers were spun. Table 9 summarizes the optimized final spin dope compositions for the high sorbent loading NaY/CA and UiO-66(Zr)/CA fibers as well as the optimized spinning apparatus parameters.

Table 9: Final fiber sorbent spin dope composition (left) and spinning parameters (right)

Spin dope component	NaY/CA dope (wt %)	UiO-66(Zr)/CA dope (wt %)	**Spinning parameter**	Range
NaY	18.9	n/a	Dope flow rate	100-700 mL/h
UiO-66(Zr)	n/a	22.4	Drum take-up rate	12 m/min
CA	6.3	7.5	Air gap	3 cm
PVP	5.0	6.0	Operating temperature	25 ºC
NMP	61.8	56.6	Quench bath temperature	40-55 ºC
H_2O	8.0	7.5		

5.2.1 Fiber sorbent dope flow rate correlation

The dope flow rate set by the syringe pump was varied between 100 and 700 mL/h to produce fibers of different diameters, as illustrated by the correlation shown in Figure 44. The optimal drum uptake rate to produce consistently shaped fibers with no breaks was found to be 12 m/min, and the air gap was set low at ~3 cm to yield fast phase separation to avoid formation of an external dense skin layer in the new fiber. The operating temperature was ambient temperature, ~25 °C, while the quench bath temperature ranged between 40 and 55 °C to allow faster phase separation.

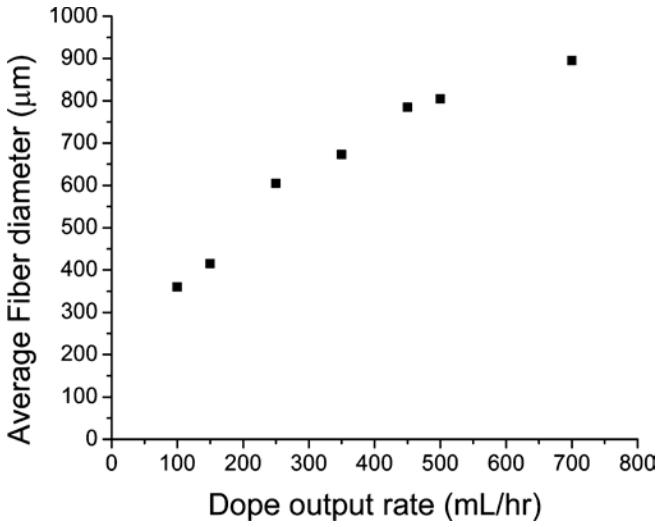

Figure 44: Linear correlation between dope output rate and average diameter of the fibers produced.

5.2.2 SEM images of fiber sorbents

SEM images of the cross sections of NaY/CA and UiO-66(Zr)/CA fibers are shown in Figure 45. Both sets of fibers were consistent in shape and had an open morphology, while displaying qualitatively good mechanical strength and flexibility.

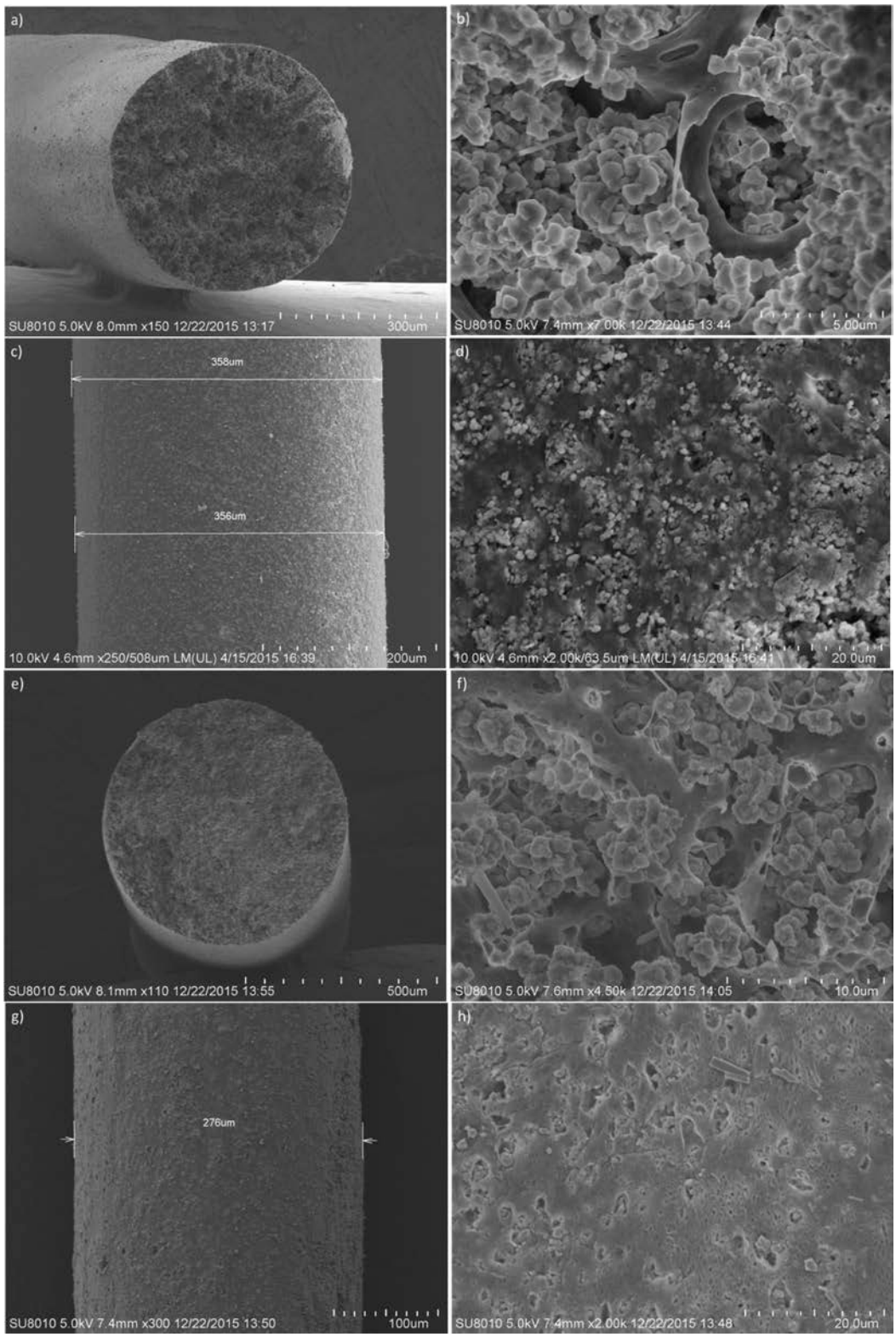

Figure 45: SEM images of 75 wt % loaded NaY/CA fiber sorbent (a) cross section, (b) close-up of cross section showing NaY crystal dispersion in CA fiber matrix, (c) external surface, (d) close-up of external surface showing surface porosity; and 75 wt % loaded UiO-66(Zr) fiber sorbent (e) cross section, (f) close-up of cross section showing UiO-66(Zr) crystal dispersion in CA fiber matrix, (g) external surface, (h) close-up of external surface showing surface porosity.

5.3 Equilibrium Adsorption Measurements

5.3.1 Syringe versus spinneret fiber TBM uptake capacity verification

The single cycle equilibrium adsorption capacities of the powder sorbent materials NaY, UiO-66(Zr), and MIL-53(Al) and their corresponding initial 50 wt % loaded syringe fibers toward the model natural gas (NG) are shown in Figure 46 on the left. All uptake values for the fiber sorbents have been normalized with respect to powder sorbent weight alone.

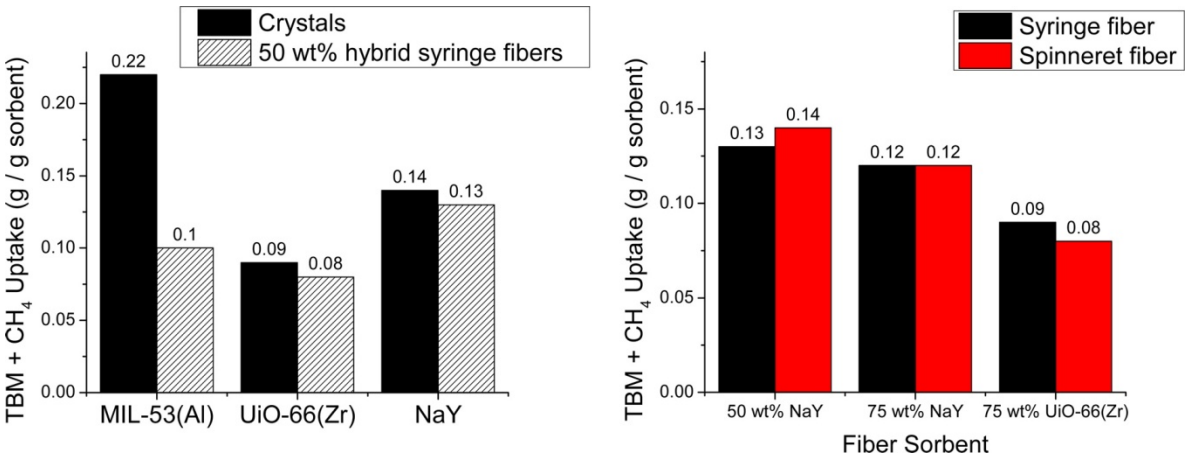

Figure 46: Equilibrium uptake values for model natural gas (60 ppm TBM/CH4) of (left) the powder samples and the uptake values of the 50 wt % sorbent-polymer hybrid syringe fibers and (right) various sorbent-loaded syringe fibers versus that of spinneret fibers, showing good agreement. All uptake values are normalized to per gram of sorbent.

Although MIL-53(Al) displayed the highest adsorption uptake of 0.22 g/g of sorbent for the model NG in its original crystalline form, it was only able to reach about half (0.10 g/g of sorbent) of this same value when spun into a fiber. This further supports the hypothesis that the cloudiness in the water bath during fiber synthesis and solvent

exchange was caused by dissolution or destruction of at least some of the MIL-53(Al). In contrast, both NaY and UiO-66(Zr) fibers were able to reach approximately the same uptake values as their original powders and were therefore further investigated and optimized. NaY crystals reached an uptake of 0.14 g/g of sorbent, while the 50 wt % NaY/CA syringe fiber reached an uptake of 0.13 g/ g of sorbent. UiO-66(Zr) crystals had an uptake of 0.09 g/g of sorbent, while the 50 wt % UiO-66(Zr)/CA syringe fibers gave an uptake of 0.081 g/g of sorbent. Both 50 wt % sorbent-loaded NaY and UiO-66(Zr) fibers were able to reach acceptable percentages of 94% and 87% of the uptake values achieved by their corresponding powders, respectively.

Upon spinning NaY and UiO-66(Zr) fibers with the spinneret assembly, syringe and spinneret fibers were compared against each other for consistency. As summarized in Figure 46 on the right, the 50 wt % NaY/CA syringe and spinneret fibers reached uptakes of 0.13 and 0.14 g/g of sorbent, respectively. Similarly, the 75 wt % NaY/CA syringe and spinneret fibers reached uptakes of 0.12 and 0.12 g/g of sorbent, respectively. The MOF fibers performed similarly, with the 75 wt % UiO-66(Zr)/CA syringe and spinneret fibers reaching uptakes of 0.09 and 0.08 g/g of sorbent, respectively. The syringe and spinneret fiber uptakes were found to be in good agreement in all cases, with <5% difference between them, being especially close for UiO-66(Zr) fibers. Taking the average uptake between the optimized syringe and spinneret fibers, the 75 wt % sorbent-loaded NaY and UiO-66(Zr) fibers again reached acceptable percentages of about 87% and 90% of their uptake values in powder form, respectively.

5.3.2 Cyclic regenerability of sorbent sieves at different desorption temperatures

The cyclic equilibrium adsorption capacities of NaY and UiO-66(Zr) LB and SB crystals toward the model NG at various desorption temperatures are shown in Figure 47. NaY showed little difference in uptake when using 200 and 300 °C desorption temperatures but decreased by an average of 26% for desorption at 120 °C. The standard deviations for the five cycles were 0.01, 0.02, and 0.01 g/g of sorbent for 300, 200, and 120 °C, respectively.

For all desorption temperatures and consistent with previous findings, NaY showed a slight decreasing trend in uptake in the first three cycles, followed by stabilization, likely due to some small amount of irreversible binding of sulfur species.[31] UiO-66(Zr) LB showed an average uptake decrease of 40% from a desorption temperature of 200 to 120 °C. However, for desorption at 120 °C, there was a slight increasing trend in uptake in the first three cycles followed by stabilization, which was not present in the uptake experiments using a desorption temperature of 200 °C, such that, by the fifth cycle, the decrease was only by 33%. A possible explanation is that the lower adsorption temperature was unable to fully desorb any previously adsorbed atmospheric gases or residual synthesis solvents in the desorption time used, but the repeated thermal cycling with continuous gas flow over the sample was able to help liberate these molecules over the later cycles. There appears to be no irreversible binding of sulfur species for UiO-66(Zr), consistent with previous findings detailed in chapter 3.[31]

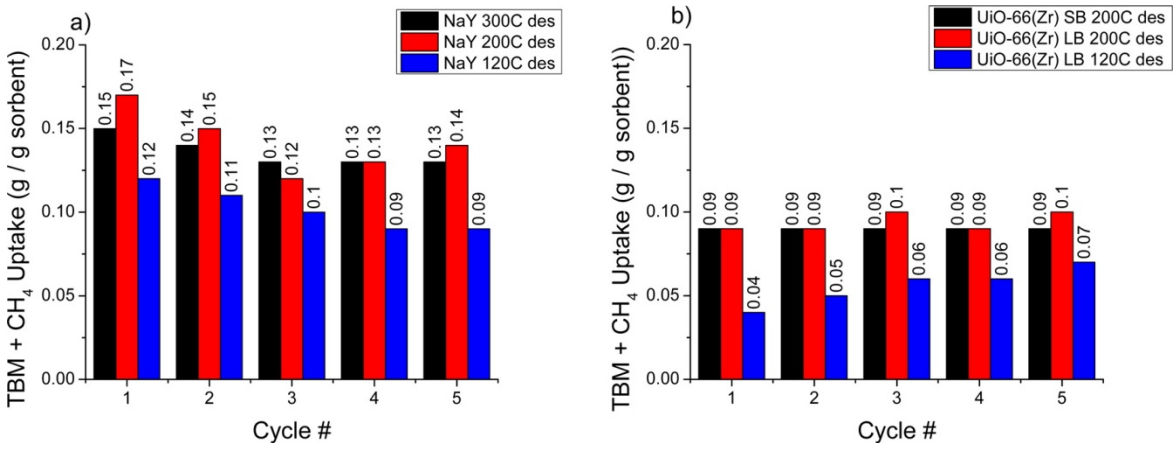

Figure 47: Cyclic equilibrium uptake values at 35 °C for model natural gas (60 ppm TBM/CH4) for (a) NaY sieve at desorption temperatures of 120, 200, and 300 °C and (b) UiO-66(Zr) LB sieve at desorption temperatures of 120 and 200 °C, with a comparison to UiO-66(Zr) SB sieve at 200 °C. All uptake values are normalized to per gram of sorbent.

The standard deviations for the five cycles were 0.001 and 0.008 g/g of sorbent for 200 and 120 °C, respectively. A thorough cost−benefit analysis needs to be completed to assess whether the energy savings gained by this lower-temperature desorption would offset the decrease in cyclic adsorption capacity. Additionally, consistent with the UiO-66(Zr) characterization results, there was no significant difference between the cyclic capacities of SB and LB.

5.3.3 Cyclic regenerability and selectivity of fiber sorbents

To estimate fiber selectivity and examine regenerability, the cyclic equilibrium adsorption capacities of 75 wt % sorbent loaded NaY/CA and UiO-66(Zr)/CA fibers toward model NG, methane-free TBM gas, and sulfur-free methane are shown in Figure 48.

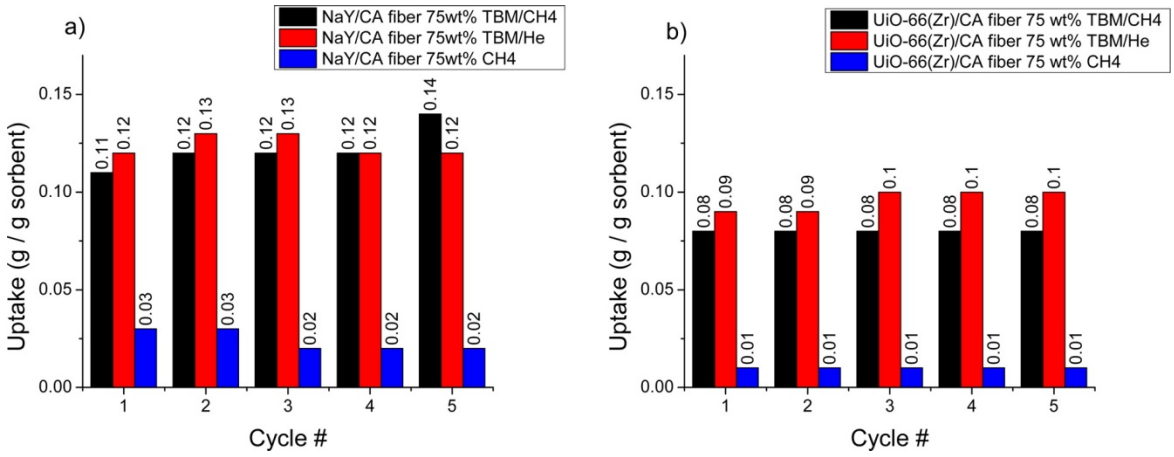

Figure 48: Cyclic equilibrium uptake values at 35 °C with 200 °C cyclic helium desorption sweep for (a) 75 wt % NaY/CA and (b) 75 wt % UiO-66(Zr)/CA hybrid fibers for model natural gas (60 ppm TBM/CH4), methane-free TBM gas (60 ppm TBM/He), and sulfur-free methane gas (99.0% methane purity). All uptake values are normalized to per gram of sorbent.

NaY/CA fibers did not show any observable trends in cyclic uptake toward model NG or methane-free TBM gas; however, they did show the familiar trend of slightly decreasing uptakes for the first three cycles followed by stabilization, using the sulfur-free methane gas. NaY/CA fibers had average sorption values of 0.12, 0.13, and 0.02 g/g of sorbent with standard deviations of 0.01, 0.006, and 0.008 g/g of sorbent for model NG, methane-free TBM gas, and sulfur-free methane, respectively. UiO-66(Zr)/CA fibers showed a more stable, although lower overall, trend in uptake, with average sorption values of 0.09, 0.09, and 0.01 g/g of sorbent and standard deviations of 0.001, 0.004, and 0.001 g/g of sorbent for model NG, methane-free TBM gas, and sulfur-free methane, respectively. Both types of fiber sorbents showed a slightly higher uptake for methane-free TBM gas than the model NG, potentially due to the lack of competitive adsorption or hindrances of various other impurity gas species in the sulfur-free methane, which is inconsistent with the previous findings for NaY in its powder form.[31]

The average amounts of sulfur-free methane adsorbed by NaY/CA fibers and UiO-66(Zr)/CA fibers as percentages of the amounts of model NG adsorbed were 20% and 15%, respectively. These equilibrium values of sulfur-free methane represent the maximum amount of methane and/or other impurities that could be competitively adsorbed over TBM in the fibers. Overall, the capacity of NaY/CA fibers for model NG is ~29% higher than UiO-66(Zr)/CA fibers, although NaY/CA has a larger margin of error (higher standard deviation) in uptake capacity due to its extreme hydrophilicity, making it more sensitive to even small changes in the ambient laboratory environment. Being more hydrophobic, UiO-66(Zr) is more stable toward these changes.

These results further indicate that NaY and UiO-66(Zr) are good candidates for mercaptan removal via the fiber sorbent system. Both sorbent materials are resilient towards the fiber spinning process and cyclic regeneration, maintaining the same high TBM capacities and regenerability in their fiber forms as in their sieve forms. With these encouraging outcomes, the performances of NaY/CA and UiO-66(Zr)/CA fiber sorbents were further evaluated in a modular form in a temperature swing adsorption flow system in the third and final objective, discussed in the next chapter. Before the publication of the work discussed in this chapter, no literature had been found on the formation of UiO-66(Zr)/CA hybrid fibers. This work showed that not only is their fabrication easily achievable without any modifications to the typical fiber spinning process, but that they can retain nearly unchanged sorption performance per gram of UiO-66(Zr).

CHAPTER 6

SORPTION PERFORMANCE OF FIBER SORBENT MODULES IN A TEMPERATURE SWING ADSORPTION SYSTEM

The work described in chapters 3 and 4 indicated that the zeolite NaY and MOF UiO-66(Zr) were good candidate materials for incorporation into hybrid polymer-adsorbent fibers in a temperature swing adsorption system for mercaptan odorant removal from pipeline natural gas.[115] The hybrid fiber sorbents consist of a matrix of cellulose acetate and sorbent crystals spun using the spinning apparatus and technique described in the previous chapter. The fibers demonstrated great stability throughout the various steps of a mechanically and chemically rigorous fiber spinning process, with the sieves retaining their crystallinity and adsorption properties within the final fiber. Alone, NaY and UiO-66(Zr) sieves displayed high mercaptan capacities, stabilities, regenerabilities, and selectivities, which made these sorbents ideal for the envisioned final adsorptive odorant removal system with fiber modules.[31] Actual sorbent weight loadings of 76 wt% and 72 wt% were achieved for NaY and UiO-66(Zr) respectively. The average particle size of NaY is 2 μm and of UiO-66(Zr) is 2.5 μm as measured by SEM images. Fibers of approximately 700 μm in diameter with densities of 0.0013 g/cm for NaY/CA fibers and 0.0012 g/cm for UiO-66(Zr)/CA fibers were chosen for implementation in the module TSA system.

In the work discussed in this chapter, both NaY/CA and UiO-66(Zr)/CA hybrid fibers were packaged into modules for adsorption experiments in the TSA system as a proof-of-concept for practical industrial application. The results of this study provide a

demonstration of how this fiber sorbent module system can be feasibly implemented in a natural gas fueled power plant, and insight into the roles of different system variables and potential challenges still to be addressed in the overall system.

6.1 Equilibrium and Breakthrough Adsorption Measurements

6.1.1 Fiber sorbent module creation

Fiber sorbent modules were created using ¼ inch diameter stainless steel Swagelok tubing and fittings as shown in the photo in Figure 49. Three fibers were sealed in each 8 inch module using epoxy, corresponding to a calculated module void fraction of 0.68 (example calculations for this value are discussed in the Appendix).

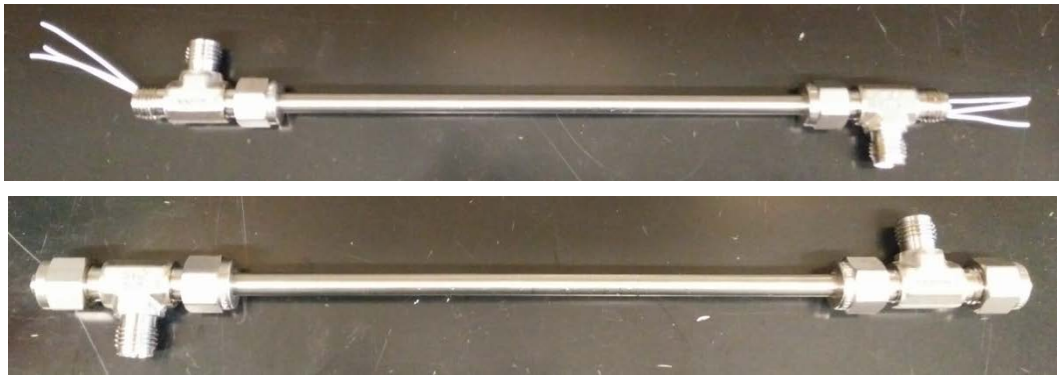

Figure 49: Photos of 8 inch long fiber sorbent modules constructed with ¼ inch diameter Swagelok tubing and fittings, showing bundling of fibers inside the tubing before (top) and after (bottom) fittings are attached.

The fiber sorbent module was then connected to the TSA system in a vertical position with gas inlet at the top and gas outlet at the bottom such that gas flows downward. The system was used to evaluate dynamic TBM adsorption performance and

cycling ability of the fiber sorbents in a model natural gas flow. The gas temperatures at the inlet and outlet of the module were monitored using T-type thermocouples throughout the experiment, and the gas composition exiting the module was measured every 1 second by mass spectrometry (Pfeiffer, Omnistar Quadrupole mass spectrometer QMG 220). The inlet and outlet gas pressures were measured with pressure transducers (MKS, Inc.) and both model natural gas and purge gas (helium) flow rates were controlled with mass flow controllers (Brooks Instrument, SLA 5850). A custom program written in Labview (National Instruments) was used to automatically monitor and record temperature, pressure, and flow rate data, as well as control the overall operation of the TSA system.

Unfortunately, both MOF and zeolites fiber modules in the original TSA system experimental setup (pictured in Figure 63(a) in the Appendix) experienced difficulty with regeneration after the first TBM adsorption step, a challenge that was not present with adsorption in the TGA. It was discovered that this was because of insufficient heating of the fibers through the stainless steel walls of the module casing due to inadequate time for heat exchange from the heating tape to the stainless steel tubing and also heat loss through several feet of unwrapped tubing inside of the TSA system process control box. The helium desorption gas was therefore unable to reach the high desorption temperature requirement of the fibers in the original TSA setup. To fix this problem, a slightly modified setup (pictured in Figure 63(b) in the Appendix) involving coiling 1/8'' stainless steel tubing in an oil heating bath placed within the TSA system box before the inlet of the fiber module was used for all adsorption experiments reported in this section. The new setup was able to reach the temperature necessary to perform desorption and

cycle the fibers after TBM adsorption. The discovery of this problem is discussed more in Section 5.2 in the portion on elemental analysis results. A more thorough discussion of this issue and its resolution and an illustration of the new TSA system setup is included in the Appendix along with other challenges faced in this project overall.

6.1.2 TBM capacity calculations from TSA breakthrough curves

All experiments were performed at atmospheric pressure with varied operating conditions. Before each adsorption experiment, the fiber module was purged with flowing helium at 80 sccm at 200°C for 1 hour to desorb previously adsorbed gases. The module was then cooled down to the adsorption temperature, which was varied between 35, 45, and 55 ºC with the model natural gas flow rate fixed at 40 sccm to characterize the effect of temperature on adsorption capacity. In a second set of experiments, the adsorption temperature was then fixed at 35 ºC while the model natural gas flow rate was varied between 10, 20, 40, and 80 sccm, corresponding to interstitial velocities of 7.8, 15.5, 31.1, and 62.1 cm/s respectively to characterize the effect of flow rate on adsorption capacity. With a module containing 3 fibers, the packing fraction was at a low 0.32, and the pressure data recorded by the transducers before and after the module show that the pressure drop across the module was negligible and remained at atmospheric pressure throughout all experiments. This is consistent with the predictions from previous calculations showing a pressure drop of nearly zero for these types of fiber modules, especially at larger fiber diameters and lower gas flow rates.[12]

Figure 50 shows a typical TBM breakthrough curve of a NaY / CA fiber module and a UiO-66(Zr) / CA fiber module, with feed flow rate set at 40 sccm and an adsorption temperature of 35 °C, with the methane carrier gas as a reference. Curve smoothing of the raw data was done in Origin using the Smooth tool to remove noise from the TBM signal. As the feed gas is switched from pure helium to the model natural gas, the helium concentration drops to zero as methane breaks through, followed by TBM breakthrough several hours later when the module reaches its adsorption capacity. The TBM adsorption step is long due to the low concentration of TBM in the model natural gas. The breakthrough of methane (present at 99.0% purity in the model natural gas, as mentioned in previous chapters) as a non-adsorbing gas provided background information about the flow behavior of the bulk gas through the module as the feed is switched from the helium purge to model natural gas.

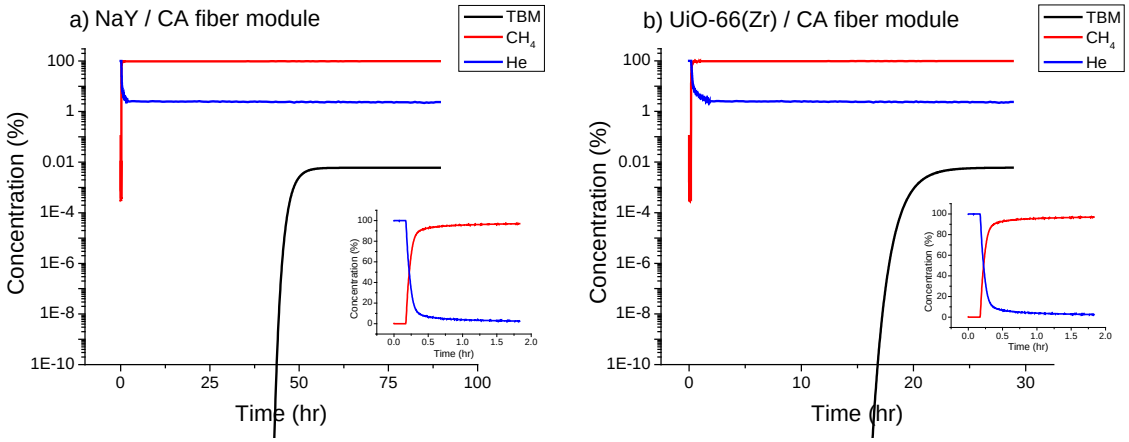

Figure 50: Typical breakthrough curves of a) NaY/CA fiber module and b) UiO-66(Zr)/CA fiber module. Both modules contained 3 fibers each and were operated with a model natural gas flow rate of 40 sccm and an adsorption temperature of 35°C. Inset graphs zoom in on a linear scale on the first two hours of the transition from desorption step with helium purge to adsorption step with methane as the bulk carrier gas.

The breakthrough and equilibrium capacities were calculated by integrating the area between the TBM breakthrough signal and its equilibrium value of 60 ppm with respect to time. All uptake values reported in this section are normalized by the amount of sorbent in the fiber module. The methane breakthrough time is taken as the time at which the TBM begins to be adsorbed in the module and was used as the starting time point for integration of the TBM curve. The TBM breakthrough capacity was calculated by integrating from the methane breakthrough time to the time point at which TBM begins to appear in the exit gas at a concentration of 3 ppm (5% of the equilibrium concentration), while the equilibrium capacity was calculated by integrating to the time point at which TBM reached its equilibrium value. The breakthrough and equilibrium time changed significantly with different operating conditions, as will be discussed later. Example TSA capacity calculations are shown in the Appendix. The breakthrough capacity is an important factor for consideration in a practical application, as the feed gas would typically be switched over to purge at this point for regeneration, such that natural gas exiting the module would always be free of TBM. The equilibrium and breakthrough uptake values for NaY / CA fibers under the conditions in Figure 50 were 0.129 ± 0.006 and 0.120 ± 0.005 g/g sorbent, respectively; and for UiO-66(Zr)/CA fibers were 0.064 ± 0.005 and 0.057 ± 0.004 g/g sorbent, respectively.

6.1.3 Length of unused bed

The fractional length of unused bed (LUB) is a key design parameter for scale up of an adsorber bed. The LUB is the length of the fiber sorbent module that is left over and "unused" at the time of TBM breakthrough, after the rest of the module has been fully

saturated. The shape of the TBM breakthrough curve determines how much the full capacity of the fiber module can be utilized during adsorption, and consequently, the length of module needed to adsorb a certain amount of TBM. For scale up, the LUB is added to the required length of bed for a certain breakthrough time to achieve the desired TBM adsorption capacity. The LUB can be calculated with the following equation:

$$LUB = \left(1 - \frac{t'}{\bar{t}}\right) L \tag{20}$$

where t' is the actual (experimental) breakthrough time, $\bar{t}$ is the theoretical (ideal) breakthrough time with a perfectly sharp front, and L is the length of the module. For the modules and conditions shown in Figure 50, the fractional LUB was 0.24 and 0.32 for NaY / CA and UiO-66(Zr) / CA fiber modules respectively.

6.1.4 Adsorption measurements at various feed flow rates

Figure 50 illustrates the TBM breakthrough curves of NaY / CA and UiO-66(Zr) / CA fiber modules (containing 3 fibers each) at various feed flow rates between 10 and 80 sccm at a fixed adsorption temperature of 35°C. As can be seen in the figure, TBM broke through faster as the flow rate of the model natural gas feed was increased. The front also sharpened with increased feed flow rate due to reduced external mass transfer resistance and faster adsorption rates with higher external flow rates.

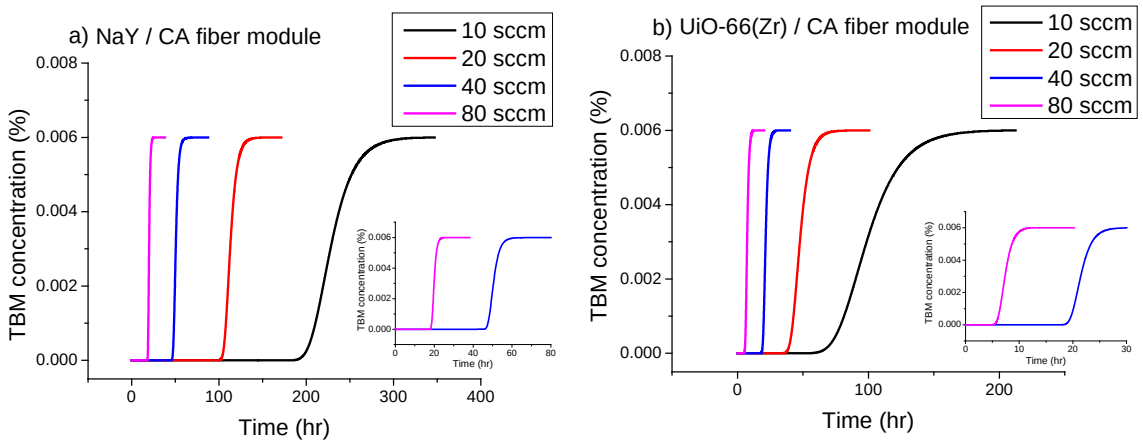

Figure 51: TBM breakthrough curves of a) NaY/CA fiber module and b) UiO-66(Zr)/CA fiber module at various model natural gas flow rates of 10, 20, 40, and 80 sccm. Inset graph zooms in on 40 and 80 sccm breakthrough curves alone.

Figure 52 shows the comparison in fiber sorbent performance at different flow rates. As flow rate increased, breakthrough and equilibrium capacities decreased. Adsorption experiments were not repeated for the 10 sccm flow condition due to the extended amount of time it took to reach equilibrium with this very slow flow rate. The breakthrough and equilibrium uptake for the NaY / CA module reduced from 0.131 and 0.149 g/g sorbent, respectively, at a flow rate of 10 sccm to 0.096 ± 0.007 and 0.101 ± 0.008 g/g sorbent, respectively, at 80 sccm. This corresponds to a 27% decrease in breakthrough capacity and a 32% decrease in equilibrium capacity. Similarly, the breakthrough and equilibrium uptake for the UiO-66(Zr) / CA module reduced from 0.059 and 0.078 g/g sorbent, respectively, at a flow rate of 10 sccm to 0.038 ± 0.005 and 0.046 g/g ± 0.005 sorbent, respectively, at 80 sccm. This corresponds to a 35% decrease in breakthrough capacity and a 41% decrease in equilibrium capacity. A likely explanation of this trend is that external mass transfer resistance and gas contact time decreased with increased flow rate, resulting in the sharper breakthrough fronts seen in Figure 51, and a reduction in TBM uptake capacity at higher flow rates.

6.1.5 Comparison of TBM adsorption capacity in TSA system versus TGA

The equilibrium adsorption results obtained in the TSA system at 10 and 20 sccm flow rates were very similar to the results obtained in the TGA, as discussed in Chapter 4. There is a decreasing deviation away from TGA performance values as the feed flow rate was increased in the TSA system. Different flow rates and adsorption temperatures were not studied in the TGA as they were in this portion of work. More than one year passed between the formation and initial testing of NaY / CA and UiO-66(Zr) / CA hybrid fibers in the TGA discussed in Chapter 4 and the testing of these fibers in the TSA system discussed in this chapter. The fibers were stored in the laboratory in a sealed container at room temperature under an atmosphere of air during this time. To study if there were any long-term aging effects in these fibers as a result of this storage, the fibers were again tested for TBM adsorption capacity from model natural gas under the same conditions and setup in the TGA as shown in Figure 22. The NaY / CA fibers achieved a TBM uptake of 0.134 g/g sorbent and the UiO-66(Zr) / CA fibers achieved an uptake of 0.082 g/g sorbent. These results are not significantly different than the TBM uptake capacities measured initially in the TGA when the fibers were first formed, indicating that these fibers do not degrade or age in any way when stored under ambient environmental conditions. The stability of these fibers towards not only repeated cycles of TBM adsorption and desorption, but also long term atmospheric storage is promising for future implementation in a real commercial system, which would need to operate consistently long term over several years to be economically beneficial.

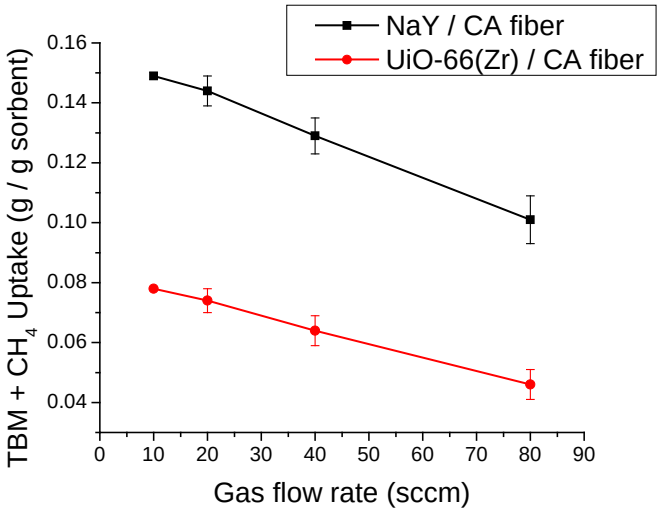

Figure 52: Equilibrium uptake values for model natural gas (60 ppm TBM/CH_4) at various flow rates. Both NaY / CA and UiO-66(Zr) / CA modules contained 3 fibers each and were operated at a fixed adsorption temperature of 35°C. All uptake values are normalized to per gram of sorbent.

6.1.6 Mass transfer coefficients of fiber sorbents

The feed flow rates of 10, 20, 40, and 80 sccm correspond to residence times inside the fiber module of 2.18, 1.10, 0.55, and 0.27 seconds, respectively. The temperature-dependent molecular diffusivity of TBM and methane ($D_{TBM\text{-}CH4}$), which is an important parameter for estimating the external mass transfer coefficient (MTC), was estimated to be approximately 0.072, 0.076, and 0.080 cm^2/s for adsorption temperatures of 35, 45, and 55°C respectively. The external MTC is dependent on both adsorption temperature and feed flow rate. At a fixed adsorption temperature of 35°C, the external MTC was calculated to be 0.476, 0.598, 0.752, and 0.945 cm/s for feed flow rates of 10, 20, 40, and 80 sccm respectively. At a fixed flow rate of 40 sccm, the external MTC was calculated to be 0.752, 0.785, and 0.818 cm/s for adsorption temperatures from 35-55°C.

It is clear that the external MTC is more dependent on the gas flow rate than adsorption temperature in these experiments.

From the mean free path calculations for both TBM and methane molecules (shown in the Appendix), it was determined that the $D_{TBM\text{-}CH4}$ molecular diffusivity was the controlling factor for internal mass transfer within the pores of the fiber, and Knudsen diffusion negligible. However, the effective diffusion coefficient (D_{eff}) inside the fiber would still be lower than the molecular diffusivity due to gas molecule transport being hindered by the polymer network and embedded sorbent crystals. As described in the Appendix, the D_{eff} inside the fiber pores was estimated to be approximately 0.008-0.009 cm^2/s, depending on the adsorption temperature range from 35-55°C. The internal MTC is only dependent on temperature, and was calculated to be 0.919, 0.964, and 1.010 cm/s for adsorption temperatures of 35, 45, and 55°C respectively.

From the magnitude of the MTCs, it can be seen that both the external and internal mass transfer contribute to controlling the gas transport resistance in the fiber module system; however the external MTC is generally smaller than the internal MTC (except for the case of 80 sccm flow rate and 35°C adsorption temperature, where the external MTC is slightly larger) and would therefore be the controlling resistance under the operating conditions used in this system. Example calculations of these diffusion coefficients and mass transfer coefficients are detailed in the Appendix.

Compared to the first cycle uptake values for the powder sieves alone in the TGA (0.09 g TBM / g UiO-66(Zr) and 0.17 g TBM / g NaY), the capacities of the hybrid fibers at 40 sccm and 35°C adsorption temperature achieved 71% of its maximum capacity for UiO-66(Zr)/CA and 75% of its maximum capacity for NaY/CA. The mass transfer

resistances present in the TSA flow system contributes to this decrease away from the maximum (theoretical) TBM capacity in the fibers. A possible explanation for the external mass transfer being the controlling resistance is the formation of a skin layer in the fiber sorbents. As seen in Figure 45, the inside (cross-section) of the fibers show good porosity and sorbent distribution, however the outside surface of the fibers are less porous and likely contributes to the mass transfer resistance leading to a decrease in TBM capacity in both UiO-66(Zr) and NaY hybrid fibers. To address this problem, the air gap in the spinning system can be decreased for future spins to decrease the skin layer that forms when solvent evaporates from the outer surface of the fiber as it goes through the air during its formation.

6.1.7 Adsorption measurements at various adsorption temperatures

Figure 53 presents the equilibrium and breakthrough capacities of NaY / CA and UiO-66(Zr) / CA fibers as a function of adsorption temperature at a fixed natural gas flow rate of 40 sccm. The same pretreatment conditions mentioned previously were used for all experiments. The TBM uptake capacity decreases with increasing adsorption temperature. The breakthrough and equilibrium uptake for the NaY / CA module reduced from 0.121 and 0.129 g/g sorbent, respectively, at an adsorption temperature of 35°C to 0.080 and 0.091 g/g sorbent, respectively, at 55°C. This corresponds to a 34% decrease in breakthrough capacity and a 29% decrease in equilibrium capacity. Similarly, the breakthrough and equilibrium uptake for the UiO-66(Zr) / CA module reduced from 0.055 and 0.064 g/g sorbent, respectively, at an adsorption temperature of 35°C to 0.034

and 0.044 g/g sorbent, respectively, at 55°C. This corresponds to a 38% decrease in breakthrough capacity and a 31% decrease in equilibrium capacity. The general trends of these results are consistent with the thermodynamic properties of adsorption.

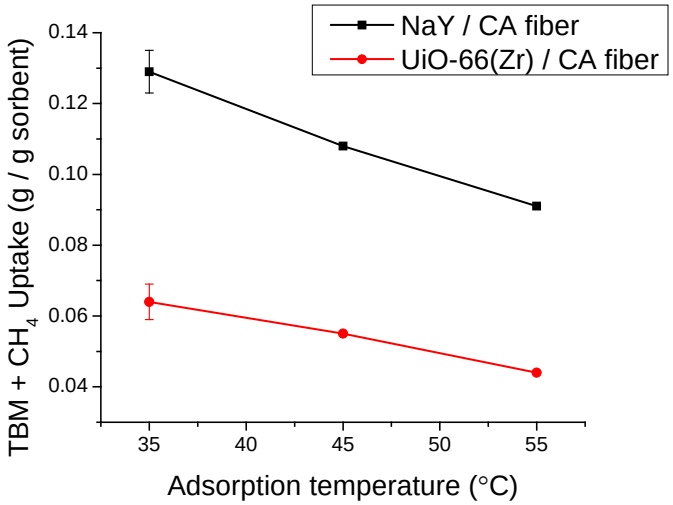

Figure 53: Equilibrium uptake values for model natural gas (60 ppm TBM/CH_4) at various adsorption temperatures. Both NaY / CA and UiO-66(Zr) / CA modules contained 3 fibers each and were operated at a fixed flow rate of 40 sccm. All uptake values are normalized to per gram of sorbent.

During adsorption, the temperature of the gas at the outlet of the module never differed by more than 1°C from the gas at the inlet of the module, indicating near isothermal operation during this step due to the ultralow concentration of sulfur to be adsorbed from the model natural gas feed. This result confirms previous calculations from the MS thesis work indicating near isothermal operation for this step without the need for cooling water to take the heat of adsorption, and supports the use of solid fibers without a bore for this application.[12]

6.1.8 Heat of adsorption of TBM on fiber sorbents

The heat of adsorption, ΔH_{ads}, is an important thermodynamic property defining how much heat is evolved during the adsorption of gases like TBM on solid surfaces such as that of zeolites and MOFs. It is useful for understanding any thermal effects that may occur during adsorptive removal of TBM, which can aid in heat management in scale-up of the system for practical applications, as well as the development of adsorption models. The heat of adsorption can be estimated using the Van't Hoff equation below, which relates the change in equilibrium adsorption capacity with change in adsorption temperature:

$$\frac{d \ln q_{eq}}{dT} = \frac{\Delta H_{ads}}{RT^2} \tag{21}$$

where q_{eq} (mol/cm^3) is the equilibrium adsorption capacity, T is absolute adsorption temperature, and R is the ideal gas constant. The ΔH_{ads} typically varies with temperature for most adsorption processes, but a good approximation of ΔH_{ads} can be obtained by assuming it is constant and integrating the Van't Hoff equation between two adsorption temperatures as follows:

$$ln\left(\frac{q_{eq,2}}{q_{eq,1}}\right) = -\frac{\Delta H_{ads}}{R}\left(\frac{1}{T_2} - \frac{1}{T_1}\right) \tag{22}$$

where $q_{eq,1}$ is the equilibrium adsorption capacity at adsorption temperature T_1 and $q_{eq,2}$ is the equilibrium adsorption capacity at adsorption temperature T_2.

Using the data shown in Figure 53 and integrating between 35°C and 55°C for both zeolite and MOF hybrid fibers, the estimated heat of adsorption of TBM on NaY/CA fibers is about -14.7 kJ/mol and on UiO-66(Zr)/CA fibers is -15.7 kJ/mol. These values are within the same magnitude, but slightly less than the heat of vaporization (condensation) of TBM and the heats of adsorption reported in other published works for mercaptans on similar zeolites and MOFs in their original crystalline form without a support. For example, Weber et al.[45] reported a heat of adsorption of approximately -37.5 kJ/mol for ethyl mercaptan on zeolite NaX, while Taheri et al.[109] reported a value of approximately -26.0 kJ/mol for methyl mercaptan on MOF MIL-53(Al). It is not unexpected that the hybrid fibers created in this work have lower ΔH_{ads} values than that of the original unsupported sieves due to the fibers having a lower adsorbent content (approximately 75 wt.% sorbent). However, these ΔH_{ads} values calculated for the hybrid fibers are lower than 75% of the literature values for zeolite and MOF sieves alone. A possible explanation for this discrepancy comes from the practical realities of potentially incompletely pretreated or desorbed fibers due thermal cycling at a lower temperature than the optimal desorption temperature of 200°C in the TSA system. This issue is discussed in more detail in the Appendix.

From the Handbook of the Thermodynamics of Organic Compounds, the enthalpy of vaporization of TBM at 35°C is -30.9 kJ/mol.[116] The heats of adsorption of TBM on the original zeolite or MOF sieves reported in the literature being close to that of its heat of vaporization indicates that physical adsorption of TBM on the solid surfaces of these adsorbents is the dominating mechanism, and is achieved by the same intermolecular

forces as vapor condensation. This supports the observation that adsorption equilibrium is reached relatively quickly and is mostly reversible in these sorbents.

6.1.9 Cyclic adsorption measurements and fiber regenerability

Finally, the cyclic performance of the fiber sorbent modules was investigated under fixed operating conditions of 40 sccm model natural gas flow and 35°C adsorption temperature. Again, the pretreatment and desorption conditions were kept the same as previous experiments. Cyclic regenerability is economically important for practical industrial applications. Figure 54 shows the uptake of these modules over five consecutive adsorption / desorption cycles. As mentioned previously, the initial equilibrium capacity was 0.129 g/g sorbent for NaY / CA fiber modules. This capacity decreases over the first three cycles to 0.104 g/g sorbent, corresponding to a 19% decrease from its initial capacity. This pattern of initial decrease followed by stabilization in TBM capacity was also observed in experiments with cycling the original NaY sieve (results discussed in Chapter 3) and the NaY / CA chopped fibers in the TGA (results discussed in Chapter 4), and was attributed to some small amount of irreversible binding and / or incomplete regeneration of adsorbed gases such as mercaptan, water, and / or CO_2. In all three cases, in order to keep the experiment time reasonable, the temperature and desorption step time was kept the same for all cycles and materials without regard to whether sulfur and other adsorbed gases had been fully desorbed in that time. This potentially incomplete regeneration may explain the initial capacity decrease as the desorption step releases a fraction of the total amount of gas adsorbed, which is then

followed by stabilization as the desorption step can now fully desorb that same fraction of gas repeatedly. The majority of the gas adsorbed in the initial step is still able to be desorbed once the desorption step reaches this achievable limit, and the capacity difference between the third and fifth cycle is nearly zero. Similar to previous TBM adsorption with NaY sieve and NaY / CA fibers in the TGA, the NaY / CA fibers used in these TSA experiments were slightly discolored (from white initially to light grey) after use.

For UiO-66(Zr) / CA fiber modules, the initial equilibrium capacity was 0.064 g/g sorbent, which remained very stable over all five cycles. The uptake capacity remained nearly unchanged between the first and fifth adsorption cycle. This trend is similar to previous TBM adsorption results on UiO-66(Zr) sieve and UiO-66(Zr) / CA fibers in the TGA. While NaY has a higher capacity for TBM overall, UiO-66(Zr) shows exceptional stability and predictability, with results never differing much from the initial cycle.

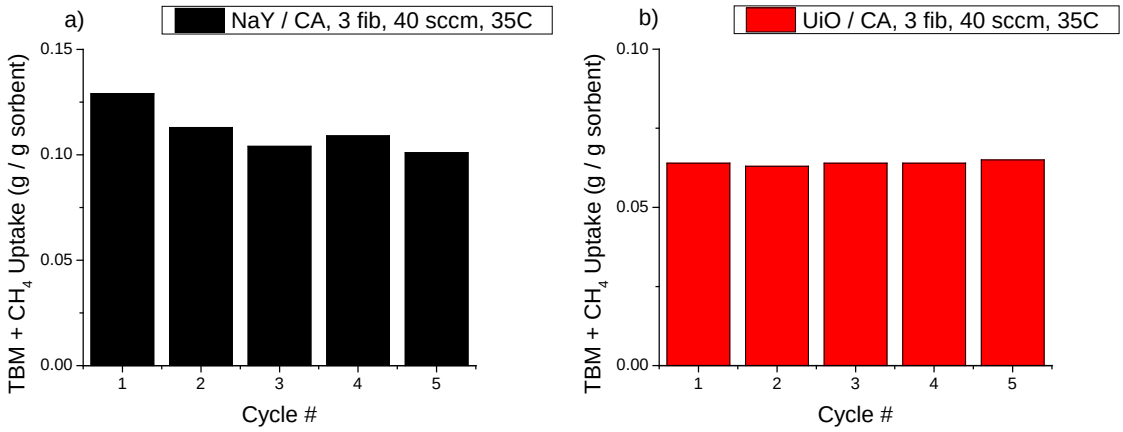

Figure 54: Cyclic equilibrium uptake values at 35°C and 40 sccm for model natural gas for (a) NaY / CA and (b) UiO-66(Zr) / CA fiber modules. All uptake values are normalized to per gram of sorbent.

For both NaY / CA and UiO-66(Zr) fiber modules, the desorption temperature of 200°C is significantly lower than the temperature at which pure cellulose acetate fibers break down (300°C), as shown in Figure 42. Additionally, both NaY and UiO-66(Zr) sieves are also stable above 300°C. Therefore, TBM capacity in the fibers is unlikely to be lost due to any structural damage to either fiber or sorbent. These cycling experiments in the TSA system show that both types of fiber sorbents are promisingly regenerable and stable over many cycles, which is important for implementation in an industrial application.

6.2 Characterizations of Materials

Fiber sorbents were characterized after exposure to the five cycles of TBM adsorption and desorption from the fixed conditions cyclic experiments shown in Figure 54, with the exception of elemental analysis results which will be discussed later. The fiber characteristics after TBM exposure were compared with that of fresh fibers to examine if any significant degradation or other changes occurred.

6.2.1 XRD patterns of fiber sorbents before and after TBM adsorption

The XRD patterns of 75 wt% sorbent loaded NaY / CA and UiO-66(Zr) / CA hybrid fiber sorbents before and after TBM adsorption are shown in Figure 55. The peaks of the “used" fibers of both MOF and zeolites are slightly less intense than those of the fresh fibers, but match the peak positions, giving evidence that the sieves retain their

crystallinity and remain integrated in the fibers even after many cycles of TBM adsorption.

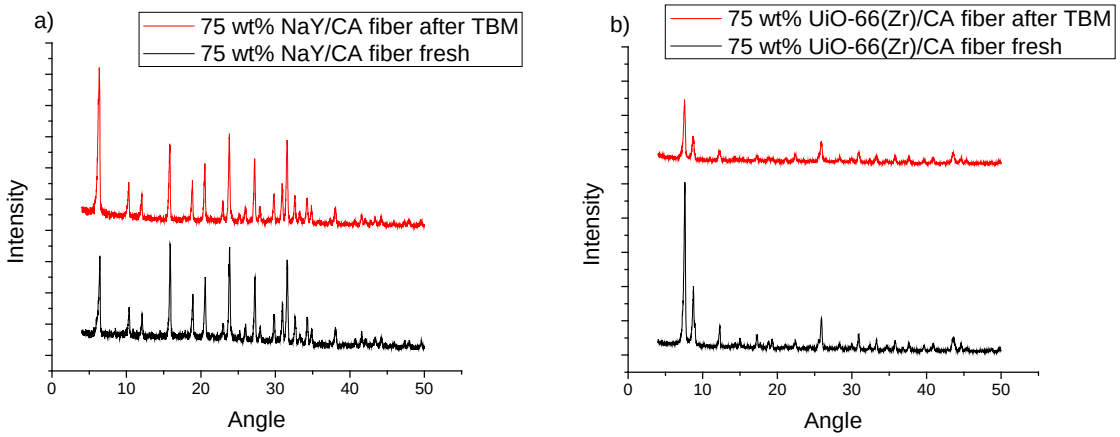

Figure 55*:* XRD patterns of fresh hybrid polymer-sorbent fibers and fibers after exposure to high temperature pretreatment and TBM adsorption: (a) NaY and (b) UiO-66(Zr).

The SEM images of the hybrid fibers after TBM adsorption are shown in Figure 56. The overall circular shape and morphology of the fiber remain unchanged from that of fresh fibers, indicating no pore structure change or damage with the application of heat and the adsorption and desorption of TBM. It is also qualitatively evident from these images that both NaY and UiO-66(Zr) sieves remain undamaged and contained inside of the polymer fiber structure.

6.2.2 SEM images of fiber sorbents after TBM adsorption

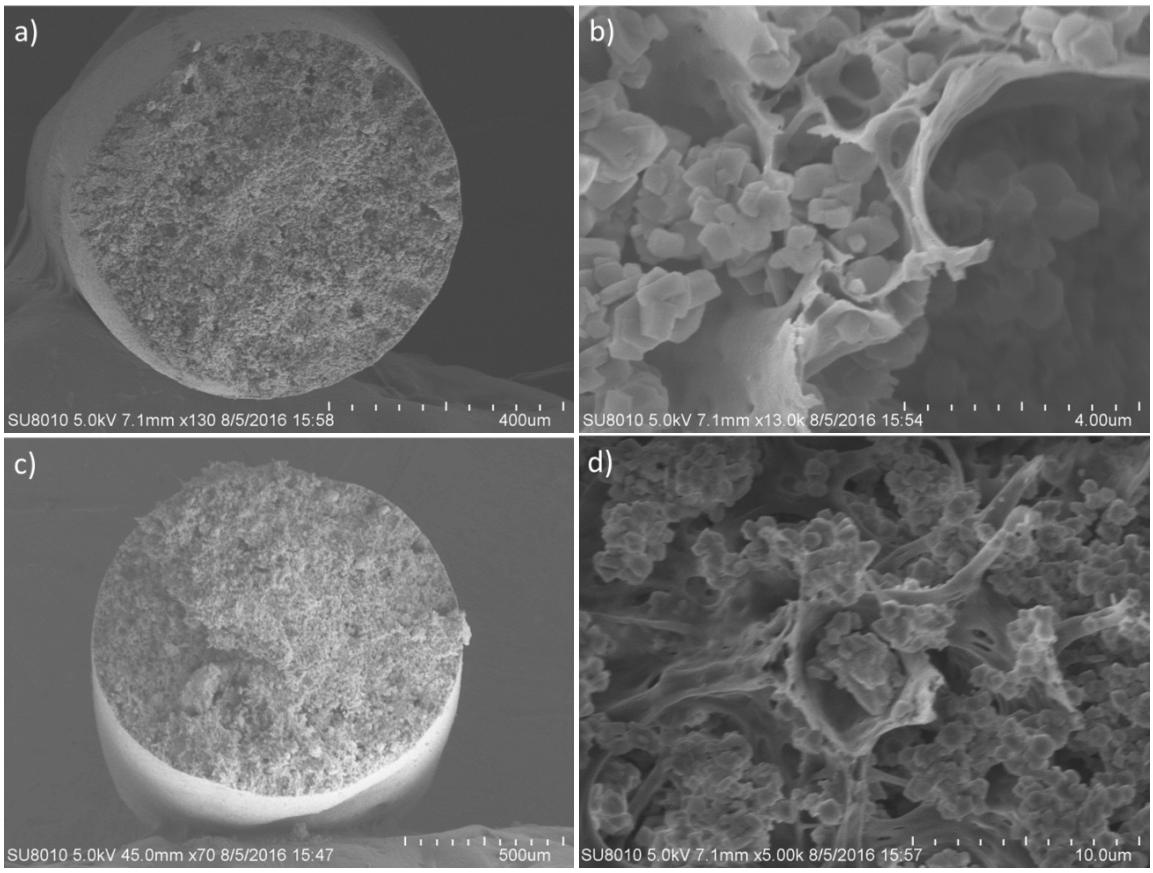

Figure 56: SEM images of hybrid fiber sorbents fibers after exposure to high temperature pretreatment and TBM adsorption: 75 wt % loaded NaY/CA fiber (a) cross section and (b) close-up of cross section showing NaY crystal dispersion in CA fiber matrix, and 75 wt % loaded UiO-66(Zr) fiber (c) cross section and (d) close-up of cross section showing UiO-66(Zr) crystal dispersion in CA fiber matrix.

6.2.3 TGA degradation curves of fiber sorbents before and after TBM adsorption

The thermal analysis (TGA) curves of the 75 wt% sorbent loaded NaY / CA and UiO-66(Zr) / CA hybrid fiber sorbents before and after TBM adsorption are shown in Figure 57. There appears to be no change in the shape of the TGA curves for fresh versus

"used" fibers for both NaY and UiO-66(Zr) hybrid fibers. Fresh NaY/CA fibers retain 59% of their original starting weight at the end temperature of 900°C while used NaY/CA fibers retain 60%, indicating no sorbent loss in these fibers after TBM cycling. Similarly, fresh UiO-66(Zr)/CA fibers retain 28% of their original starting weight while used fibers retain 27%, also demonstrating no sorbent loss in the fibers after TBM cycling.

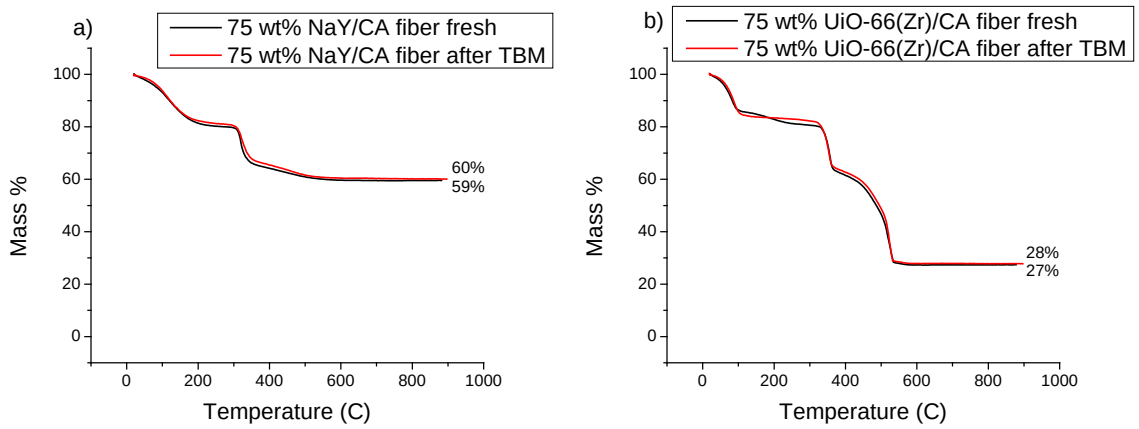

Figure 57: TGA curves of fresh hybrid polymer-sorbent fibers and fibers after exposure to high temperature pretreatment and TBM adsorption: (a) NaY and (b) UiO-66(Zr).

6.2.4 Nitrogen physisorption isotherms of fiber sorbents before and after TBM adsorption

The nitrogen physisorption measurement isotherms of both NaY / CA and UiO-66(Zr) / CA hybrid fibers are shown in Figure 58. As seen in the previous chapter, the isotherms of fresh fiber samples displayed type I isotherms without hysteresis between the adsorption and desorption curves, while the "used" fiber samples after TBM adsorption displayed type II isotherms without hysteresis. Type I isotherms indicate the

adsorption of a single monolayer of nitrogen on the sorbent surface, which is typical for microporous solids with fixed pore sizes such as zeolites and MOFs. The isotherm flattens as the adsorption reaches its limit in the completion of a monolayer. Type II isotherms indicate the completion of a monolayer near the first point of inflection, followed by adsorption in indefinite multi-layers. This type of isotherm is typical for materials with a distribution of pore sizes. A potential explanation for the change in isotherm shape is some degree of irreversible sorption of sulfur and other gases on the surface and pores of the fiber sorbents which gives the sorbents a pore size distribution and affects the perfect monolayer formation and isotherm shape, but is not large enough to significantly affect the TBM adsorption capacity reported in the previous chapter.

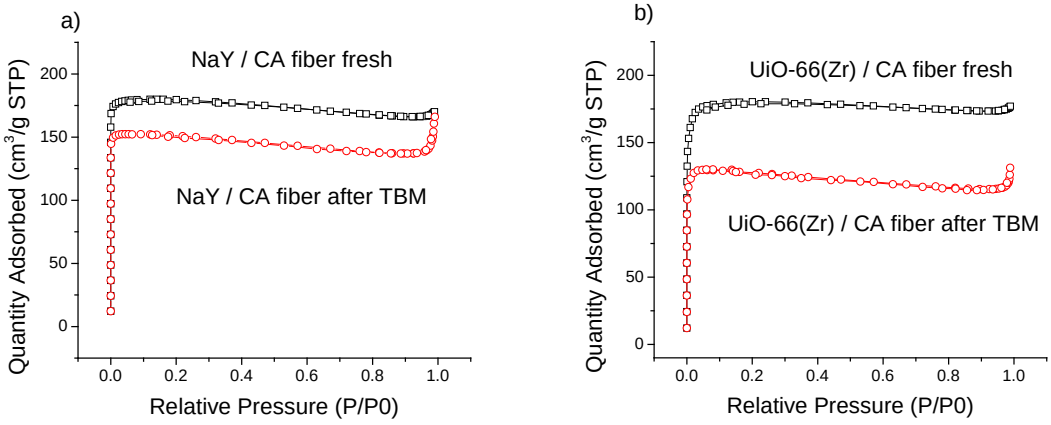

Figure 58: Nitrogen physisorption isotherms of hybrid fibers before and after exposure to high temperature pretreatment and TBM adsorption.

The surface area and t-plot micropore volumes calculated from the N_2 isotherm data using the Brunauer-Emmett-Teller (BET) method are summarized in Table 10. The textural properties of both NaY and UiO-66(Zr) fresh fibers show no significant changes after exposure to heat treatment and TBM adsorption, consistent with previous results

reported in Chapter 3 on the sorbent sieves alone. This is also consistent with the previous characterization trends indicating no structural damage or loss of sieves from within the fiber during TSA system experiments.

Table 10: Textural properties of materials before and after exposure to high temperature pretreatment and TBM adsorption

Sample	BET Surface Area (m^2/g)	t-plot Micropore Volume (cm^3/g)
75 wt% NaY/CA fiber fresh	598	0.26
75 wt% NaY/CA fiber after TBM	536	0.24
75 wt% UiO-66(Zr)/CA fiber fresh	652	0.26
75 wt% UiO-66(Zr)/CA fiber after TBM	568	0.20

6.2.5 Elemental analysis of fiber sorbents before and after TBM adsorption

The elemental analysis (EA) results of both NaY / CA and UiO-66(Zr) / CA fibers before and after TBM exposure in the original TSA system setup are shown in Table 11. As discussed above in Section 5.1, these EA results indicate that some amount of sulfur from the initial TBM adsorption on fresh material does remain in both NaY / CA and UiO-66(Zr) / CA fiber sorbents even after desorption in the original TSA system. This supported the hypothesis that the fiber sorbents were not getting properly heated to the desired temperature of 200ºC during the desorption step in the original system, and therefore a small portion of the adsorbed TBM was unable to be removed after the first adsorption. It was therefore necessary to implement a slightly new and different TSA system setup inside the process control box, as described in the Appendix. The new setup ensured that the fibers in the module got heated to the correct high temperature during the desorption step so that the fibers could be regenerated and cycled.

Table 11: Elemental analysis results of hybrid fibers before and after exposure to high temperature pretreatment and TBM adsorption in the original TSA setup

Sample	Carbon (wt %)	Hydrogen (wt %)	Zirconium (wt %)	Aluminum (wt %)	Silicon (wt %)	Sulfur (wt %)
75 wt% NaY/CA fiber fresh	10.11	3.51	n/a	7.62	17.88	n/a
75 wt% NaY/CA fiber after TBM	10.33	2.83	n/a	7.08	18.43	0.4
75 wt% UiO-66(Zr)/CA fiber fresh	37.69	3.50	21.24	n/a	n/a	n/a
75 wt% UiO-66(Zr)/CA fiber after TBM	34.05	2.75	21.03	n/a	n/a	0.2

It is noted that even with the original TSA system setup, the compositions of the rest of the fibers (C, H, N, Zr, Al, and Si elements) after TBM adsorption remains basically unchanged, again consistent with the other characterization results indicating that the sorbents remain intact and secured within the polymer fiber structure throughout the adsorption process. EA was not repeated on "used" fibers after cycles of adsorption and desorption in the newly modified TSA setup, as the amount of sulfur left in the fibers after adsorption and desorption in the original setup was small and the other characterizations (N_2 physisorption, XRD, SEM, degradation TGA) performed on fibers in the modified TSA setup showed no significant changes. Therefore, it was expected there would be negligible amounts of sulfur remaining in the fibers after desorption in the modified TSA system, even after multiple adsorption cycles.

The adsorption performance of hybrid fiber sorbents was investigated in a laboratory scale temperature swing adsorption flow system, and compared with the equilibrium adsorption results obtained from previous TGA experiments. The fiber sorbents retain a high mercaptan uptake capacity which was stable over many cycles of adsorption, illustrating that the sorbents are regenerable in the TSA system. Both of these factors are critical for the practical implementation and economic feasibility in an industrial odorant removal system. Certain trade-offs exist between the variables of flow rate and adsorption temperature studied in this portion of work. A larger volume of pipeline natural gas would be able to be processed in a given amount of time at higher feed flow rate, which also produces a sharper breakthrough front. However, the breakthrough point occurs much earlier at higher flow rates, which corresponds to a lower breakthrough and equilibrium capacity. Similarly, higher adsorption temperatures also correspond to lower capacities, but less time and energy would be needed to heat the fibers to the desorption temperature and cool them back down to adsorption temperature because the difference between the two temperatures is less. These trade-offs are important factors to consider when finalizing the design and operation of the odorant removal system.

CHAPTER 7

CONCLUSIONS AND FUTURE DIRECTIONS

7.1 Summary and Conclusions

In this first part of this work, seven materials, the MOFs Cu-BTC, MIL-53(Al), UiO-66(Zr), and ZIF-8 and the zeolites NaY, Beta, and ZSM-5, were synthesized or purchased and tested for equilibrium TBM adsorption capacities. After this initial screening, three MOF candidates with the best initial capacities [Cu-BTC, MIL-53(Al), and UiO-66(Zr)] were selected to be further compared to that of benchmark adsorbent material zeolite NaY. Cu-BTC displayed the highest initial adsorption capacity and is quite selective for TBM over methane and gas impurities; however, this capacity was completely lost by the second cycle because of irreversible binding of sulfur with the MOF and total destruction of the MOF structure. MIL-53(Al) displayed the second highest capacity and is also selective for TBM over methane and impurities but lost about 5% of its initial capacity with each subsequent cycle after the first cycle because of changes in its crystal structure. UiO-66(Zr) and NaY had similar sulfur capacities, regenerability, and stability, but UiO-66(Zr) is significantly more selective toward TBM than NaY, making it a good candidate for practical applications with pipeline-grade natural gas, which will contain water and other trace impurities that would compete with TBM adsorption.

Hybrid sorbent/polymer fibers incorporating the MOF UiO-66(Zr) and the zeolite NaY into a cellulose acetate network were developed for the purpose of organosulfur

odorant removal from pipeline natural gas by selective adsorption. This relative desulfurization approach offers several potential advantages over traditional pellet packed bed adsorption, which suffers from high pressure drops, slow heat and mass transfer, and particle attrition. Fiber sorbent morphology, composition, and sulfur capacities were characterized using a variety of techniques. Both NaY / CA and UiO-66(Zr) / CA fibers exhibited high capacities and selectivities for the odorant TBM in a model natural gas feed and were able to be regenerated by temperature swings over several cycles. NaY / CA fibers demonstrated higher overall adsorption capacities than UiO-66(Zr) / CA fibers, while UiO-66(Zr) / CA fibers demonstrated higher stability and selectivity. For pipeline NG with ultralow concentrations of contaminants or tightly controlled environments, NaY / CA fibers may be better suited for odorant removal, while UiO-66(Zr) / CA fibers may be more advantageous for pipeline NG with more impurities or for more variable environments because, percentage-wise, they will adsorb less of the impurities that may be present. The cyclic sulfur adsorption capacities of sorbents in their powder forms were also measured with a lower desorption temperature of 120 °C, which decreased their uptake by 24−40%. A thorough cost−benefit analysis would need to be performed to determine if the cost savings of the lower-temperature desorption can counterbalance this lower uptake. Moreover, the cost difference between the UiO-66(Zr) and NaY sieves must ultimately be considered; however, it is premature to attempt this comparison, because the UiO-66 manufacturing process is still undergoing optimization. A related technology that was not explored in this work, extruded monolithic contactors, may also be an acceptable alternative contactor for the desulfurization of natural gas.

An automated temperature swing adsorption (TSA) system was used to characterize the adsorption performance of NaY / CA and UiO-66(Zr) / CA fiber sorbents packaged into fiber modules. Both MOF and zeolite hybrid fibers retained high TBM adsorption capacity and regenerability in the TSA system. It was found that increasing model natural gas feed flow rates and increasing adsorption temperatures led to decreasing TBM uptake capacities. Though this inverse correlation exists and it is typically desired to increase the TBM uptake capacity as much as possible in adsorption processes, lower feed flow rates mean more time needed to process a given volume of gas, and lower adsorption temperatures mean a larger temperature swing needed (more energy and / or time intensive) between the adsorption and desorption temperature every cycle. It would be necessary to perform a cost-benefit analysis to economically optimize the TSA operating conditions before implementation in an industrial system.

Overall, the three research objectives of this project were met, and the work discussed in this dissertation provides a proof of concept that NaY / CA and UiO-66(Zr) / CA hybrid fiber sorbents can be easily fabricated and run continuously to remove odorants from natural gas in an automated TSA system. Further work still needs to be done to optimize and scale up the system from the lab scale used in the third objective to an industrial scale for processing the quantities of pipeline natural gas needed to operate off-shore gas turbines for electricity generation.

7.2 Recommendations and Future Directions

The results obtained for the fiber sorbent TSA system indicate that this setup is promising for future scale up for an industrial odorant removal system. Before this can happen, several system parameters and operating conditions would still need further investigation and optimization. Additionally, some of the issues and topics that were preliminarily explored in the body of this dissertation could be further examined and analyzed for completeness.

To expand on some of the work completed in this dissertation, more desorption temperatures should be considered with the hybrid fibers (rather than just the powder sieves) to assess the differences in swing capacity and how that affects the operating costs of the TSA system. It may be more cost effective to desorb the fibers at a lower temperature and / or adsorb at a higher temperature than optimal for the maximum TBM capacity if that would significantly reduce the energy needs, and thereby the operating costs, of the system. In addition, due to some of the heat transfer challenges faced in running the adsorption experiments in the TSA system discussed in Chapter 6 and the Appendix, it would be wise to double check the TBM adsorption capacity at different adsorption temperatures in the TGA. Because TGA experiments are less time consuming, it would also be interesting to study a wider range of adsorption temperatures and how that affects fiber sorbent performance. In the case that the capacities calculated from TGA adsorption experiments at 35-55 °C do not match well with the capacities calculated from experiments in the TSA system, it would be necessary to understand any discrepancies and rectify any issues with the TSA system. Another necessary experiment

is to run the adsorption system at actual pipeline natural gas pressures (typically 17-18 atms) rather than at atmospheric pressure as the experiments detailed in this dissertation are done at for simplicity. It is expected that the adsorption performance will change with this increased, but industrially realistic, pressure. It is also important to verify that the fibers themselves can withstand being under these high pressures without degradation or change to the fiber structure.

This current work provides some basic trends and correlations between different independent operating variables and their affects on adsorption performance, which is useful as a proof of concept and starting point for more detailed investigations. However, a thorough cost-benefit analysis and detailed modeling / simulation of all these variables would need to be completed to economically optimize the fiber sorbent module formation and operating conditions of the TSA system. Some variables that would need to be analyzed through cost-benefit analysis and modeling are feed flow rate, module size and optimal void fraction, timing of multiple adsorption beds, adsorption and desorption temperatures, and desorption gas composition.

In an industrial TSA system, it may also be more practical to use either nitrogen or a fraction of the treated, sulfur-free natural gas product as the desorption gas instead of helium. Nitrogen and treated natural gas is more cost effective than helium and may provide better heat transfer due to its higher density and heat capacity. However, nitrogen and natural gas may also adsorb more on the sorbents than helium, taking up sorbent sites that could otherwise be occupied by TBM molecules. It is therefore recommended to check the adsorption performance of the fiber sorbents using these two gases as the desorption gas under the same operating conditions used in this dissertation, and compare

the capacity results with what was obtained using helium as the desorption gas. Using a fraction of the product natural gas for desorption would likely be a better choice due to its availability from the process. In addition, this waste gas stream consisting of TBM-rich methane can then be burned, and the heat produced used as the heat source for subsequent desorption cycles. As described in previous work, this heat integration within the odorant removal system would significantly decrease its operating cost.[12]

A long term cost-benefit study on the effect of removing the odorants from natural gas before burning in the gas turbine is also needed to quantify the actual savings on corrosion and turbine lifetime. This benefit would need to be weighed against the capital and operating costs of the fiber sorbent system, including the cost of "spending" a fraction of the natural gas for desorption.

It may also be of interest to probe the reason(s) why MIL-53(Al) degrades during the fiber spinning process (described in Chapter 5) and investigate if there are some ways to modify the sorbent or spinning process to prevent this from happening. Creating stable hybrid MIL-53(Al) / CA fibers could be extremely beneficial for this sulfur adsorption application. MIL-53(Al) has a significantly higher mercaptan uptake capacity than zeolites, is much more selective for mercaptans than NaY (similar to UiO-66(Zr)), and is currently more economical to purchase in bulk than UiO-66(Zr).

APPENDIX

EXAMPLE CALCULATIONS AND CHALLENGES FACED

A.1 Fiber Sorbent Loading Calculation Based on TGA curves and EA

The sorbent loading in hybrid fibers were calculated from the thermogravimetric analysis curves performed in air shown in Figure 42 in the main text. (For clarification, this Netzsch TGA was used only to burn off all organic compounds at a high temperature in air in order to calculate the sieve loading. A separate TA Instruments TGA was used for TBM adsorption experiments.) From the figure, it can be seen that a filler-free, organic cellulose acetate fiber reacts with oxygen and completely degrades by the end of the analysis, as evidenced by the mass loss of almost 100%. The MOF UiO-66(Zr) partially degrades (the organic ligands are burned off), leaving only ZrO_2 behind by the end of the analysis. The molecular formula of UiO-66(Zr) is $C_{48}H_{24}O_{30}Zr_6$, which corresponds to a molecular weight of 1626 g/mol. The molecular weight of ZrO_2 is 123 g/mol. Using the 75 wt% UiO-66(Zr) / CA fiber as an example: The weight at the end of this analysis is 27% of the starting weight of the sample. Assuming a 100 g sample basis, and thus 27 g of ZrO_2 from the TGA curve, we use the following stoichiometric calculation to arrive at the weight of UiO-66(Zr) in this fiber sample:

$$27\ \text{g}\ ZrO_2 \times \frac{1\ \text{mol}\ ZrO_2}{123\ \text{g}\ ZrO_2} \times \frac{1\ \text{mol Zr}}{1\ \text{mol}\ ZrO_2} \times \frac{1\ \text{mol UiO-66}}{6\ \text{mol Zr}} \times \frac{1626\ \text{g UiO-66}}{1\ \text{mol UiO-66}} \quad (23)$$
$$= 59.5\ \text{g UiO-66(Zr)}$$

We then estimate the amount of water and other adsorbed atmospheric gases present in the sample by making the reasonable assumption that these species are fully desorbed by 200°C, the typical activation temperature for UiO-66(Zr). For the 75 wt% UiO-66(Zr) / CA sample, the weight loss at 200°C is 17.2 g (on a 100 g sample basis), which is then attributed to adsorbed species. Under these assumptions, the rest of the total sample weight can be attributed to cellulose acetate, as follows:

$$100 \text{ g sample} - 59.9 \text{ g } UiO\text{-}66(Zr) - 17.2 \text{ g adsorbed species} = 23.3 \text{ g CA} \tag{24}$$

Finally, the sorbent weight loading in this fiber on a dry fiber basis can be calculated:

$$\frac{59.5 \text{ g UiO-66(Zr)}}{\left[59.5 \text{ g UiO-66(Zr)} + 23.3 \text{ g CA}\right]} \times 100 = 72 \text{ wt\% UiO-66(Zr)} \tag{25}$$

This same method was used to calculate the true sorbent weight loading in the 50 wt% UiO-66(Zr) / CA fiber.

The assumption that only ZrO_2 is left behind at the end of the TGA run can be checked against elemental analysis (EA) results. For the same 75 wt% UiO-66(Zr) / CA sample, EA results show 21 wt% zirconium. Assuming a 100 g sample basis, and thus 21 g of Zr from the EA results, we use the following stoichiometric calculation to arrive at the weight of ZrO_2 in this fiber sample:

$$21 \text{ g Zr} \times \frac{1 \text{ mol Zr}}{91 \text{ g Zr}} \times \frac{1 \text{ mol } ZrO_2}{1 \text{ mol Zr}} \times \frac{123 \text{ g } ZrO_2}{1 \text{ mol } ZrO_2} = 28 \text{ g } ZrO_2 \tag{26}$$

This matches closely with the TGA results of 27 wt% ZrO_2. The same calculation can be done for 50 wt% UiO-66(Zr) / CA.

Checking again for the UiO-66(Zr)LB sample:

$$25\ \text{g Zr} \times \frac{1\ \text{mol Zr}}{91\ \text{g Zr}} \times \frac{1\ \text{mol } ZrO_2}{1\ \text{mol Zr}} \times \frac{123\ \text{g } ZrO_2}{1\ \text{mol } ZrO_2} = 34\ \text{g } ZrO_2 \tag{27}$$

This again matches closely with the TGA results of 35 wt% ZrO_2.

The zeolite NaY only releases adsorbed species up to about 200 °C, but does not degrade or chemically react in this analysis unlike the filler-free CA fiber, which degrades completely. Thus, in TGA curves for the NaY / CA composite fibers, we can assume the weight at the end of the analysis is from NaY sieve alone. Using the 75 wt% NaY / CA fiber as an example: The weight at the end of this analysis is 62% of the starting weight of the sample. Assuming a 100 g sample basis, this corresponds to 62 g of NaY.

We then estimate the amount of water and other adsorbed atmospheric gases present in the sample by making the reasonable assumption that these species are fully desorbed by 300 °C, the typical activation temperature for NaY. From the curve for filler-free CA fiber, we can assume that the CA part of the composite NaY / CA fiber does not experience a significant mass loss at this temperature. For the 75 wt% NaY / CA sample, the weight loss at 300°C is 18 g (on a 100 g sample basis), which is then attributed to adsorbed species. Under these assumptions, the rest of the total sample weight can be attributed to cellulose acetate, as follows:

$$100\ \text{g sample} - 62\ \text{g NaY} - 18\ \text{g adsorbed species} = 20\ \text{g CA} \tag{28}$$

Finally, the sorbent weight loading in this fiber on a dry fiber basis was calculated:

$$\frac{62\ \text{g NaY}}{\left[62\ \text{g NaY} + 20\ \text{g CA}\right]} \times 100 = 76\ \text{wt\% NaY} \tag{29}$$

This same method was used to calculate the true sorbent weight loading in the 50 wt% NaY / CA fiber.

A.2 Example TSA Capacity Calculation

All raw concentration data obtained from the mass spectrometer was first smoothed in Origin using the Smooth tool to remove noise from the TBM signal. This data was then transferred to Excel to calculate capacity. The data from the UiO-66(Zr) / CA fiber module containing 3 fibers with a feed flow rate of 40 sccm and adsorption temperature of 35 °C is used for this example calculation.

From the plot of TBM concentration (%) versus time (hours) breakthrough plot, the time at which the system reached equilibrium was determined visually, and the TBM concentration value from that time point to the end of the run was averaged. This averaged value was the experimental equilibrium concentration. From Figure 59 below, the system reached equilibrium around 25 hours. Averaging the TBM concentration signal from 25 to 28.5 hours when the run ended, the experimental equilibrium concentration was 0.0075%, or 75 ppm.

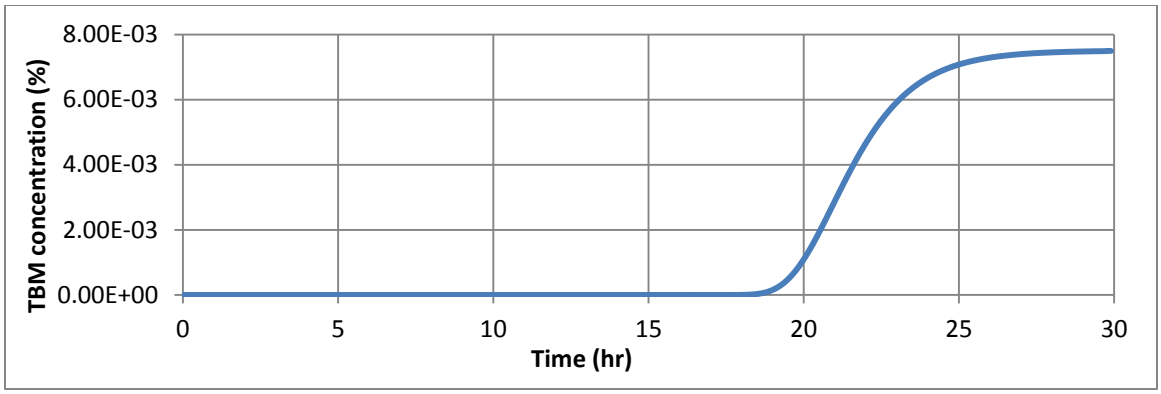

Figure 59: The original smoothed breakthrough curve for UiO-66(Zr)/CA fiber module at 40 sccm flow rate and 35°C adsorption temperature, plotted in Excel.

The actual equilibrium concentration is 60 ppmv, the known concentration in the gas cylinder. The experimental TBM concentration signal was normalized to the actual TBM concentration by the experimental equilibrium concentration to the actual equilibrium concentration using the following equation:

$$C_{actual} = C_{\exp} \times \frac{C_{eq,actual}}{C_{eq,\exp}} \tag{30}$$

where C_{actual} is the calculated actual TBM concentration, C_{exp} is the experimental TBM signal shown in Figure 59, $C_{eq,actual}$ is 0.0075% and $C_{eq,exp}$ is 0.006%. This normalized curve was replotted as shown in Figure 60.

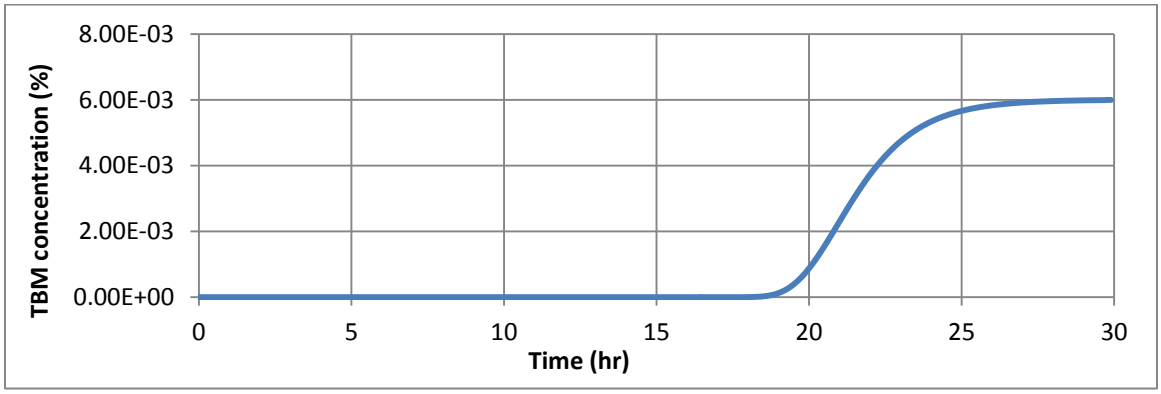

Figure 60: The normalized breakthrough curve for UiO-66(Zr)/CA fiber module at 40 sccm flow rate and 35°C adsorption temperature, plotted in Excel.

The curve was then inverted by taking the difference of the normalized concentration signal from the equilibrium value as shown in Figure 61.

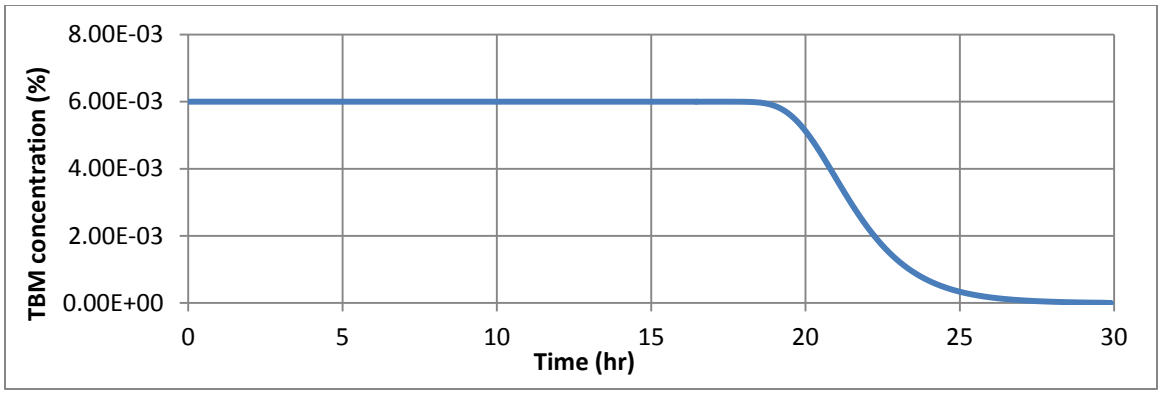

Figure 61: The inverted normalized breakthrough curve for UiO-66(Zr)/CA fiber module at 40 sccm flow rate and 35°C adsorption temperature, plotted in Excel.

The rectangle method was then used to calculate the area, A, under this new inverted curve where the width of each rectangle is the difference between adjacent time points and the height is the TBM signal at the first time point. Fiber density in g/cm was obtained by measuring different lengths and weights of fibers and averaging the value. The mass of fibers was then calculated using the following equation:

$$m_f = \rho_f \cdot n_f \cdot L_f = 0.0012 \frac{g}{cm} \times 3\, fibers \times 17 cm = 0.061 g \quad (31)$$

where ρ_f is the fiber density in g/cm, n_f is the number of fibers in the module, and L_f is the length of the fibers. It is noted that the stainless steel module length was 8 inches (or approximately 20 cm), but the ends of fiber sorbents were sealed into the module with epoxy, and therefore the "useable" fiber length that got exposed to flowing gases was approximately only 17 cm, which is the L_f value used in these sample calculations.

The flow rate was converted from standard cubic centimeters per minute (sccm) to a mass flow rate in grams per second, assuming the density of natural gas as 0.8 kg/m^3:

$$\dot{m} = \dot{V} \cdot \left(\frac{T_{act}}{T_{std}} \right) \cdot \rho_{NG} = 40 sccm \times \left(\frac{308K}{273K} \right) \times 0.8 \frac{kg}{m^3} \times \frac{1 min}{60 s} \times \frac{1000 g}{1 kg} \times \frac{1 m^3}{10^6 cm^3} = 6.02 \times 10^{-4} \frac{g}{s}$$

(32)

where ṁ is mass flow rate in g/s, V̇ is volumetric flow rate in sccm, T_{act} is the temperature of adsorption in Kelvins, T_{std} is standard temperature 273K.

The amount of TBM adsorbed per gram of fiber was then calculated via:

$$q_{eq,f} = \frac{A \cdot \dot{m}}{100 \cdot m_f} = \frac{(469\% \cdot s) \times \left(6.02 \times 10^{-4} \frac{g}{s} \right)}{100 \times 0.061 g} = 0.046 \frac{\text{g TBM}}{\text{g fiber}} \quad (33)$$

where $q_{eq,f}$ is the equilibrium capacity in g TBM / g fiber, and A is the area under the curve calculated from rectangle method.

The TBM adsorbed per gram of fiber was converted to a sorbent basis via:

$$q_{eq,s} = \frac{q_{eq,f}}{w_s} = \frac{0.046 \text{ g TBM} / \text{g fiber}}{0.72} = 0.064 \frac{\text{g TBM}}{\text{g sorbent}} \quad (34)$$

where $q_{eq,s}$ is the equilibrium capacity in g TBM / g sorbent, and w_s is the sorbent weight loading in the fiber.

To calculate breakthrough capacity, the same procedure was repeated except the area under the inverted curve was only summed to the breakthrough time; in this example, to about 15 hours.

A.3 Fiber Sorbent Module Flow Calculations

The module void fraction and interstitial velocity of the model natural gas through the module was also calculated to help characterize system behavior. The flow rate was first converted from standard cubic centimeters per minute (sccm) to a volumetric flow rate at the experimental conditions in cubic centimeters per second. In this example calculation, a fixed flow rate of 40 sccm is used:

$$\begin{aligned} \dot{V}_{NG,actual} &= \dot{V}_{NG,std} \times \left(\frac{P_{std}}{P_{actual}} \right) \times \left(\frac{T_{actual}}{T_{std}} \right) \\ &= 40 sccm \times \left(\frac{1 \text{ atm}}{1 \text{ atm}} \right) \times \left(\frac{308K}{273K} \right) \times \left(\frac{1 \text{ min}}{60 \text{ s}} \right) = 0.752 \frac{cm^3}{s} \end{aligned} \tag{35}$$

The outer diameter of the stainless steel module was ¼ inch, or 0.635 cm, and the wall thickness was 0.083 inch, or about 0.211 cm. The inner diameter of the module could then be calculated:

$$d_{m,i} = d_{m,o} - \left(2 \cdot d_{m,t} \right) = 0.635 - (2 \times 0.211) = 0.213 \text{ cm} \tag{36}$$

where $d_{m,i}$, $d_{m,o}$, and $d_{m,t}$, are the module inner diameter, outer diameter, and wall thickness, respectively.

The cross-sectional inner area of the module, A_m, was then calculated via:

$$A_m = \frac{\pi}{4} \times (d_{m,i})^2 = \frac{\pi}{4} \times (0.213 \text{ cm})^2 = 0.036 \text{ cm}^2 \tag{37}$$

With the number of fibers in each module (N_f) of 3, and an average fiber diameter (d_f) of about 700 μm, or 0.07 cm, the filled cross-sectional space of the module, A_f, was calculated as:

$$A_f = \frac{\pi}{4} \times (d_f)^2 \times N_f = \frac{\pi}{4} \times (0.07 \text{ cm})^2 \times 3 = 0.012 \text{ cm}^2 \quad (38)$$

The void fraction of the module could then be calculated by subtracting out the fraction of the total module area that is filled with fibers:

$$\varepsilon_m = 1 - \left(\frac{A_f}{A_m} \right) = 1 - \left(\frac{0.012 \text{ cm}^2}{0.036 \text{ cm}^2} \right) = 0.68 \quad (39)$$

The interstitial velocity for a 3-fiber module flowing model natural gas at 40 sccm is then calculated as:

$$v_i = \frac{\dot{V}_{NG,actual}}{A_m} \times \frac{1}{\varepsilon_m} = \frac{0.752 \, cm^3/s}{0.036 \, cm^2} \times \frac{1}{0.68} = 31.1 \, \frac{cm}{s} \quad (40)$$

A.4 Mass Transfer Analysis

Gas transport and adsorption on solids generally experience mass transfer resistance in three distinct regions in and around the fiber sorbent: 1) The external (or bulk) diffusion from the bulk feed gas stream through the boundary layer to the outer surface of the sorbent; 2) The internal mesopore and macropore diffusion through the pores of the fiber; and 3) The internal micropore diffusion through the pores of the sorbent crystals contained within the fiber. The internal mass transfer resistance in the sorbent (zeolite or MOF) crystals was expected to be negligible compared to the internal meso/macropore resistance and the external film layer resistance. Both types of sorbents had small crystal sizes within the range of 1 μm diameter, high sorption affinities (as

detailed in the main text) for TBM, and large pores compared to the diameter of a TBM molecule. These characteristics lead to this internal diffusion step happening fast, and therefore the rate controlling step is not in this region. Example calculations for the mass transfer coefficients in the first two regions are shown in this section for a 3-fiber module with a feed flow rate of 40 sccm and adsorption temperature of 35 °C.

A.4.1 Residence Time

First, the residence time of gas flowing through a fiber module can be calculated from knowing the interstitial velocity and the length of the module (L_m):

$$t_{residence} = \frac{L_m}{v_i} = \frac{17\ cm}{31.1 cm/s} = 0.55s \tag{41}$$

This is the average amount of time that a gas molecule will spend inside the module. The residence time must be long enough for heat and mass equilibration to happen. This will be checked in later sections.

A.4.2 Binary Diffusion Coefficient

$D_{TBM\text{-}CH4}$ is the molecular diffusivity, or diffusion coefficient, which can be estimated from the Chapman-Enskog equation for gaseous systems.[88] For a binary gas mixture such as the one between TBM and CH_4 (assumed to be the only two species in this calculation), the binary diffusion coefficient can be calculated as:

$$D_{TBM-CH4} = \frac{1.858\times10^{-23}\times T^{\frac{3}{2}}}{P\sigma^2_{TBM-CH4}\Omega}\times\left(\frac{1}{MW_{TBM}}+\frac{1}{MW_{CH4}}\right)^{\frac{1}{2}} \quad (42)$$

where MW_{TBM} and MW_{CH4} are the molecular weights of TBM and methane respectively, P is the total pressure in atmospheres, T is temperature in Kelvins, Ω is the temperature-dependent dimensionless collision integral of order 1, and $\sigma_{TBM-CH4}$ is the average collision diameter, calculated as $\sigma_{TBM-CH4}=0.5(\sigma_{TBM}+\sigma_{CH4})$.

With the following specifications of M_{TBM} =90.19 g/mol, M_{CH4} =16.04 g/mol, σ_{CH4} =3.89 Å, σ_{TBM} ≈ 5.6 Å, ($\sigma_{TBM-CH4}$ = 4.75 Å), T=308 K, P=1 atm, the diffusivity is:

$$D_{TBM-CH4} = \frac{1.858\times10^{-23}\times(308K)^{\frac{3}{2}}}{(1\ atm)\times\left(4.75\times10^{-10}m\right)^2\times(1.667)}\times\left(\frac{1}{90.19g/mol}+\frac{1}{16.04g/mol}\right)^{\frac{1}{2}} \approx 0.072\frac{cm^2}{s}$$

This diffusion coefficient is valid for the external film layer that surrounds a fiber. However, it must be modified to account for the sorbent and / or polymer when calculating the mass transfer inside of the fiber or pellet.

A.4.3 External Mass Transfer Coefficient (Film Layer)

Determination of the external mass transfer coefficient, k_{ext} is easiest using Sherwood correlations that accurately describe the situation of interest. The Sherwood number is first estimated from the correlation, and then the definition of Sherwood number is applied to find the external mass transfer coefficient using the following definition:

$$Sh \equiv \frac{d\cdot k_{ext}}{D} \quad (43)$$

The diffusion coefficient in this region is simply the binary diffusion coefficient calculated previously, as there are no hindrances (Knudsen diffusion) in this external region. The gas molecules only interact with each other.

The dimensionless Schmidt number (Sc), present in the Sherwood (Sh) correlations, is calculated below:

$$Sc = \frac{\mu_{NG}}{D_{TBM-CH4}\rho_{NG}} = \frac{1.67\times10^{-5}\ Pa\cdot s}{\left(7.2\times10^{-6}\ m^2/s\right)\times\left(0.8\frac{kg}{m^3}\right)} = 2.88 \quad (44)$$

The dimensionless Reynolds number (Re) must also be calculated for the fiber sorbent module:

$$Re = \frac{d_f v_i \rho_{NG}}{\mu_{NG}} = \frac{(0.0007m)\times\left(31.1\ \frac{cm}{s}\times\frac{1\ m}{100\ cm}\right)\times\left(0.8\frac{kg}{m^3}\right)}{1.67\times10^{-5}\ Pa\cdot s} = 10.42 \quad (45)$$

For flow outside and parallel to a bundle of fibers, the Sherwood number can be correlated from the Reynolds and Schmidt numbers as:[93]

$$Sh = 1.45\left[ReSc\frac{d_f}{L_m}\right]^{0.33} = 1.45\left[10.42\times2.88\times\frac{0.07cm}{17cm}\right]^{0.33} = 0.728 \quad (46)$$

Rearranging and solving equation (43) for the external mass transfer coefficient:

$$(k_{ext})_f = \frac{Sh\cdot D_{TBM-CH4}}{d_f} = \frac{0.728\times0.072\ cm^2/s}{0.07cm} = 0.752\frac{cm}{s} \quad (47)$$

A.4.4 Internal Mass Transfer Coefficient (Fiber Layer)

The diffusion of a gas through the meso and macropores of a fiber or pellet is hindered by the sorbent such that the effective diffusivity, D_{eff}, is lower than the binary diffusion coefficient. First, the mean free path of the molecules must be determined. An example calculation of the mean free path of a TBM molecule at a fixed adsorption temperature of 35 °C is shown below:

$$\lambda_{TBM} = \frac{k_B T}{\sqrt{2}\pi d_{TBM}^2 P} = \frac{\left(1.38\times10^{-23}\,\frac{m^2 kg}{s^2 K}\right)\times(308K)}{\sqrt{2}\pi\left(5.6\times10^{-10}m\right)^2\times(101{,}325Pa)} = 3.01\times10^{-8}m \qquad (48)$$

Similarly, the mean free path can be calculated for the TBM molecule at the regeneration temperature of 200 °C, and also for the methane molecules at both temperatures. These various mean free paths are shown in Table 12.

Table 12: Mean free path for TBM and methane molecules at feed and regeneration temperatures

Temperature	TBM Mean Free Path (m)	Methane Mean Free Path (m)
35°C	$3.01\text{x}10^{-8}$	$6.21\text{x}10^{-8}$
200°C	$4.62\text{x}10^{-8}$	$9.53\text{x}10^{-8}$

The average pore diameter of a fiber sorbent containing zeolite or MOF sorbent ranges from 1 to 2 microns, with the most typical diameter being 1 micron, or 10^{-6} meters.[81] The mean free paths of both TBM and methane molecules at both temperatures are well below an order of magnitude less than the pore radius, indicating that only molecular diffusion, rather than Knudsen diffusion, will be important in this region. That

is, the gas molecules collide with each other more than with the pore walls and this provides the main diffusional resistance to flow.

The effective diffusivity is then:

$$D_{eff} = \frac{\varepsilon_f D_{TBM-CH4}}{\tau} \approx \frac{0.33 \times 0.072 \frac{cm^2}{s}}{3} = 0.008 \frac{cm^2}{s} \quad (49)$$

The tortuosity factor, τ, accounts for the effect of the random orientation of the pores and the variation in the pore diameter, and varies inversely with porosity. For straight, randomly oriented cylindrical pores, it was shown that τ =3, and experimental tortuosity factors generally fall within the range of 2-6.[85] For the purposes of this design study, the tortuosity factor is taken to be 3, and the porosity of the fiber, ε_f, is estimated as $\varepsilon_f \approx 1/\tau$.

The shape factor (SF) for catalysts or adsorbers is generally defined as the volume of the sorbent over the surface area of the sorbent, such that for solid cylinders, the shape factor simplifies to r/2. Applying this shape factor to Liaw et al.'s method for internal mass transfer coefficient in a solid cylinder (long enough for end effects to be negligible),[117] the internal MTC for the pores of the fiber was calculated as:

$$(k_{int})_f = \frac{8 D_{eff}}{r_f^{\,2}} \times \frac{r_f}{2} = \frac{8\left(0.008 \frac{cm^2}{s}\right)}{(0.035cm)^2} \times \frac{0.035cm}{2} = 0.919 \frac{cm}{s} \quad (50)$$

The external and internal mass transfer coefficients have the same magnitude, and are therefore both important contributors to the controlling mass transfer resistance in the fiber module system. The external mass transfer coefficient is slightly smaller and would be the controlling resistance in this case.

A.5 Challenges Faced

As mentioned in Chapter 5, during desorption in the initial experiments in the original TSA system setup, the helium desorption gas experienced difficulty reaching the desired desorption temperature of 200 °C. More specifically, the original experimental setup had trouble with fiber sorbent regeneration during attempts to perform cycling experiments. It was discovered that this problem was due to insufficient heating during the desorption step. The amount of heat provided by the heat tape in the original setup and continuous flow of the helium desorption gas was sufficient to perform the pretreatment step on the fresh fibers, but was not enough to remove the adsorbed TBM during the desorption step (same conditions as the pretreatment step).

In the TSA setup, heating tape and insulation was wrapped around a portion of 3 ft long, ¼ inch diameter stainless steel tubing connecting the helium gas cylinder (located outside of the fume hood) to the inlet of the fiber module contained within the experimental process control box inside the fume hood. The heating tape was set at 200 °C during the preheating / desorption steps to preheat the helium gas before it entered the process control box, as shown in Figure 62. This outside portion was kept the same between the original and modified TSA setup.

Figure 62: Photo of the overall TSA system setup including process control box, mass spectrometer, and 60 ppm TBM/CH_4 gas cylinder located inside of the walk-in fume hood, as well as the helium desorption cylinder located outside of the fume hood.

Within the process control box in the original TSA setup, shown in Figure 63(a), the preheated helium gas passed through tubing and valves ambiently heated with a convection heater inside the box to between 35-55°C (depending on the adsorption temperature used), before passing through the module itself which was also heated to 200°C during the desorption step with heat tape and insulation wrapped on the outside of the module. With this setup, the inlet gas temperature (measured right before the module entrance as shown in Figure 23) only reached about 60°C and the outlet gas temperature (measured right after the module exit) only reached about 65°C during the desorption step. Here, both NaY / CA and UiO-66(Zr) / CA fiber sorbents showed significantly

lower TBM uptake capacities in the second adsorption cycle than they were capable of achieving in the first adsorption cycle.

It was hypothesized that the helium gas was not getting sufficiently heated with the lengths of heating tape used, and / or was losing heat to the unwrapped and uninsulated tubing and valves located within the experiment box. The low density of helium gas (0.17 kg/m^3 under ambient temperature and pressure) coupled with the high thermal conductivity of the stainless steel module (45 W/m K at ambient temperatures) means that the helium gas loses heat quickly to the module, which then also quickly dissipates it to the surrounding air in the process control box. To remedy this heating problem, the TSA setup was modified as pictured in Figure 63(b). The helium gas was re-routed through a long length of 1/8 inch stainless steel tubing, which was coiled and submerged in an oil bath heated to the desorption temperature, before once again passing through the fiber module. The smaller diameter and longer length of the new tubing inside the experiment box made for greater heat transfer to the helium gas, as well as better heat retention before entering the module. With this newly modified setup, the inlet gas temperature was able to reach ~190°C and the outlet gas temperature was able to reach ~195°C; much closer to the desired desorption temperature, and the fiber sorbents were able to be regenerated and retained close to their high initial TBM uptake capacities over multiple adsorption runs.

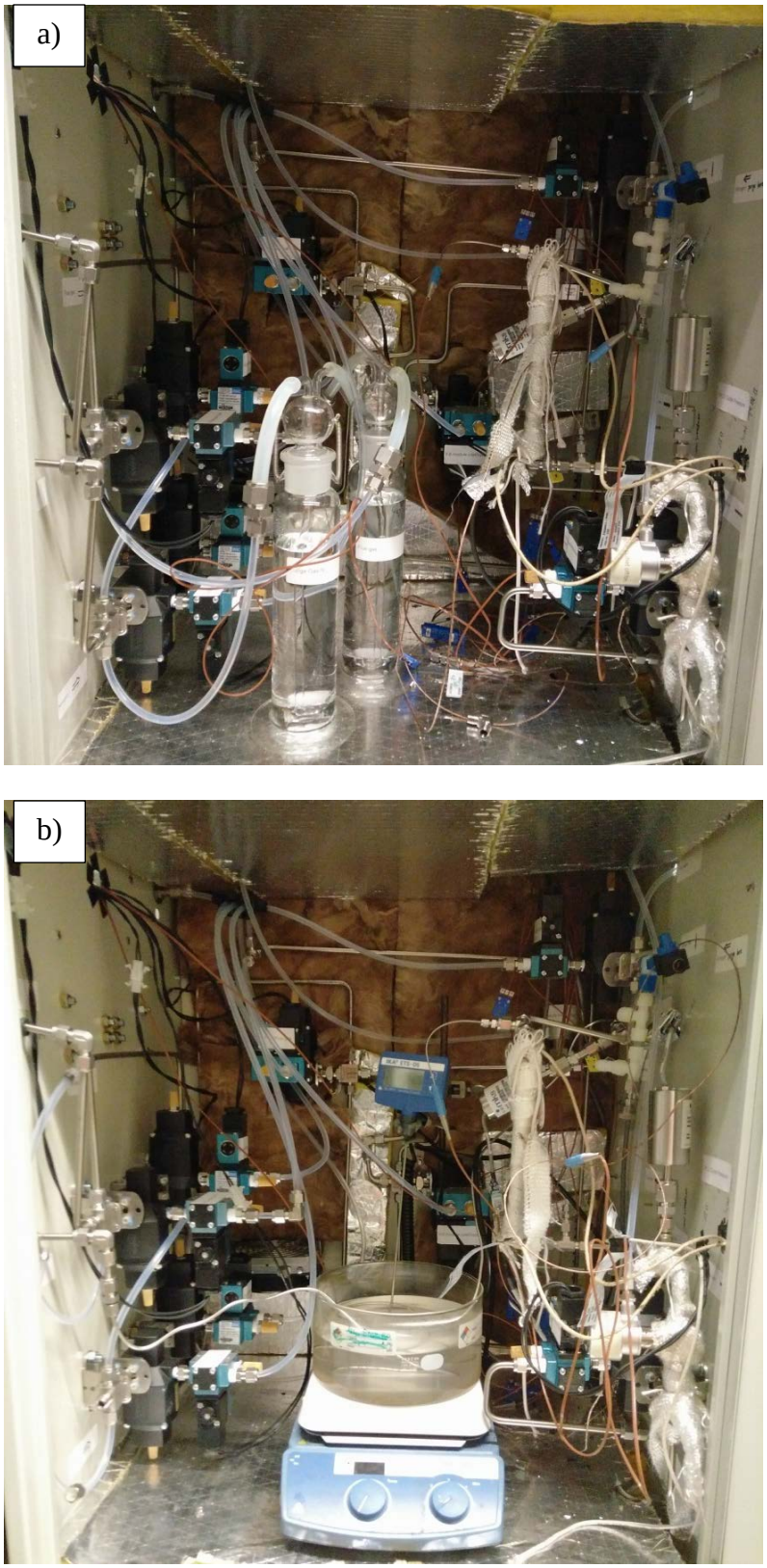

Figure 63: Photo of the fiber sorbent module wrapped in heat tape and insulation inside of the process control box in the a) original and b) modified TSA system setup.

REFERENCES

1. Annual Energy Outlook. U.S. Energy Information Administration: 2015 Vol. AEO2015.

2. Key World Energy Statistics. The International Energy Agency: 2016.

3. High Temperature Corrosion and Materials Application ASM International: Materials Park, Ohio, 2007; pp 249-258.

4. Casanova, M., Corrosion problems in turbines. *Proceedings of the Second Turbomachinery Symposium* **1973**, 83-90.

5. Drajem, M.; Olson, B., The future of oil, coal, and gas under Obama. *Bloomberg Businessweek* 2012.

6. Market Digest: Natural Gas (2013-2014). *Natural Gas Market Digest* 2014.

7. Corrosion costs and preventive strategies in the United States 2002.

8. Overview of Natural Gas: Electric generation using natural gas. Natural Gas Supply Association: 2011.

9. About Energy: Natural Gas: Featured Plant Profile: Plant McDonough-Atkinson. Georgia Power: 2013.

10. Ivanov, I.; Strmen, J.; Jones, L., Pre-odorization or pickling of new natural gas pipe. *Pipeline & Gas Journal* **2009,** *236* (11), 1-4.

11. Bammert, K.; Santstede, H., Measurements concerning the influence of surface roughness and profile changes on the performance of gas turbines. *Journal of Engineering for Gas Turbines and Power* **1972,** *94* (3), 207-213.

12. Chen, G.; Lively, R. P.; Jones, C. W.; Koros, W. J., Fiber Adsorbents for Odorant Removal from Pipeline Grade Natural Gas. *Ind. Eng. Chem. Res.* **2014,** *53* (17), 7113-7120.

13. de Wild, P. J.; Nyqvist, R. G.; de Bruijn, F. A.; Stobbe, E. R., Removal of Sulphur-Containing Odorants from Fuel Gases for Fuel Cell-Based Combined Heat and Power Applications. *J. Power Sources* **2006,** *159* (2), 995-1004.

14. Craig, B. D.; Smith, L., Corrosion resistant alloys (CRA) in the oil and gas industry – selection guidelines update, 3rd Edition. *Nickel Institute Technical Series* 2011.

15. Brunet, S.; Mey, D.; Perot, G.; Bouchy, C.; Diehl, F., On the Hydrodesulfurization of FCC Gasoline: A Review. *Appl. Catal., A* **2005,** *278* (2), 143-172.

16. Kang, S.-H.; Bae, J.-W.; Kim, H.-T.; Jun, K.-W.; Jeong, S.-Y.; Chary, K. V. R., Effective removal of odorants in gaseous fuel for the hydrogen station using hydrodesulfurization and adsorption. *Energy & Fuels* **2007,** *21* (6), 3537-3540.

17. Alptekin, G.; DeVoss, S.; Dubovik, M.; Monroe, J.; Amalfitano, R.; Israelson, G., Regenerable sorbent for natural gas desulfurization. *Journal of Materials Engineering and Performance* **2006,** *15* (4), 433-438.

18. Ratnasamy, C.; Wagner, J. P.; Spivey, S.; Weston, E., Removal of sulfur compounds from natural gas for fuel cell applications using a sequential bed system. *Catalysis Today* **2012,** *198* (1), 233-238.

19. Wakita, H.; Tachibana, Y.; Hosaka, M., Removal of Dimethyl Sulfide and t-Butylmercaptan from City Gas by Adsorption on Zeolites. *Microporous Mesoporous Mater.* **2001,** *46* (2-3), 237-247.

20. Gardner, T. H.; Berry, D. A.; Lyons, K. D.; Beer, S. K.; Freed, A. D., Fuel processor integrated H2S catalytic partial oxidation technology for sulfur removal in fuel cell power plants. *Fuel* **2002,** *81* (17), 2157-2166.

21. Chica, A.; Gatti, G.; Moden, B.; Marchese, L.; Iglesia, E., Selective catalytic oxidation of organosulfur compounds with tert-butyl hydroperoxide. *Chemistry-a European Journal* **2006,** *12* (7), 1960-1967.

22. Cui, H.; Turn, S. Q.; Reese, M. A., Removal of Sulfur Compounds from Utility Pipelined Synthetic Natural Gas using Modified Activated Carbons. *Catal. Today* **2009,** *139* (4), 274-279.

23. Wu, X. X.; Kercher, A. K.; Schwartz, V.; Overbury, S. H.; Armstrong, T. R., Activated carbons for selective catalytic oxidation of hydrogen sulfide to sulfur. *Carbon* **2005,** *43* (5), 1087-1090.

24. Shen, Y.; Li, P.; Xu, X.; Liu, H., Selective Adsorption for Removing Sulfur: A Potential Ultra-Deep Desulfurization Approach of Jet Fuels. *RSC Adv.* **2012,** *2* (5), 1700-1711.

25. Clausse, M.; Bonjour, J.; Meunier, F., Adsorption of Gas Mixtures in TSA Adsorbers under Various Heat Removal Conditions. *Chem. Eng. Sci.* **2004,** *59* (17), 3657-3670.

26. Ko, C. H.; Song, H.-I.; Park, J.-H.; Han, S.-S.; Kim, J.-N., Selective removal of sulfur compounds in city-gas by adsorbents. *Korean Journal of Chemical Engineering* **2007,** *24* (6), 1124-1127.

27. Koriakin, A.; Kim, Y.-H.; Lee, C.-H., Adsorptive Desulfurization of Natural Gas Using Lithium-Modified Mesoporous Silica. *Ind. Eng. Chem. Res.* **2012,** *51* (44), 14489-14495.

28. Achmann, S.; Hagen, G.; Hammerle, M.; Malkowsky, I.; Kiener, C.; Moos, R., Sulfur Removal from Low-Sulfur Gasoline and Diesel Fuel by Metal-Organic Frameworks. *Chem. Eng. Technol.* **2010,** *33* (2), 275-280.

29. Barea, E.; Montoro, C.; Navarro, J. A. R., Toxic Gas Removal - Metal-Organic Frameworks for the Capture and Degradation of Toxic Gases and Vapours. *Chem. Soc. Rev.* **2014,** *43* (16), 5419-5430.

30. Blanco-Brieva, G.; Campos-Martin, J. M.; Al-Zahrani, S. M.; Fierro, J. L. G., Effectiveness of Metal-Organic Frameworks for Removal of Refractory Organo-Sulfur Compound Present in Liquid Fuels. *Fuel* **2011,** *90* (1), 190-197.

31. Chen, G.; Tan, S.; Koros, W. J.; Jones, C. W., Metal Organic Frameworks for Selective Adsorption of t-Butyl Mercaptan from Natural Gas. *Energy Fuels* **2015,** *29* (5), 3312-3321.

32. Khan, N. A.; Hasan, Z.; Jhung, S. H., Adsorptive Removal of Hazardous Materials using Metal-Organic Frameworks (MOFs): A Review. *J. Hazard. Mater.* **2013,** *244*, 444-456.

33. Khan, N. A.; Jhung, S. H., Adsorptive Removal of Benzothiophene using Porous Copper-Benzenetricarboxylate Loaded with Phosphotungstic Acid. *Fuel Process. Technol.* **2012,** *100*, 49-54.

34. Khan, N. A.; Jun, J. W.; Jeong, J. H.; Jhung, S. H., Remarkable Adsorptive Performance of a Metal-Organic Framework, Vanadium-Benzenedicarboxylate (MIL-47), for Benzothiophene. *Chem. Commun.* **2011,** *47* (4), 1306-1308.

35. Kim, H.-T.; Kim, S.-M.; Jun, K.-W.; Yoon, Y.-S.; Kim, J.-H., Desulfurization of Odorant-Containing Gas: Removal of t-Butylmercaptan on Cu/ZnO/Al2O3. *Int. J. Hydrogen Energy* **2007,** *32* (15), 3603-3608.

36. Kim, J. H.; Ma, X. L.; Zhou, A. N.; Song, C. S., Ultra-Deep Desulfurization and Denitrogenation of Diesel Fuel by Selective Adsorption over Three Different Adsorbents: A Study on Adsorptive Selectivity and Mechanism. *Catal. Today* **2006,** *111* (1-2), 74-83.

37. Lee, D.; Ko, E. Y.; Lee, H. C.; Kim, S.; Park, E. D., Adsorptive Removal of Tetrahydrothiophene (THT) and tert-Butylmercaptan (TBM) using Na-Y and AgNa-Y Zeolites for Fuel Cell Applications. *Appl. Catal., A* **2008,** *334* (1-2), 129-136.

38. Liu, B. J.; Zhu, Y. B.; Liu, S. W.; Mao, J. W., Adsorption Equilibrium of Thiophenic Sulfur Compounds on the Cu-BTC Metal-Organic Framework. *J. Chem. Eng. Data* **2012,** *57* (4), 1326-1330.

39. Peralta, D.; Chaplais, G.; Simon-Masseron, A.; Barthelet, K.; Pirngruber, G. D., Metal-Organic Framework Materials for Desulfurization by Adsorption. *Energy Fuels* **2012,** *26* (8), 4953-4960.

40. Roh, H. S.; Jun, K. W.; Kim, J. Y.; Kim, J. W.; Park, D. R.; Kim, J. D.; Yang, S. S., Adsorptive Desulfurization of Natural Gas for Fuel Cells. *J. Ind. Eng. Chem.* **2004,** *10* (4), 511-515.

41. Satokawa, S.; Kobayashi, Y.; Fujiki, H., Adsorptive Removal of Dimethylsulfide and t-Butylmercaptan from Pipeline Natural Gas Fuel on Ag Zeolites under Ambient Conditions. *Appl. Catal., B* **2005,** *56* (1-2), 51-56.

42. Shimizu, K.; Kobayashi, N.; Satsuma, A.; Kojima, T.; Satokawa, S., Mechanistic Study on Adsorptive Removal of tert-Butanethiol on Ag-Y Zeolite under Ambient Conditions. *J. Phys. Chem. B* **2006,** *110* (45), 22570-22576.

43. Van de Voorde, B.; Boulhout, M.; Vermoortele, F.; Horcajada, P.; Cunha, D.; Lee, J. S.; Chang, J.-S.; Gibson, E.; Daturi, M.; Lavalley, J.-C.; Vimont, A.; Beurroies, I.; De Vos, D. E., N/S-Heterocyclic Contaminant Removal from Fuels by the Mesoporous Metal-Organic Framework MIL-100: The Role of the Metal Ion. *J. Am. Chem. Soc.* **2013,** *135* (26), 9849-9856.

44. Weber, G.; Bellat, J. P.; Benoit, F.; Paulin, C.; Limborg-Noetinger, S.; Thomas, M., Adsorption Equilibrium of Light Mercaptans on Faujasites. *Adsorption* **2005,** *11*, 183-188.

45. Weber, G.; Benoit, F.; Bellat, J. P.; Paulin, C.; Mougin, P.; Thomas, M., Selective Adsorption of Ethyl Mercaptan on NaX Zeolite. *Microporous Mesoporous Mater.* **2008,** *109* (1-3), 184-192.

46. Yang, R. T.; Hernandez-Maldonado, A. J.; Yang, F. H., Desulfurization of Transportation Fuels with Zeolites under Ambient Conditions. *Science* **2003,** *301* (5629), 79-81.

47. Hwang, C.-L.; Tai, N.-H., Removal of dimethylsulfide by adsorption on ion-exchanged zeolites. *Appl. Catal. B-Environ.* **2010,** *93* (3-4), 363-367.

48. Satokawa, S.; Ohnuki, T.; Takahiro, T.; Urasaki, K.; Kojima, T., Adsorptive Removal of t-Butanethiol Using Metal Ion-exchange Y Type Zeolite under Ambient Conditions. *J. Jpn. Pet. Inst* **2010,** *53* (2), 83-87.

49. Husain, S.; Koros, W. J., Mixed matrix hollow fiber membranes made with modified HSSZ-13 zeolite in polyetherimide polymer matrix for gas separation. *Journal of membrane science* **2007,** *288* (1-2), 195-207.

50. Lively, R. P.; Bessho, N.; Bhandari, D. A.; Kawajiri, Y.; Koros, W. J., Thermally moderated hollow fiber sorbent modules in rapidly cycled pressure swing adsorption mode for hydrogen purification. *International Journal of Hydrogen Energy* **2012,** *37* (20), 15227-15240.

51. Khan, N. A.; Hasan, Z.; Jhung, S. H., Adsorptive removal of hazardous materials using metal-organic frameworks (MOFs): A review. *J. Hazard. Mater.* **2013,** *244*, 444-456.

52. Srivastava, V. C., An Evaluation of Desulfurization Technologies for Sulfur Removal from Liquid Fuels. *RSC Adv.* **2012,** *2* (3), 759-783.

53. Achmann, S.; Hagen, G.; Hammerle, M.; Malkowsky, I.; Kiener, C.; Moos, R., Sulfur Removal from Low-Sulfur Gasoline and Diesel Fuel by Metal-Organic Frameworks. *Chemical Engineering & Technology* **2010,** *33* (2), 275-280.

54. Van de Voorde, B.; Munn, A. S.; Guillou, N.; Millange, F.; De Vos, D. E.; Walton, R. I., Adsorption of N/S heterocycles in the flexible metal-organic framework MIL-53(Fe-III) studied by in situ energy dispersive X-ray diffraction. *Physical Chemistry Chemical Physics* **2013,** *15* (22), 8606-8615.

55. Ahmed, I.; Khan, N. A.; Jhung, S. H., Graphite Oxide/Metal-Organic Framework (MIL-101): Remarkable Performance in the Adsorptive Denitrogenation of Model Fuels. *Inorganic Chemistry* **2013,** *52* (24), 14155-14161.

56. Dai, W.; Hu, J.; Zhou, L. M.; Li, S.; Hu, X.; Huang, H., Removal of Dibenzothiophene with Composite Adsorbent MOF-5/Cu(I). *Energy & Fuels* **2013,** *27* (2), 816-821.

57. Maes, M.; Trekels, M.; Boulhout, M.; Schouteden, S.; Vermoortele, F.; Alaerts, L.; Heurtaux, D.; Seo, Y.-K.; Hwang, Y. K.; Chang, J.-S.; Beurroies, I.; Denoyel, R.; Temst, K.; Vantomme, A.; Horcajada, P.; Serre, C.; De Vos, D. E., Selective Removal of N-Heterocyclic Aromatic Contaminants from Fuels by Lewis Acidic Metal-Organic Frameworks. *Angewandte Chemie-International Edition* **2011,** *50* (18), 4210-4214.

58. Hamon, L.; Serre, C.; Devic, T.; Loiseau, T.; Millange, F.; Ferey, G.; De Weireld, G., Comparative Study of Hydrogen Sulfide Adsorption in the MIL-53(Al, Cr, Fe), MIL-

47(V), MIL-100(Cr), and MIL-101(Cr) Metal-Organic Frameworks at Room Temperature. *Journal of the American Chemical Society* **2009,** *131* (25), 8775-+.

59. Petit, C.; Mendoza, B.; Bandosz, T. J., Hydrogen Sulfide Adsorption on MOFs and MOF/Graphite Oxide Composites. *Chemphyschem* **2010,** *11* (17), 3678-3684.

60. Glover, T. G.; Peterson, G. W.; Schindler, B. J.; Britt, D.; Yaghi, O., MOF-74 building unit has a direct impact on toxic gas adsorption. *Chemical Engineering Science* **2011,** *66* (2), 163-170.

61. Britt, D.; Tranchemontagne, D.; Yaghi, O. M., Metal-organic frameworks with high capacity and selectivity for harmful gases. *Proceedings of the National Academy of Sciences of the United States of America* **2008,** *105* (33), 11623-11627.

62. Mueller, U.; Schubert, M.; Teich, F.; Puetter, H.; Schierle-Arndt, K.; Pastre, J., Metal-organic frameworks - prospective industrial applications. *Journal of Materials Chemistry* **2006,** *16* (7), 626-636.

63. Yang, R. T., *Gas Separation by Adsorption Processes*. Boston: Butterworths, 1987.

64. Feng, X. S.; Pan, C. Y.; McMinis, C. W.; Ivory, J.; Ghosh, D., Hollow-fiber-based adsorbers for gas separation by pressure-swing adsorption. *Aiche J.* **1998,** *44* (7), 1555-1562.

65. Gilleskie, G. L.; Parker, J. L.; Cussler, E. L., Gas Separations in Hollow-Fiber Adsorbers. *Aiche J.* **1995,** *41* (6), 1413-1425.

66. Bhandari, D. A.; Bessho, N.; Koros, W. J., Dual Layer Hollow Fiber Sorbents for Trace H2S Removal from Gas Streams. *Chem. Eng. Sci.* **2013,** *94*, 256-264.

67. Hu, J.; Cai, H. P.; Ren, H. Q.; Wei, Y. M.; Xu, Z. L.; Liu, H. L.; Hu, Y., Mixed-Matrix Membrane Hollow Fibers of Cu-3(BTC)(2) MOF and Polyimide for Gas Separation and Adsorption. *Ind. Eng. Chem. Res.* **2010,** *49* (24), 12605-12612.

68. Lively, R. P.; Chance, R. R.; Mysona, J. A.; Babu, V. P.; Deckman, H. W.; Leta, D. P.; Thomann, H.; Koros, W. J., CO2 Sorption and Desorption Performance of Thermally Cycled Hollow Fiber Sorbents. *Int. J. Greenhouse Gas Control* **2012,** *10*, 285-294.

69. Brown, A. J.; Brunelli, N. A.; Eum, K.; Rashidi, F.; Johnson, J. R.; Koros, W. J.; Jones, C. W.; Nair, S., Interfacial Microfluidic Processing of Metal-Organic Framework Hollow Fiber Membranes. *Science* **2014,** *345* (6192), 72-75.

70. Brown, A. J.; Johnson, J. R.; Lydon, M. E.; Koros, W. J.; Jones, C. W.; Nair, S., Continuous Polycrystalline Zeolitic Imidazolate Framework-90 Membranes on Polymeric Hollow Fibers. *Angew. Chem.-Int. Edit.* **2012,** *51* (42), 10615-10618.

71. Kusgens, P.; Zgaverdea, A.; Fritz, H. G.; Siegle, S.; Kaskel, S., Metal-Organic Frameworks in Monolithic Structures. *J. Am. Ceram. Soc.* **2010,** *93* (9), 2476-2479.

72. Li, Y. Y.; Perera, S. P.; Crittenden, B. D., Zeolite Monoliths for Air Separation Part 1: Manufacture and Characterization. *Chem. Eng. Res. Des.* **1998,** *76* (A8), 921-930.

73. Rezaei, F.; Mosca, A.; Hedlund, J.; Webley, P. A.; Grahn, M.; Mouzon, J., The Effect of Wall Porosity and Zeolite Film Thickness on the Dynamic Behavior of Adsorbents in the Form of Coated Monoliths. *Sep. Purif. Technol.* **2011,** *81* (2), 191-199.

74. Schwab, M. G.; Senkovska, I.; Rose, M.; Koch, M.; Pahnke, J.; Jonschker, G.; Kaskel, S., MOF@PolyHIPEs. *Adv. Eng. Mater.* **2008,** *10* (12), 1151-1155.

75. Gabelman, A.; Hwang, S. T., Hollow Fiber Membrane Contactors. *J. Membr. Sci.* **1999,** *159* (1-2), 61-106.

76. Lively, R. P.; Chance, R. R.; Koros, W. J., Enabling Low-Cost CO2 Capture via Heat Integration. *Ind. Eng. Chem. Res.* **2010,** *49* (16), 7550-7562.

77. Bhandari, D. A.; Bessho, N.; Koros, W. J., Hollow Fiber Sorbents for Desulfurization of Natural Gas. *Ind. Eng. Chem. Res.* **2010,** *49* (23), 12038-12050.

78. Lively, R. P.; Chance, R. R.; Kelley, B. T.; Deckman, H. W.; Drese, J. H.; Jones, C. W.; Koros, W. J., Hollow Fiber Adsorbents for CO2 Removal from Flue Gas. *Ind. Eng. Chem. Res.* **2009,** *48* (15), 7314-7324.

79. McKelvey, S. A.; Clausi, D. T.; Koros, W. J., A Guide to Establishing Hollow Fiber Macroscopic Properties for Membrane Applications. *J. Membr. Sci.* **1997,** *124* (2), 223-232.

80. Bhandari, D.; Olanrewaju, K. O.; Bessho, N.; Breedveld, V.; Koros, W. J., Dual Layer Hollow Fiber Sorbents: Concept, Fabrication and Characterization. *Sep. Purif. Technol.* **2013,** *104*, 68-80.

81. Lively, R. P., *Hollow fiber sorbents for post-combustion CO_2 capture*. Atlanta, Ga.: Georgia Institute of Technology, 2011.

82. Davis, M. E.; Davis, R. J., *Fundamentals of chemical reaction engineering*. Courier Dover Publications: 2012.

83. Chiang, H.-L.; Tsai, J.-H.; Chang, D.-H.; Jeng, F.-T., Diffusion of hydrogen sulfide and methyl mercaptan onto microporous alkaline activated carbon. *Chemosphere* **2000,** *41* (8), 1227-1232.

84. Hirschfelder, J. O., *Molecular theory of gases and liquids*. 2d printing, corr. with notes added. ed.; New York: Wiley, 1964.

85. Ruthven, D. M., *Principles of adsorption and adsorption processes*. New York: Wiley, 1984.

86. Baker, R. W., *Membrane technology and applications*. 2nd ed. ed.; Chichester ;: J. Wiley, 2004.

87. Rawlings, J. B. E., J.G. , *Chemical reactor analysis and design fundamentals*. Nob Hill Publishing: Madison, Wisconsin, 2002.

88. Hines, A. L., *Mass transfer : fundamentals and applications*. Englewood Cliffs, N.J.: Prentice-Hall, 1985.

89. Do, D. D., *Adsorption analysis : equilibria and kinetics*. London: Imperial College Press, 1998.

90. Fogler, H. S., *Elements of chemical reaction engineering*. 3rd ed. ed.; Upper Saddle River, N.J.: Prentice Hall PTR, 1999.

91. Welty, J. R., *Fundamentals of momentum, heat, and mass transfer*. 5th ed. ed.; Hoboken, N.J. ;: Wiley, 2008.

92. Levenspiel, O., *Chemical reaction engineering*. 3rd ed. ed.; New York: Wiley, 1999.

93. Asimakopoulou, A.; Karabelas, A., A study of mass transfer in hollow-fiber membrane contactors—The effect of fiber packing fraction. *Journal of membrane science* **2006,** *282* (1), 430-441.

94. Seader, J. D., *Separation process principles*. New York: Wiley, 1998.

95. Kohl, A. L., *Gas purification*. 5th ed. / ed.; Houston, Tex.: Gulf Pub., 1997.

96. Crittenden, B. T., W.J., *Adsorption Technology & Design*. Butterworth-Heinemann: Great Britain, 1998; p 288.

97. Taty-Costodes, V. C.; Fauduet, H.; Porte, C.; Ho, Y. S., Removal of lead(II) ions from synthetic and real effluents using immobilized Pinus sylvestris sawdust: Adsorption on a fixed-bed column. *J. Hazard. Mater.* **2005,** *123* (1-3), 135-144.

98. Schlichte, K.; Kratzke, T.; Kaskel, S., Improved synthesis, thermal stability and catalytic properties of the metal-organic framework compound CU3(BTC)(2). *Microporous and Mesoporous Materials* **2004,** *73* (1-2), 81-88.

99. Loiseau, T.; Serre, C.; Huguenard, C.; Fink, G.; Taulelle, F.; Henry, M.; Bataille, T.; Ferey, G., A Rationale for the Large Breathing of the Porous Aluminum Terephthalate (MIL-53) upon Hydration. *Chem. - Eur. J.* **2004,** *10* (6), 1373-1382.

100. Cavka, J. H.; Jakobsen, S.; Olsbye, U.; Guillou, N.; Lamberti, C.; Bordiga, S.; Lillerud, K. P., A New Zirconium Inorganic Building Brick Forming Metal Organic Frameworks with Exceptional Stability. *J. Am. Chem. Soc.* **2008,** *130* (42), 13850-13851.

101. Rallapalli, P.; Patil, D.; Prasanth, K. P.; Somani, R. S.; Jasra, R. V.; Bajaj, H. C., An Alternative Activation Method for the Enhancement of Methane Storage Capacity of Nanoporous Aluminium Terephthalate, MIL-53(Al). *J. Porous Mater.* **2010,** *17* (5), 523-528.

102. Schoenecker, P. M.; Belancik, G. A.; Grabicka, B. E.; Walton, K. S., Kinetics Study and Crystallization Process Design for Scale-Up of UiO-66-NH2 Synthesis. *Aiche J.* **2013,** *59* (4), 1255-1262.

103. Qin, J. J.; Li, Y.; Lee, L. S.; Lee, H., Cellulose Acetate Hollow Fiber Ultrafiltration Membranes Made from CA/PVP 360 K/NMP/Water. *J. Membr. Sci.* **2003,** *218* (1-2), 173-183.

104. Kosuri, M. R.; Koros, W. J., Defect-Free Asymmetric Hollow Fiber Membranes from Torlon (R), a Polyamide-Imide Polymer, for High-Pressure CO2 Separations. *J. Membr. Sci.* **2008,** *320* (1-2), 65-72.

105. Pesek, S. C.; Koros, W. J., Aqueous Quenched Asymmetric Polysulfone Hollow Fibers Prepared by Dry Wet Phase-Separation. *J. Membr. Sci.* **1994,** *88* (1), 1-19.

106. Burtch, N. C.; Jasuja, H.; Walton, K. S., Water Stability and Adsorption in Metal–Organic Frameworks. *Chem. Rev.* **2014,** *114* (20), 10575-10612.

107. Jasuja, H.; Walton, K. S., Experimental Study of CO2, CH4, and Water Vapor Adsorption on a Dimethyl-Functionalized UiO-66 Framework. *The Journal of Physical Chemistry C* **2013,** *117* (14), 7062-7068.

108. Schoenecker, P. M.; Carson, C. G.; Jasuja, H.; Flemming, C. J. J.; Walton, K. S., Effect of Water Adsorption on Retention of Structure and Surface Area of Metal–Organic Frameworks. *Ind. Eng. Chem. Res.* **2012,** *51* (18), 6513-6519.

109. Taheri, A.; Babakhani, E. G.; Towfighi, J., Methyl mercaptan removal from natural gas using MIL-53(Al). *Journal of Natural Gas Science and Engineering* **2017,** *38*, 272-282.

110. Powder pattern identification table. In *Collection of Simulated XRD Powder Patterns for Zeolites (fifth)*, Treacy, M. M. J.; Higgins, J. B., Eds. Elsevier Science B.V.: Amsterdam, 2007; pp 10-16.

111. Jasuja, H.; Zang, J.; Sholl, D. S.; Walton, K. S., Rational Tuning of Water Vapor and CO2 Adsorption in Highly Stable Zr-Based MOFs. *Journal of Physical Chemistry C* **2012,** *116* (44), 23526-23532.

112. Yang, Q. Y.; Vaesen, S.; Ragon, F.; Wiersum, A. D.; Wu, D.; Lago, A.; Devic, T.; Martineau, C.; Taulelle, F.; Llewellyn, P. L.; Jobic, H.; Zhong, C. L.; Serre, C.; De Weireld, G.; Maurin, G., A Water Stable Metal-Organic Framework with Optimal Features for CO2 Capture. *Angewandte Chemie-International Edition* **2013,** *52* (39), 10316-10320.

113. Myers, A. L.; Monson, P. A., Physical adsorption of gases: the case for absolute adsorption as the basis for thermodynamic analysis. *Adsorption* **2014,** *20* (4), 591-622.

114. Bruinsma, P. J.; Kim, A. Y.; Liu, J.; Baskaran, S., Mesoporous Silica Synthesized by Solvent Evaporation: Spun Fibers and Spray-Dried Hollow Spheres. *Chem. Mater.* **1997,** *9* (11), 2507-2512.

115. Chen, G.; Koros, W. J.; Jones, C. W., Hybrid Polymer/UiO-66(Zr) and Polymer/NaY Fiber Sorbents for Mercaptan Removal from Natural Gas. *ACS Appl. Mater. Interfaces* **2016,** *8* (15), 9700-9709.

116. Stephenson, R. M.; Malanowski, S., *Handbook of the thermodynamics of organic compounds.* . American Institute of Chemical Engineers: Elsevier, New York, 1989; Vol. 35, p 877-877.

117. Patton, A.; Crittenden, B. D.; Perera, S. P., Use of the linear driving force approximation to guide the design of monolithic adsorbents. *Chemical Engineering Research & Design* **2004,** *82* (A8), 999-1009.